

GRANT
IN 34-CR
154205
P-82

ALGORITHM AND CODE DEVELOPMENT FOR UNSTEADY THREE-DIMENSIONAL NAVIER-STOKES EQUATIONS

Shigeru Obayashi

(NASA-CR-192760) ALGORITHM AND
CODE DEVELOPMENT FOR UNSTEADY
THREE-DIMENSIONAL NAVIER-STOKES
EQUATIONS (MCAT Inst.) ~~82~~ p

N93-23234

Unclass

496152

73p

G3/34 0154205

March 1993

NCC2-605

MCAT Institute
3933 Blue Gum Drive
San Jose, CA 95127

CASI

ORIGINAL CONTAINS
COLOR ILLUSTRATIONS

ALGORITHM AND CODE DEVELOPMENT FOR UNSTEADY THREE-DIMENSIONAL NAVIER-STOKES EQUATIONS

Shigeru Obayashi

March 1993

NCC2-605

MCAT Institute
3933 Blue Gum Drive
San Jose, CA 95127

Algorithm and Code Development for Unsteady Three-Dimensional Navier-Stokes Equations

Shigeru Obayashi

Introduction

In the last two decades, there have been extensive developments in computational aerodynamics, which constitutes a major part of the general area of computational fluid dynamics. Such developments are essential to advance the understanding of the physics of complex flows, to complement expensive wind-tunnel tests, and to reduce the overall design cost of an aircraft, particularly in the area of aeroelasticity.

Aeroelasticity plays an important role in the design and development of aircraft, particularly modern aircraft, which tend to be more flexible. Several phenomena that can be dangerous and limit the performance of an aircraft occur because of the interaction of the flow with flexible components. For example, an aircraft with highly swept wings may experience vortex-induced aeroelastic oscillations. Also, undesirable aeroelastic phenomena due to the presence and movement of shock waves occur in the transonic range. Aeroelastically critical phenomena, such as a low transonic flutter speed, have been known to occur through limited wind-tunnel tests and flight tests.

Aeroelastic tests require extensive cost and risk. An aeroelastic wind-tunnel experiment is an order of magnitude more expensive than a parallel experiment involving only aerodynamics. By complementing the wind-tunnel experiments with numerical simulations, the overall cost of the development of aircraft can be considerably reduced. In order to accurately compute aeroelastic phenomenon it is necessary to solve the unsteady Euler/Navier-Stokes equations simultaneously with the structural equations of motion. These equations accurately describe the flow phenomena for aeroelastic applications.

At Ames a code, ENSAERO, is being developed for computing the unsteady aerodynamics and aeroelasticity of aircraft and it solves the Euler/Navier-Stokes equations. The purpose of this contract is to continue the algorithm enhancements of ENSAERO and to apply the code to complicated geometries. During the last year, the geometric capability of the code has been extended to simulate transonic flows, a wing with oscillating control surface. Single-grid and zonal approaches were tested. For the zonal approach, a new interpolation technique has been introduced. The key development of the algorithm was an interface treatment between moving zones for a control surface using the virtual-zone concept. This report summarizes briefly the work performed during the period, April 1, 1992 through March 31, 1993. Additional details on the various aspects of the study are given in the Appendices.

Research Efforts

The following specific objectives have been performed:

1. The zonal procedure coded in ENSAERO was tested. Flows over a wing with oscillating control surface were simulated. The procedure was validated through

comparisons with experimental data. The resultant code has been extended for wing-body configurations with oscillating control surface. See Appendix C and F.

2. Parallel to the use of the existing zonal technique, more robust and generalized grid interpolation technique was investigated. A new procedure for zonal interface using the virtual zone technique has been added to ENSAERO. See Appendix D.

3. Research for the turbulence model is undergoing. A problem with the Johnson-King model has been pointed out at Langley Research Center. Our independent calculation using their grid confirmed the observation.

Results

Virtual Zones

Virtual zones are zones of zero thickness (for a finite volume formulation) which serve to transfer solid wall (or other) boundary conditions to an interface condition. Thus multiple boundary conditions can be imposed on a block face with the same flexibility as an interface condition. Virtual zones also decouple the process of volume grid zoning from the surface grid patches which define the aerodynamic configuration under study. Surface grid patches are required in order to impose the proper boundary conditions. The volume grid zones should be set up to obtain the proper mesh qualities required for numerical accuracy. Another advantage of the decoupling is that much fewer zones are now needed, thus easing the effort and time required to generate the grids about complex and realistic configurations.

The original zoning capability of the ENSAERO code was extended by including the above capability of multiple interface conditions on a single block face. Since the code is a finite difference code the zones required an overlap at the boundaries of the zones to allow for the proper interblock communication (*ie.* interfacing). In this study a one cell overlap was chosen. For this kind of zoning the virtual zones of zero thickness used for the finite volume formulation is not appropriate. Instead the thickness of the virtual zones had to be expanded to include the extent of the overlap of the zones. In other words the virtual zones for the present formulation are now one cell thick. There is a slight mismatch of a half cell thickness between the location of the actual solid wall and the location where the virtual zones applies the solid wall boundary condition. This mismatch does not occur with the finite volume formulation. However in the present case the slight mismatch had no discernible influence on the overall flow field, especially in the case where flows at the ends of the flaps and wings are treated as viscous, rather than as inviscid.

The test case considered was a clipped delta wing with an oscillating trailing edge control surface. The wing planform is shown in Fig. 1. The wing has a leading edge sweep angle of 50.4 deg and a 6 % thick circular arc airfoil section. At $M_\infty = 0.9$ and $\alpha = 3$ deg, both a leading edge vortex and a shock wave are present on the upper surface of the wing. The C-H grids of the three zones consist of $151 \times 13 \times 34$, $151 \times 15 \times 34$, and $151 \times 20 \times 34$ points from the inboard to the outboard zones. Since the experiment was conducted using a Freon test medium, the ratio of specific heats, γ , was set to 1.135 in the present computations.

Figure 2 shows the unsteady pressures with the control surface oscillating at a frequency of 8 Hz and an amplitude of 6.65 deg at $M_\infty = 0.9$ and $\alpha = 3$ deg and $Re_c = 17 \times 10^6$ based on the root chord. The results are shown as the amplitude and phase angle of the upper surface at the three span stations as indicated in the figure. In general, the agreement with the experimental results is good. Because the accuracy of experiment had its own limitations, the virtual zone results are also compared with the single grid results. As

shown there is quite a discrepancy between the virtual zone results and the single grid results (the $151 \times 44 \times 34$ grid), especially in the amplitudes at the center of the control surface. The discrepancy is however most likely due to the gap that was introduced between the flap and wing in the single grid case to accommodate the shearing grid. If the gap is reduced by increasing the spanwise resolution of the wing and control surface, the computational results of the refined single grid case ($151 \times 87 \times 34$) approach those of the virtual zone. This particular example demonstrates the importance of simulating the geometry of the control surface/wing configuration accurately.

Wing-Body Configuration with Oscillating Control Surfaces

Next the code has been extended for unsteady Navier-Stokes simulations of transonic flows over a rigid arrow-wing body configuration of supersonic transport-type aircraft with oscillating control surfaces. The H-H topology grid was used. The ICEM DDN CAD software system by CDC was used to generate the surface grid. Then the volume grid was generated by using HYPGEN code. To treat the control surface movement, the single-grid approach was used. Figure 3 shows the geometry of the wind tunnel model. The configuration is a thin, low aspect ratio, highly swept wing mounted below the centerline of a slender body. The wing is flat with a rounded leading edge. The body is extended to downstream. This half-span grid consists of 110 points in the streamwise direction, 116 points in the spanwise direction, and 40 points normal to the body surface, in total of 510,400 points. In the following computations, the grid is further divided into the upper and lower grids at the wing and the H-topology cut condition is provided through a zonal interface. For the full-span configuration, the grid is mirrored to the other side and thus the number of the grid points is doubled. It should be noted that the exact wing tip definition was not available so the tip thickness was decreased to zero across three grid points.

Figure 4 shows the steady pressures compared with experiment at three spanwise sections for the half-span configuration. The flow conditions consists of $M_\infty = 0.85$, $\alpha = 8$ deg, $\delta = 0$ deg and $Re_c = 9.5 \times 10^6$ based on the mean aerodynamic chord. The leading-edge vortex is captured well by the computed results. Figure 5 shows the corresponding case with a flap deflection of $\delta = 8$ deg. The effect of the deflection is apparent at the outboard sections. Figure 6 illustrates the instantaneous antisymmetric position of oscillating control surfaces. Comparison of response characteristics between symmetric and antisymmetric control surface motions on the right and left wings is being studied.

Concluding Remarks

The geometric capability of the code, ENSAERO, has been extended to wing-body configuration with oscillating control surface. Comparisons with available experimental data show good agreement.

The future research plan is to extend the code toward a complete aircraft. The next milestone is Navier-Stokes computation with engine thrust. For the code validation, good experimental data will be required.

Research in turbulence modeling is ongoing. The models we tested often show dependency on the numerical dissipation. Further improvements will be studied for reliability.

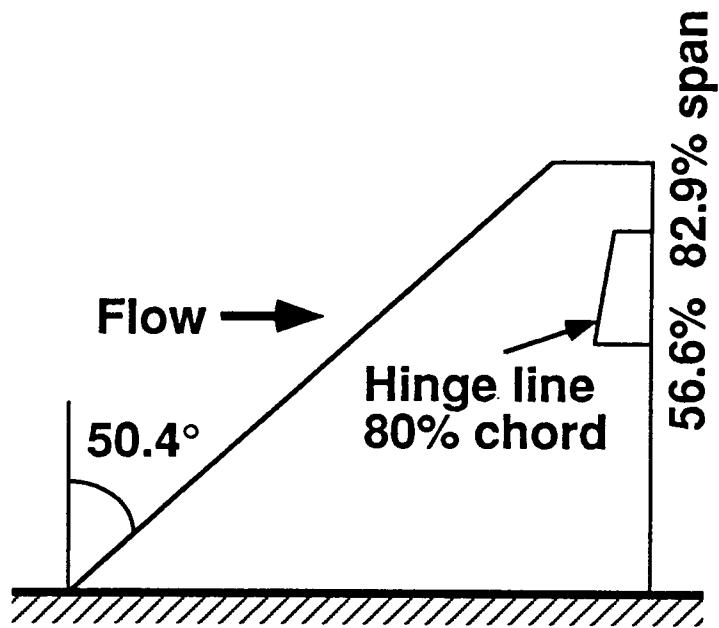


Fig. 1 Planform of clipped delta wing with trailing edge flap.

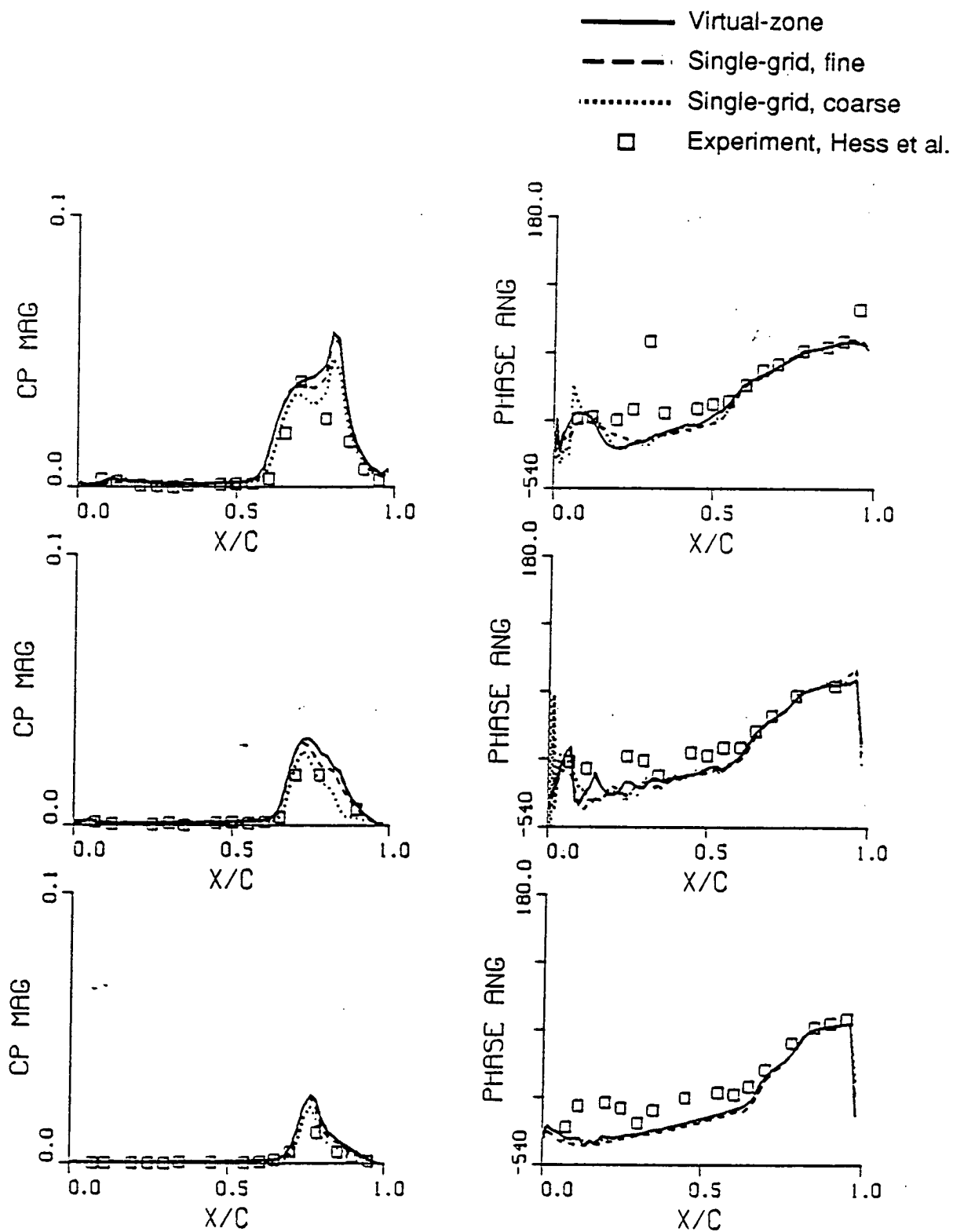
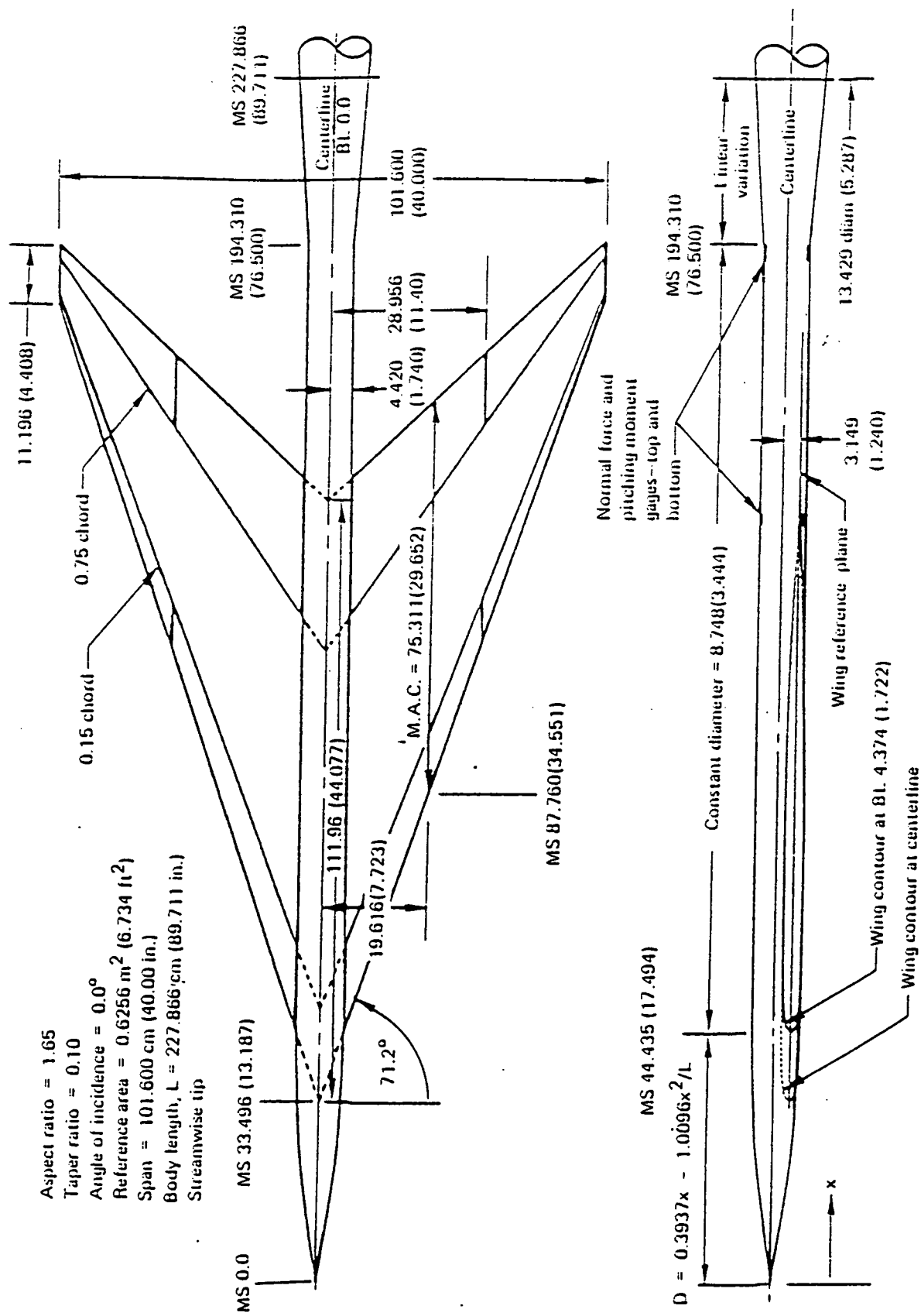


Fig. 2 Comparison of unsteady pressures between virtual-zone and single-grid computations with experiment.



All dimensions in centimeters (inches)

Fig. 3 Wind-tunnel model geometry of an arrow-wing body configuration.

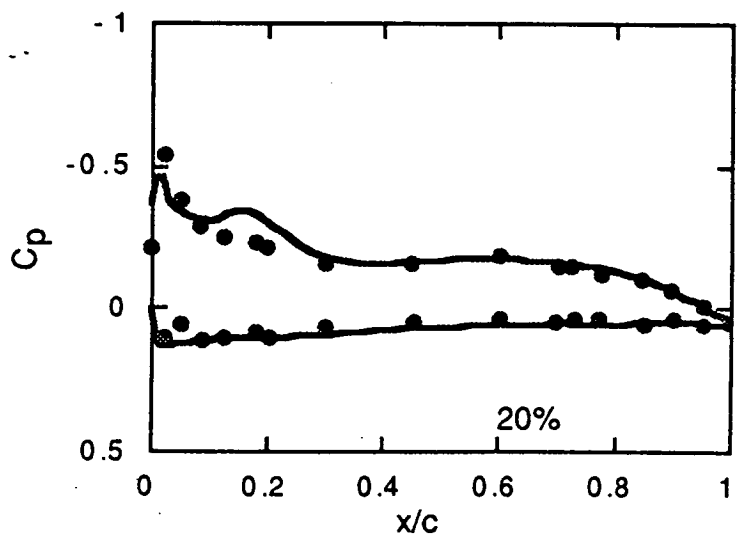
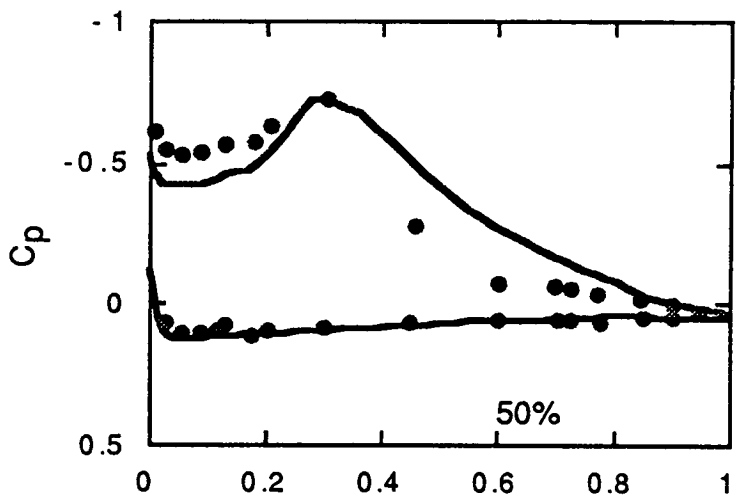
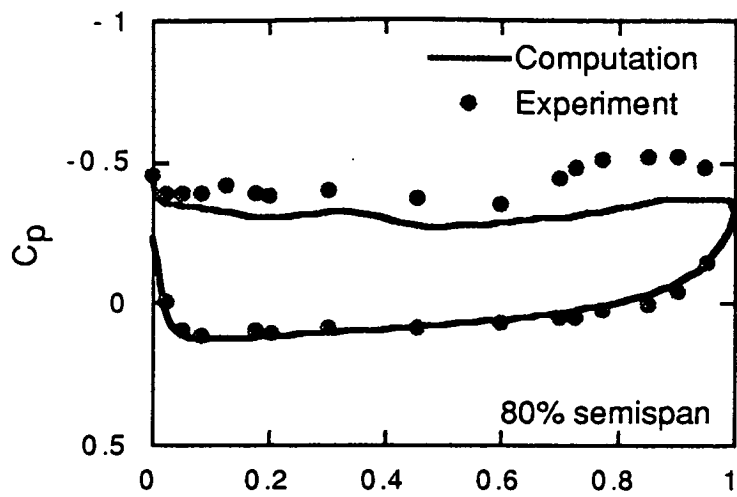


Fig. 4 Comparison of computed steady pressures with experiment.

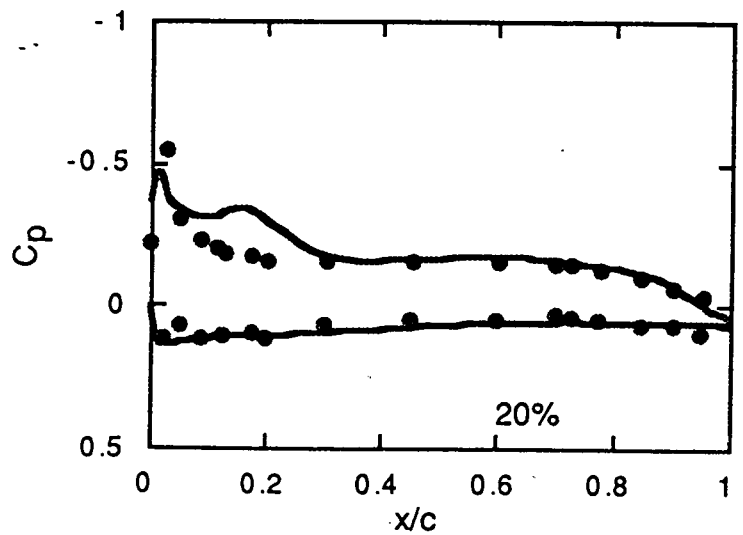
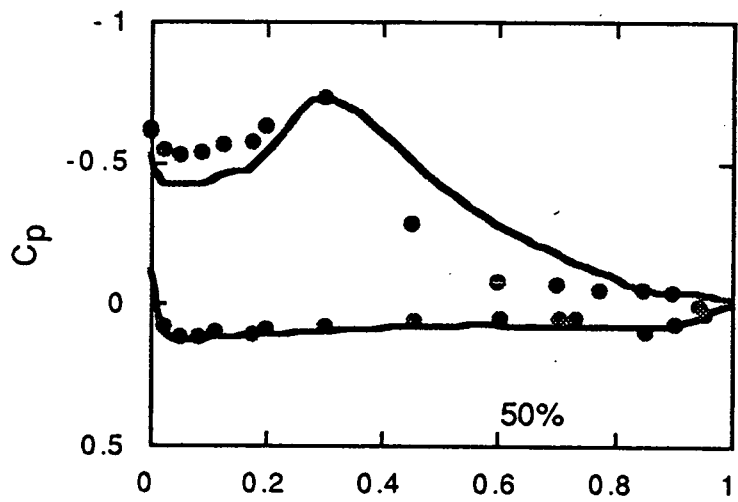
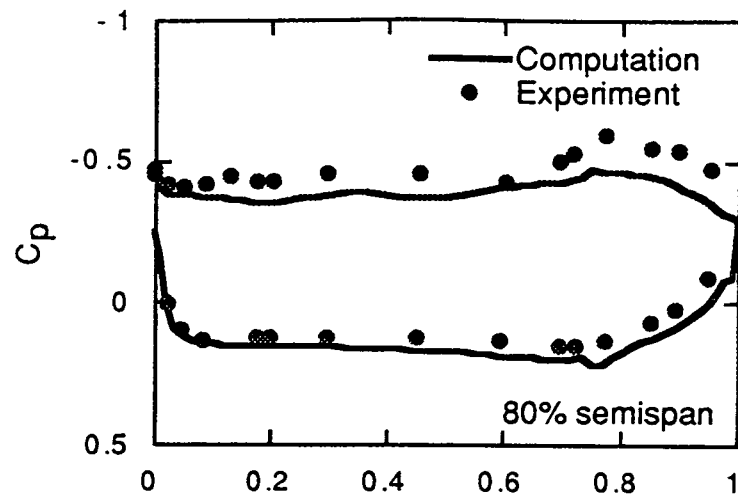


Fig. 5 Comparison of computed steady pressures with experiment.

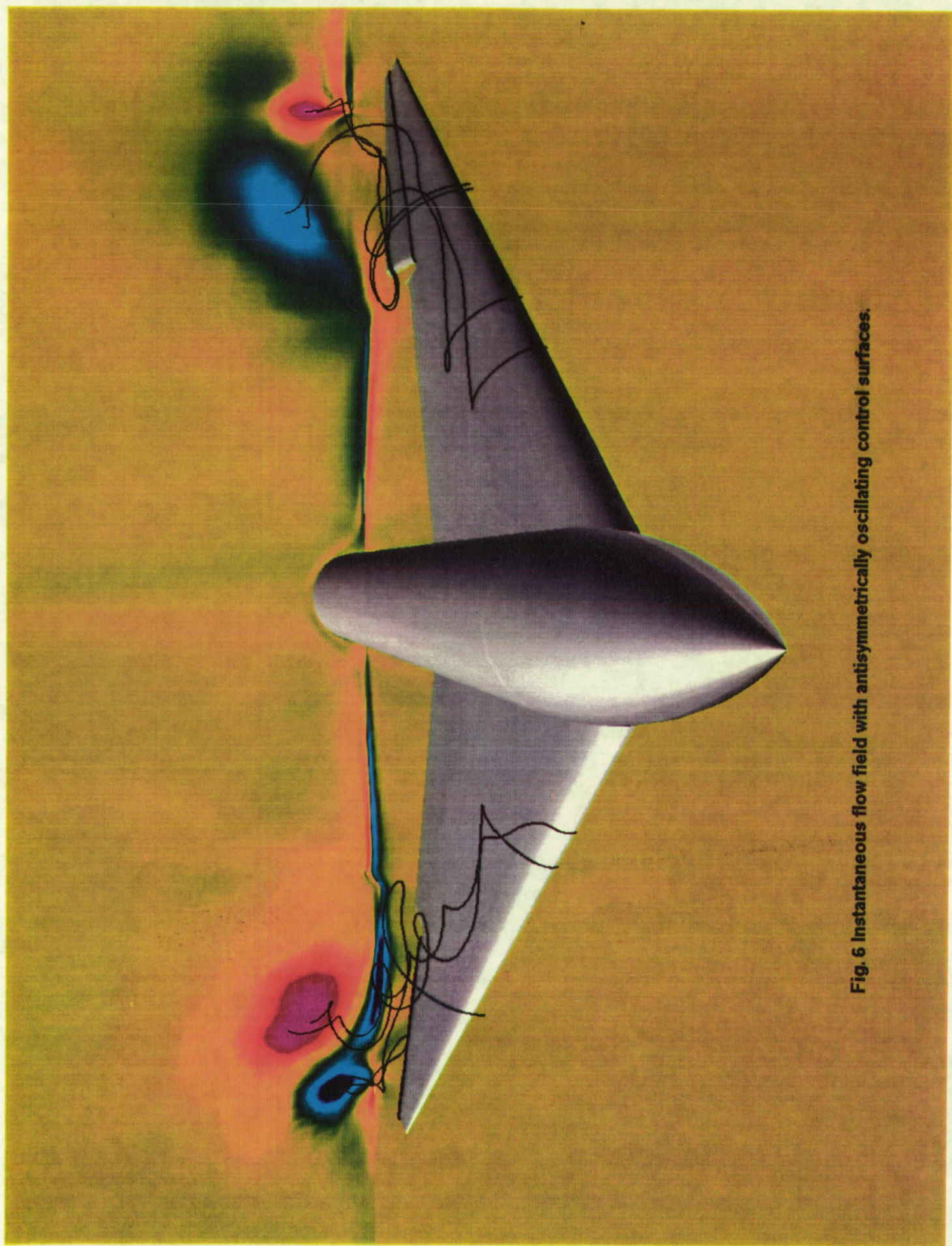


Fig. 6 Instantaneous flow field with antisymmetrically oscillating control surfaces.

APPENDIX A

Freestream Capturing for Moving Coordinates in Three Dimensions

S. Obayashi

Reprinted from

AIAA Journal

Volume 30, Number 4, April 1992, Pages 1125-1128



A publication of the
American Institute of Aeronautics and Astronautics, Inc.
The Aerospace Center, 370 L'Enfant Promenade, SW
Washington, DC 20024-2518

PRECEDING PAGE BLANK NOT FILMED

Freestream Capturing for Moving Coordinates in Three Dimensions

Shigeru Obayashi*
NASA Ames Research Center,
Moffett Field, California 94035

Introduction

BODY-CONFORMING coordinate transformations of a fluid conservation law are generally used in computational fluid dynamics. The associated metrics must satisfy certain geometric identities to maintain the global conservation for numerical solutions.¹ These metrics are called freestream capturing (or preserving) metrics. Numerical techniques are known to capture the freestream on stationary grids.²⁻⁴ However, the extension of such a formulation for moving grids is not straightforward. The error introduced in forming the time metrics has been overlooked because it is negligible in most cases, but it can be significant in certain applications such as helicopter rotor flows.⁵ Rigorous formulations based on the types of grid motions were discussed in Ref. 1, and demonstrated, for example, in Ref. 6. The present study describes detailed formulas that can be used in both finite volume (FV) and finite difference (FD) methods for constructing freestream capturing metrics in space and time.

Finite Volume Formulation

Geometric Identities and Freestream Capturing

The integral form of a conservation law for a given cell can be written as

$$\int_{V(t_2)} Q dV - \int_{V(t_1)} Q dV + \int_{t_1}^{t_2} \oint_{S(t)} n \cdot F dS dt = 0 \quad (1)$$

where $V(t)$ is the cell volume and $n dS(t)$ is a vector element of surface area with outwardly normal n . Considering the Euler equations, Q is a vector of conserved variables, viz., density, momentum, and energy, and F is the flux tensor of Q . The flux F can be decomposed into the flux in the stationary frame F_{st} and the contribution due to surface element velocity v as

$$F = F_{st} - vQ \quad (2)$$

Received Nov. 27, 1990; revision received June 10, 1991; accepted for publication June 24, 1991. Copyright © 1991 by the American Institute of Aeronautics and Astronautics, Inc. No copyright is asserted in the United States under Title 17, U.S. Code. The U.S. Government has a royalty-free license to exercise all rights under the copyright claimed herein for Governmental purposes. All other rights are reserved by the copyright owner.

*Senior Research Scientist, MCAT Institute, San Jose, CA 95127.

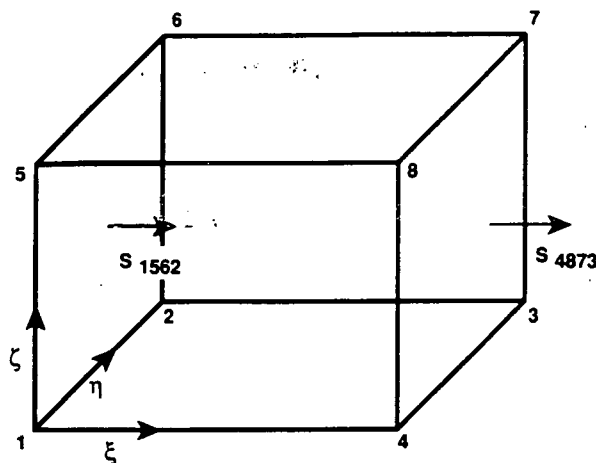


Fig. 1 Geometry of a hexahedral cell.

For the freestream condition Q_∞ and $F_{st\infty}$ the geometric identities can be derived from Eq. (1) as follows:

$$Q_\infty[V(t_2) - V(t_1)] = -F_{st\infty} \cdot \int_{t_1}^{t_2} \oint_S \mathbf{n} \, dS \, dt + Q_\infty \int_{t_1}^{t_2} \oint_S \mathbf{n} \cdot \mathbf{v} \, dS \, dt \quad (3)$$

On a stationary grid, the first geometric identity can be obtained as

$$\oint_S \mathbf{n} \, dS = 0 \quad (4)$$

This gives a mathematical expression for a closed cell, which is a requirement for any grid system. The corresponding time integration in Eq. (3) will be satisfied for moving grids by applying Eq. (4) at each time level. From the rest of Eq. (3), the second geometric identity can be obtained as

$$V(t_2) - V(t_1) = \int_{t_1}^{t_2} \oint_{S(t)} \mathbf{n} \cdot \mathbf{v} \, dS \, dt \quad (5)$$

This equation is essential for moving grids because it represents the conservation of volume for a moving cell. To guarantee the global conservation for numerical solutions, these geometric identities must be satisfied numerically.

Figure 1 shows a regular hexahedral cell. We assume that all edges are straight lines. Let \mathbf{r} be the position vector of a point in space. The formulas for the surface vector \mathbf{S} (note that \mathbf{S} is taken in the positive coordinate direction here) and the volume V can be defined as

$$\mathbf{S}_{1562} = \frac{1}{2}(\mathbf{r}_6 - \mathbf{r}_1) \times (\mathbf{r}_5 - \mathbf{r}_2) \quad (6)$$

$$\mathbf{S}_{1562} = (\mathbf{r}_{56} - \mathbf{r}_{12}) \times (\mathbf{r}_{15} - \mathbf{r}_{26}) \quad (7)$$

$$V_{12345678} = \frac{1}{6}(\mathbf{S}_{1485} + \mathbf{S}_{1234} + \mathbf{S}_{1562}) \cdot (\mathbf{r}_7 - \mathbf{r}_1) \quad (8)$$

where $\mathbf{r}_{56} = \frac{1}{2}(\mathbf{r}_5 + \mathbf{r}_6)$, and so on (see Ref. 1, for example). Note that Eqs. (6) and (7) result in the same expression. In fact, the surface vector is defined uniquely as long as the edges are straight lines. Also note that there are other consistent ways to compute the cell volume. However, Eq. (8) is the simplest form.

Let $\mathbf{S}_{1562} = S_{1562}\mathbf{n}$. With either Eq. (6) or (7), Eq. (4) is satisfied numerically as

$$\sum_{\text{cell}} S_{\mathbf{n}} = 0 \quad (9)$$

To satisfy Eq. (5) numerically, it is essential to compute the right-hand side correctly. It can be rewritten as

$$\int_{t_1}^{t_2} \oint_S \mathbf{n} \cdot \mathbf{v} \, dS \, dt = \int_{t_1}^{t_2} \left(\sum_{\text{cell}} S_{\mathbf{n}} \cdot \mathbf{v} \right) dt = \sum_{\text{cell}} \left(\int_{t_1}^{t_2} S_{\mathbf{n}} \cdot \mathbf{v} \, dt \right) \quad (10)$$

Let V_S be a volume swept by a surface S between the time interval $[t_1, t_2]$:

$$V_S = \int_{t_1}^{t_2} S_{\mathbf{n}} \cdot \mathbf{v} \, dt \quad (11)$$

Let $S(t_1) = S_{1562}$ and $S(t_2) = S_{1'5'6'2'}$. The volume V_S can be computed similar to Eq. (8) as

$$V_{S_{1265}} = V_{122'1'566'5'} = \frac{1}{6}(\mathbf{S}_{11'5'5} + \mathbf{S}_{122'1'} + \mathbf{S}_{1562}) \cdot (\mathbf{r}_{6'} - \mathbf{r}_1) \quad (12)$$

where $\mathbf{S}_{11'5'5}$ and $\mathbf{S}_{122'1'}$ are the surface vectors in space and time domain. Then, Eq. (5) is satisfied numerically as

$$V(t_2) - V(t_1) = \sum_{\text{cell}} V_S \quad (13)$$

This formula requires the position of the grid at t_2 , not the grid velocity \mathbf{v} itself as per Eq. (11). The position of the grid at the next time level must be given explicitly before computing the fluid motion. For aeroelastic simulations, for example, the structural equation of motion has to be coupled with the fluid equations only at explicit time levels. A fully coupled implicit formulation requires an iterative approach between the fluid and structural equations.

Geometric Identities for Time-Differential Form

The time-differential form of Eq. (1) is often used as a basis of the conservation law. Starting with the time-differential form, one can obtain similar geometric identities as in the previous section. However, this approach introduces an additional geometric identity.

The first geometric identity derived from the time-differential form is identical to Eq. (4). Then, the rest of the equation can be written as

$$\frac{\partial V}{\partial t} = \oint_S \mathbf{n} \cdot \mathbf{v} \, dS \quad (14)$$

To proceed with the surface integration on the right-hand side, let us break down the surface element velocity \mathbf{v} into its components. Let \mathbf{r} and $\mathbf{r}_0(t)$ be the position vectors of a point in space and the origin of the noninertial frame, respectively. Also let $\mathbf{v}_0(t)$ and $\Omega(t)$ be the velocity and angular velocity of the noninertial frame relative to the inertial frame, respectively. These velocities represent the rigid motion of the grid. In general,

$$\mathbf{v} = \mathbf{v}_0(t) + \Omega(t) \times [\mathbf{r} - \mathbf{r}_0(t)] + \mathbf{v}_c \quad (15)$$

where $\mathbf{v}_c(t)$ is the surface element velocity relative to the noninertial frame, which leads to change of a cell in time. From Eqs. (14) and (15), one obtains

$$\begin{aligned} \frac{\partial V}{\partial t} = & (\mathbf{v}_0 - \Omega \times \mathbf{r}_0) \cdot \left(\oint_S \mathbf{n} \, dS \right) + \Omega \cdot \left(\oint_S \mathbf{r} \times \mathbf{n} \, dS \right) \\ & + \left(\oint_S \mathbf{n} \cdot \mathbf{v}_c \, dS \right) \end{aligned} \quad (16)$$

The first integral on the right-hand side is zero due to the first geometric identity, Eq. (4). The second integral represents the rigid rotation of grid and does not contribute to the change of the cell volume. The remaining terms give the second geometric identity similar to Eq. (5).

The third geometric identity can be obtained from the second integral in Eq. (16) as

$$\oint_S \mathbf{r} \times \mathbf{n} dS = 0 \quad (17)$$

The discretized form of the third geometric identity can be expressed as

$$\sum_{\text{cell}} S \mathbf{r} \times \mathbf{n} = 0 \quad (18)$$

This is the additional requirement, which is concealed unless the grid movement is broken down properly. It must be satisfied whenever the grid rotates. Reference 1 introduces the area moment

$$\mathbf{M} = \int_S \mathbf{r} \times \mathbf{n} dS$$

to satisfy the discretized geometric identity, Eq. (18), on the hexahedron:

$$\mathbf{M}_{1562} = \mathbf{r}_{165} \times S_{165} + \mathbf{r}_{126} \times S_{126} \quad (19)$$

where $\mathbf{r}_{165} = 1/3(\mathbf{r}_1 + \mathbf{r}_6 + \mathbf{r}_5)$, $S_{165} = 1/2(\mathbf{r}_6 - \mathbf{r}_1) \times (\mathbf{r}_5 - \mathbf{r}_1)$, and so on. Note that $\mathbf{M}_{1562} \neq \mathbf{r}_{1562} \times S_{1562}$. The expression $\mathbf{r}_{1562} \times S_{1562}$ is not well defined for computing area moment because it results in a nonzero sum over a cell. In contrast, Eq. (19) is well defined so that the sum over a cell is zero. The nonzero error introduced by the use of the inconsistent area moment has a unique feature. A simple analysis⁷ shows that the error disappears on a hexahedron with parallelogram surfaces, for example, on the Cartesian grid. For a hexahedron with arbitrary quadrilateral surfaces, the error remains constant relative to the cell volume. This error may be ignored only if the effect of the Coriolis force is negligible. For example, the error is small for a flow over a wing oscillating at small amplitude. Note that the use of the surface area vector for evaluating the surface moment vector becomes consistent on a triangular surface. The use of the tetrahedral cell allows the most compact and consistent metric formulation, although it results in unstructured-grid formulations.

Finite Difference Formulation

The differential form of Eq. (1) has been used widely in FD formulations. With a generalized coordinate transformation, $\mathbf{r} = \mathbf{r}(\xi, \eta, \zeta, \tau)$ and $t = \tau$, the FD metric terms can be expressed as

$$\frac{\nabla \xi}{J} = \frac{1}{J}(\xi_x, \xi_y, \xi_z)^T = \mathbf{r}_\eta \times \mathbf{r}_\zeta = S^\xi \quad (20)$$

and

$$\frac{\xi_t}{J} = -S^\xi \cdot \mathbf{r}_\tau \quad (21)$$

where $\mathbf{r}_\tau = \mathbf{v}$ and the transformation Jacobian $J = 1/V$. Analogous definitions can be derived for the other directions. The cell volume as defined by Eq. (8) is different from the inverse of the transformation Jacobian in a discretized form. Nevertheless, the cell volume can be applied to the FD method with a scaling factor of one-eighth. The differential forms of the geometric identities are

$$(S^\xi)_\xi + (S^\eta)_\eta + (S^\zeta)_\zeta = 0 \quad (22)$$

$$V_\tau = (S^\xi \cdot \mathbf{r}_\tau)_\xi + (S^\eta \cdot \mathbf{r}_\tau)_\eta + (S^\zeta \cdot \mathbf{r}_\tau)_\zeta \quad (23)$$

Equation (23) is the differential statement of the geometric conservation law (GCL).⁸

The discretized form of Eq. (22) can be satisfied by the consistently differenced metrics,³ which are based on an aver-

aging procedure to numerically satisfy the differential chain rule. However, it is not straightforward to satisfy the discretized form of the GCL. The discretized form of the GCL can be written as

$$\Delta V = \Delta \tau [\delta_\xi(S^\xi \cdot \mathbf{r}_\tau) + \delta_\eta(S^\eta \cdot \mathbf{r}_\tau) + \delta_\zeta(S^\zeta \cdot \mathbf{r}_\tau)] \quad (24)$$

where δ indicates the central-difference operator in each coordinate direction. Analogous to the derivation of Eq. (18), if the grid is moved in a rigid rotation, $V_\tau = 0$ and $\mathbf{r}_\tau = \Omega \times \mathbf{r}$. Then the left-hand side of Eq. (24) equals zero. However, the right-hand side becomes $\delta_\xi(\mathbf{r} \times S^\xi) + \delta_\eta(\mathbf{r} \times S^\eta) + \delta_\zeta(\mathbf{r} \times S^\zeta) \neq 0$. Thus, the freestream will not be captured by solving Eq. (24) with the FD method. The GCL implies only a necessary condition to capture the freestream, not a sufficient condition.

The analysis of the FD formulation can be simplified with the aid of the previous discussions for the FV formulations. Following Ref. 1, let the edges of the hexahedron in Fig. 1 be redefined as a double-sized cell in the FD grid with $\mathbf{r}_1 = \mathbf{r}_{i-1,j-1,k-1}$, $\mathbf{r}_2 = \mathbf{r}_{i-1,j+1,k-1}$, ..., $\mathbf{r}_3 = \mathbf{r}_{i+1,j+1,k-1}$, $\mathbf{r}_8 = \mathbf{r}_{i+1,j-1,k+1}$. Also, let the time level advance from t_1 to t_2 . A simple calculation⁷ shows that Eq. (7) is equivalent to the consistently differenced metrics.³ Thus, the surface vector evaluations, Eqs. (6) and (7), on the double-sized cell can be regarded as the evaluations of the freestream capturing space metrics for the FD method. The FD time-metric evaluation is also obtained from the FV method. Time integration of Eq. (24) from t_1 to t_2 easily results in Eq. (13). Thus, for example in the ξ direction, replacing $S^\xi \cdot \mathbf{r}_\tau$ in the right-hand side of Eq. (21) with the time average, $V_{S\xi}/\Delta t$ of Eq. (11), the freestream capturing time metrics can be obtained as

$$\frac{\xi_t}{J} = -\frac{1}{\Delta t} \int_{t_1}^{t_2} S^\xi \cdot \mathbf{r}_\tau dt = -\frac{V_{S\xi}}{\Delta t} \quad (25)$$

Note that ξ_t defined here is costly but contains all of the information about the movement of a cell surface, such as translation, rotation, and deformation. In contrast, Eq. (21) is a simple product of surface area and velocity of cell centroid and can represent only a translational motion.

The freestream subtraction technique will be useful for the rigid motion of the grid instead of the rigorous, costly evaluation of Eq. (25). Note that the subtraction is required only for the time-metric terms with the use of the freestream capturing metrics in space.⁵

Concluding Remarks

This Note discusses the freestream capturing and the geometric identities for a fluid conservation law. To guarantee global conservation in numerical solutions, certain geometric identities must be satisfied. Based on the full integral form of the conservation law, Eqs. (7), (8), and (13) will guarantee the freestream capturing. Based on the time-differential form, another condition [Eq. (18)] must also be satisfied. However, when the differential form is used, the global conservation is not trivial. Considering an FV cell on the FD grid, the freestream capturing metrics in space and time can be constructed from the FV formulations. Such an approach for evaluating the time metrics is costly but guarantees the global conservation for an arbitrary motion of the grid.

Acknowledgments

This work was supported by NASA Grant NCC 2-605. The author would like to thank M. Vinokur of Sterling Software for his valuable discussions.

References

1. Vinokur, M., "An Analysis of Finite-Difference and Finite-Volume Formulations of Conservation Laws," *Journal of Computational Physics*, Vol. 81, No. 1, 1989, pp. 1-52.
2. Pulliam, T. H., and Steger, J. L., "On Implicit Finite-Difference Simulations of Three-Dimensional Flow," AIAA Paper 78-10, Jan. 1978.

³Chaderjian, N. M., "Transonic Navier-Stokes Wing Solutions Using a Zonal Approach," NASA TM-88248, April 1986.

⁴Buning, P. G., Chiu, I. T., Obayashi, S., Rizk, Y. M., and Steger, J. L., "Numerical Simulation of the Integrated Space Shuttle Vehicle in Ascent," AIAA Paper 88-4359, Aug. 1988.

⁵Srinivasan, G. R., Baeder, J. D., Obayashi, S., and McCroskey, W. J., "Flowfield of a Lifting Hovering Rotor—A Navier-Stokes Simulation," 16th European Rotorcraft Forum, Paper 1.3.5, Glasgow, Scotland, UK, Sept. 1990; also NASA TM-102862, Aug. 1990.

⁶Chen, C. L., and McCroskey, W. J., "Numerical Simulation of Helicopter Multi-Bladed Rotor Flow," AIAA Paper 88-0046, Jan. 1988.

⁷Obayashi, S., "Free-Stream Capturing in Fluid Conservation Law for Moving Coordinates in Three Dimensions," NASA CR-177572, Jan. 1991.

⁸Thomas, P. D., and Lombard, C. K., "Geometric Conservation Law and Its Application to Flow Computations on Moving Grids," *AIAA Journal*, Vol. 17, No. 10, 1979, pp. 1030-1037.

APPENDIX B

Unsteady Shock-Vortex Interaction on a Flexible Delta Wing

S. Obayashi and G. P. Guruswamy

Reprinted from

Journal of Aircraft

Volume 29, Number 5, September-October 1992, Pages 790-798



A publication of the
American Institute of Aeronautics and Astronautics, Inc.
The Aerospace Center, 370 L'Enfant Promenade, SW
Washington, DC 20024-2518

Unsteady Shock-Vortex Interaction on a Flexible Delta Wing

Shigeru Obayashi* and Guru P. Guruswamy†
NASA Ames Research Center, Moffett Field, California 94035

Unsteady Navier-Stokes computations have been carried out for simulating transonic flows over a clipped delta wing undergoing oscillatory and ramp motions, including flexibility. The implicit upwind algorithm has been validated by comparing the solutions with experimental data for the oscillatory pitching motion cases. The numerical and experimental results agree well at moderate angles of attack, where a leading-edge vortex develops. The ramp motion cases have demonstrated the effects of unsteadiness of the flowfield and structural flexibility on the wing responses. For the 10-deg ramp motion, a vortex breakdown is observed. The inviscid interaction with the shock wave plays an essential role in the process of the breakdown observed in the present calculation.

Introduction

IN the last decade, there have been extensive developments in computational fluid dynamics toward the prediction of the three-dimensional flowfield about complex geometries at moderate and high angles of attack. Among the characteristics of flows over aircraft, the behavior of the flow over delta wings is of strong interest for high-speed aircraft because of the nonlinear lift increase due to the leading-edge vortex. Effects of flexibility can further influence the nature of flows on such wings. Steady-state flow problems associated with delta wings have been widely investigated computationally (for example, Refs. 1-3). Several advanced studies have also been performed for unsteady vortical flow calculations at subsonic and supersonic Mach numbers. For example, Ref. 4 presented a conical flow computation on a rigid wing and Ref. 5 presented a subsonic three-dimensional computation on a flexible wing, both involving vortical flows.

Numerical methods can play an important role in complementing expensive wind-tunnel tests, particularly in the area of aeroelasticity. An aeroelastic wind-tunnel experiment is an order of magnitude more expensive than a similar rigid-body experiment involving only aerodynamics. By complementing the experiments with numerical simulations, the overall cost of the development of aircraft can be considerably reduced. Thus development of a numerical method is desired for simulating aeroelastic phenomenon. To accurately compute aeroelastic phenomena it is necessary to solve the unsteady Euler/Navier-Stokes equations simultaneously with the structural equations of motion.

Recently a code, ENSAERO, was developed to compute aeroelastic responses by simultaneously integrating the Euler/Navier-Stokes equations and the modal structural equations of motion using aeroelastically adaptive dynamic grids.^{6,7} An upwind algorithm was implemented into the code and the resulting code was successfully applied to compute transonic flows over a typical fighter-type wing undergoing oscillatory motion.⁸

The purpose of this article is to examine the capability of the present numerical method by simulating unsteady transonic flows on a clipped delta wing, which contain a leading-edge separation. So far, unsteady transonic flow computations have dealt with the motion of shock waves on wings only at small angles of attack. The present study focuses on the formation and motion of the leading-edge vortex on a clipped delta wing at transonic speeds as well as motion of the shock wave. The code validation has been done for steady and unsteady pitching cases by comparing surface pressures with the experimental data.⁹ Computations for ramp motion cases have demonstrated effects of the unsteadiness of the flowfield and the structural flexibility on the aeroelastic responses.

Governing Aerodynamic Equations and Approximations

The nondimensionalized, thin-layer Navier-Stokes equations used in this study can be written in conservation-law form in a generalized body-conforming curvilinear coordinate system for three dimensions as follows:

$$\partial_\tau \hat{Q} + \partial_\xi \hat{E} + \partial_\eta \hat{F} + \partial_\zeta \hat{G} = \frac{1}{Re} \partial_\zeta \hat{G}^v \quad (1)$$

where $\tau = t$, $\xi = \xi(x, y, z, t)$, $\eta = \eta(x, y, z, t)$, and $\zeta = \zeta(x, y, z, t)$. In the present article, the ξ and η directions are along the streamwise and spanwise directions of a wing, respectively. The viscous derivatives associated with these directions are dropped. In contrast, the ζ direction is normal to the wing surface, and thus the viscous derivatives are retained.

The vector of conserved quantities \hat{Q} and the inviscid flux vector \hat{F} are

$$\hat{Q} = \frac{1}{J} \begin{bmatrix} \rho \\ \rho u \\ \rho v \\ \rho w \\ e \end{bmatrix}, \quad \hat{F} = \frac{1}{J} \begin{bmatrix} \rho \hat{V} \\ \rho u \hat{V} + \eta_x p \\ \rho v \hat{V} + \eta_y p \\ \rho w \hat{V} + \eta_z p \\ \rho H \hat{V} - \eta_t p \end{bmatrix} \quad (2a)$$

where H is the total enthalpy and \hat{V} is the contravariant velocity component. The time metric is related to the grid velocity as

$$\eta_t = -\eta_x x_t - \eta_y y_t - \eta_z z_t \quad (2b)$$

The Cartesian velocity components u , v , and w are nondimensionalized by the freestream speed of sound a_∞ ; the density ρ is nondimensionalized by the freestream density ρ_∞ ; the total energy per unit volume e is nondimensionalized by $\rho_\infty a_\infty^2$. For the ξ and ζ directions, \hat{E} and \hat{G} can be defined similarly.

Received March 21, 1991; presented as Paper 90-1109 at the AIAA/ASME/ASCE/AHS/ASC 32nd Structures, Structural Dynamics, and Materials Conference, Baltimore, MD, April 8-10, 1991; revision received Oct. 4, 1991; accepted for publication Oct. 8, 1991. Copyright © 1990 by the American Institute of Aeronautics and Astronautics, Inc. No copyright is asserted in the United States under Title 17, U.S. Code. The U.S. Government has a royalty-free license to exercise all rights under the copyright claimed herein for Governmental purposes. All other rights are reserved by the copyright owner.

*Senior Research Scientist, MCAT Institute, San Jose, CA 95127. Member AIAA.

†Research Scientist. Associate Fellow AIAA.

The viscous flux vector \hat{G}^v is given by

$$\hat{G}^v = \frac{1}{J} \begin{bmatrix} 0 \\ \mu m_1 u_\xi + \frac{\mu}{3} m_2 \zeta_x \\ \mu m_1 v_\xi + \frac{\mu}{3} m_2 \zeta_y \\ \mu m_1 w_\xi + \frac{\mu}{3} m_2 \zeta_z \\ \mu m_1 m_3 + \frac{\mu}{3} m_2 (\zeta_x u + \zeta_y v + \zeta_z w) \end{bmatrix} \quad (2c)$$

with

$$\begin{aligned} m_1 &= \zeta_x^2 + \zeta_y^2 + \zeta_z^2 \\ m_2 &= \zeta_x u_\xi + \zeta_y v_\xi + \zeta_z w_\xi \\ m_3 &= \frac{1}{2} (u^2 + v^2 + w^2)_\xi + \frac{1}{Pr(\gamma - 1)} (a^2)_\xi \end{aligned} \quad (2d)$$

where Re is the Reynolds number, Pr is the Prandtl number, a is the speed of sound, and J is the transformation Jacobian. Pressure is related to the conservative flow variables \hat{Q} through the equation of state for a perfect gas

$$p = (\gamma - 1) \left\{ e - \frac{\rho}{2} (u^2 + v^2 + w^2) \right\} \quad (3)$$

where ρ is the fluid density and e is total energy per unit of volume of the fluid. See Ref. 7 for detailed definitions.

The viscosity coefficient μ in \hat{G}^v is computed as the sum of $\mu_l + \mu_t$, where the laminar viscosity μ_l is taken from the freestream laminar viscosity, assumed to be constant for transonic flows, and the turbulent viscosity μ_t is evaluated by the Baldwin-Lomax algebraic eddy-viscosity model.¹⁰ Since the flowfield to be considered in this article contains a leading-edge separation, it is important to apply the modification of

Circular-arc airfoil
 $t/c = 0.06$
 L.E. sweep angle = 50.4°
 Area = 1635.88 in^2
 Span = 45.08 in.
 Root chord = 63.55 in.
 Tip chord = 9.03 in.
 Taper ratio = 0.1421

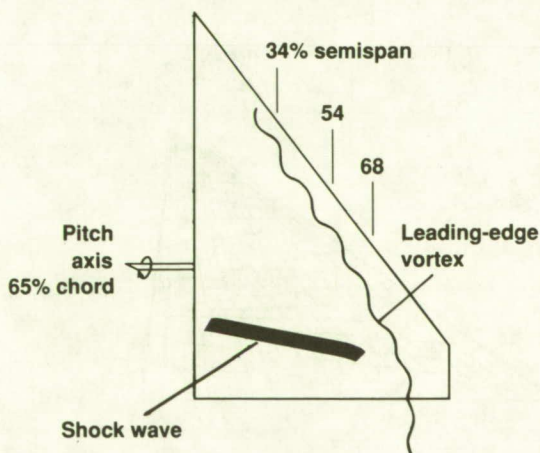


Fig. 1 Planform geometry of clipped delta wing and typical flow structure.

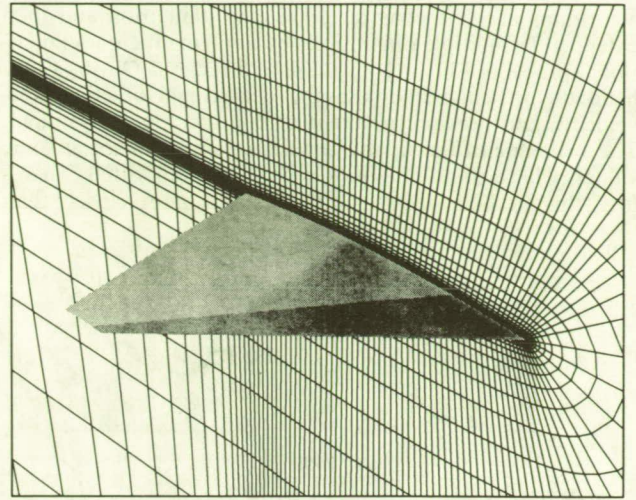


Fig. 2 Clipped delta wing and grid distributions at the root section.

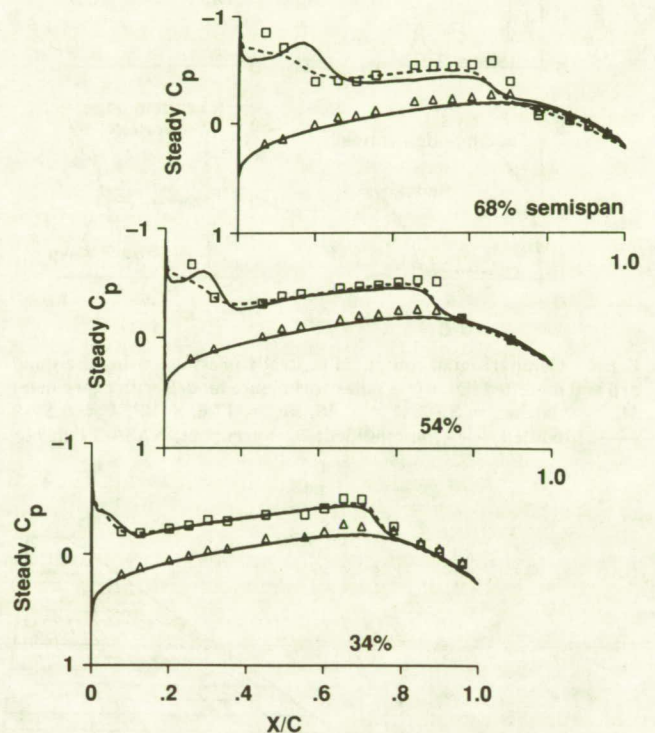


Fig. 3 Comparison of computed steady pressures using the standard and modified Baldwin-Lomax turbulence models with experiment, $M_\infty = 0.90$, $\alpha = 3.97$, $Re_c = 17.6 \times 10^6$. —, Modified; ---, unmodified; \square , \triangle , experiment, NASA TP-2594.

the turbulence model originally developed for crossflow separation by Degani and Schiff.¹¹ The modification improves the pressure prediction as shown later, even though the separation is fixed at the sharp leading edge in the following applications.

Although the nature of interaction between vortex and shock wave is predominantly inviscid, the viscous terms are important to compute right vorticity. For example, a test calculation using the Euler equations showed that the leading-edge vortex is weaker because the inviscid model does not resolve the shear layer properly.

Numerical Solution Procedure

Among upwind algorithms, a streamwise upwind algorithm has recently been developed and applied to steady-state problems of transonic flows over wings¹² and vortical flows over a delta wing¹³ on fixed grids. Most multidimensional upwind

algorithms are first constructed in one dimension and then extended to multiple dimensions by applying the one-dimensional procedure in each coordinate direction. On the other hand, the present method uses the local stream direction, flow velocity, and pressure gradient to construct the upwinding. The switching of flux evaluations always takes place at sonic values, where transonic shock waves may be located. Therefore, this method follows the flow physics more closely than

the coordinate upwind methods. The computed results confirmed the higher resolution of the present algorithm over the central-difference method as well as over other upwind methods.¹³ In this work, the streamwise upwind algorithm is applied to compute the inviscid cell-interface fluxes. A second-order central-difference evaluation is applied to the viscous term. The complete algorithm can be found in Refs. 8 and 13.

An implicit method is used for the time integration because the computational efficiency of the method is critical for expensive unsteady viscous calculations. The method chosen here is the LU-ADI (lower-upper factored, alternating direction implicit) method¹⁴ because it requires only scalar bi-diagonal matrix inversions. See Refs. 15 and 16 for additional details.

Aeroelastic Equations of Motion

The governing aeroelastic equations of motion of a flexible wing are solved using the Rayleigh-Ritz method. In this method, the resulting aeroelastic displacements at any time are expressed as a function of a finite set of assumed modes. The contribution of each assumed mode to the total motion is derived by Lagrange's equation. Furthermore, it is assumed that the deformation of the continuous wing structure can be represented by deflections at a set of discrete points. This assumption facilitates the use of discrete structural data, such as the modal vector, the modal stiffness matrix, and the modal mass matrix. These can be generated from a finite element analysis or from experimental influence-coefficient measurements. In this study, the finite element method is used to obtain the modal data.

It is assumed that the deformed shape of the wing can be represented by a set of discrete displacements at selected nodes. From the modal analysis, the displacement vector $\{d\}$ can be expressed as

$$\{d\} = [\phi]\{q\} \quad (4)$$

where $[\phi]$ is the modal matrix and $\{q\}$ is the generalized displacement vector. The final matrix form of the aeroelastic

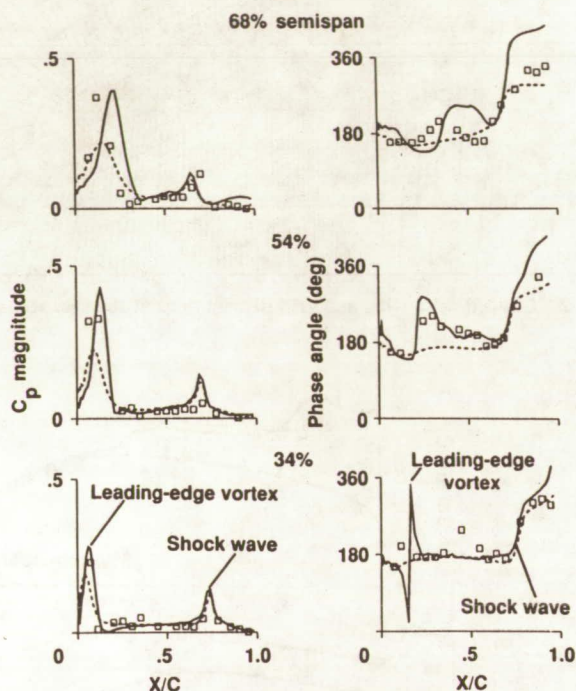


Fig. 4 Comparison of computed unsteady pressures using the standard and modified Baldwin-Lomax turbulence models with experiment, $M_\infty = 0.90$, $\alpha_m = 3.97$, $\bar{\alpha} = 0.46$, $Re_c = 17.6 \times 10^6$, $k = 0.5919$. —, Modified; ---, unmodified; \square , experiment, NASA TP-2594.

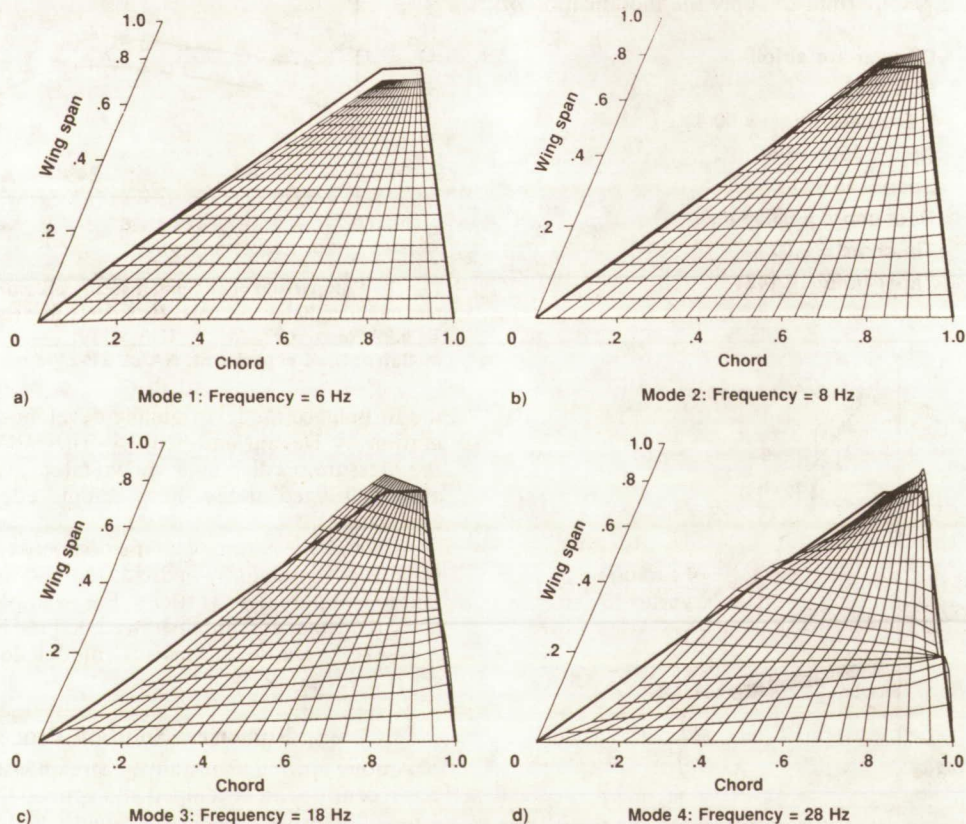


Fig. 5 First four mode shapes and frequencies of clipped delta wing.

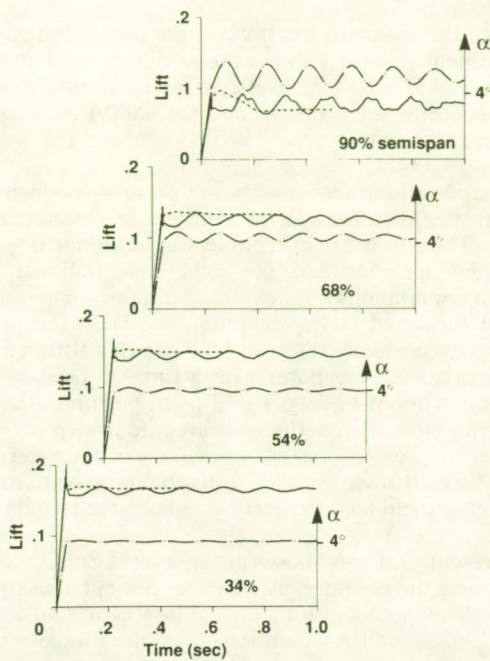


Fig. 6 Comparison of sectional lift responses between rigid and flexible wings in 4-deg ramp motion, $M_\infty = 0.90$, $Re_c = 15.0 \times 10^6$, $A = 0.04$. —, Flexible; ---, rigid; - · -, α (rigid + elastic).

equations of motion is

$$[M]\{\ddot{q}\} + [G]\{\dot{q}\} + [K]\{q\} = \{F\} \quad (5)$$

where $[M]$, $[G]$, and $[K]$ are modal mass, damping, and stiffness matrices, respectively. $\{F\}$ is the aerodynamic force vector defined as $(\frac{1}{2})\rho U_\infty^2 [\phi]^T [A] \{\Delta C_p\}$ and $[A]$ is the diagonal area matrix of the aerodynamic control points.

The aeroelastic equation of motion [Eq. (5)] is solved by a numerical integration technique based on the linear acceleration method.¹⁷

Aeroelastic Configuration Adaptive Grids

One of the major deficiencies in computational aerodynamics using the Navier-Stokes equations lies in the area of grid generation. For steady flows, the advance techniques such as zonal grids¹⁸ are being used. Grid generation techniques for aeroelastic calculations, which involve moving components, are in early stages of development. In Ref. 7, aeroelastic configuration adaptive dynamic grids were successfully used for computing time-accurate aeroelastic responses of swept wings. In this work, a similar technique is used.

Results

Numerical schemes used for flow calculations in aeroelasticity must guarantee the correct calculation of amplitude and phase of unsteady pressures. To verify the accuracy of the present code for simulating the complicated flowfield containing a leading-edge vortex and a shock wave, test cases are

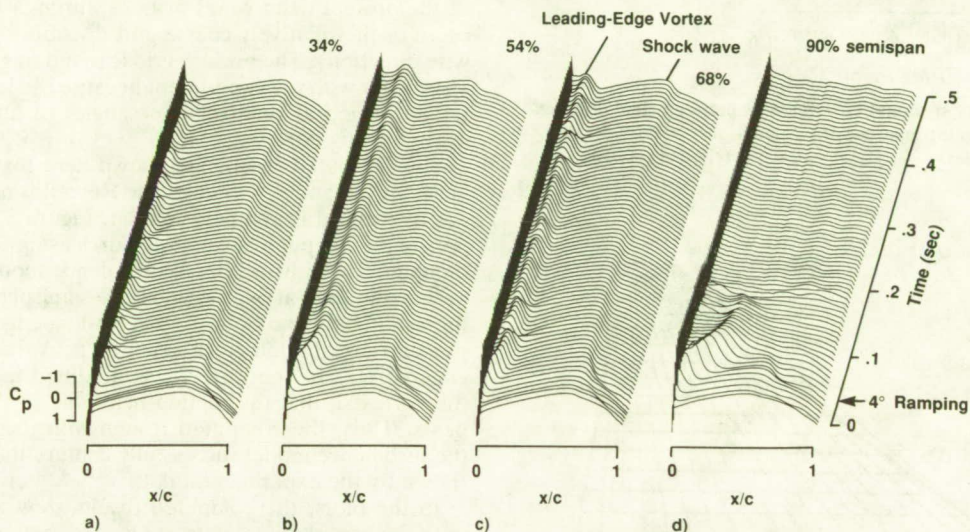


Fig. 7 Unsteady upper surface pressure responses of rigid wing in 4-deg ramp motion, $M_\infty = 0.90$, $Re_c = 15.0 \times 10^6$, $A = 0.04$.

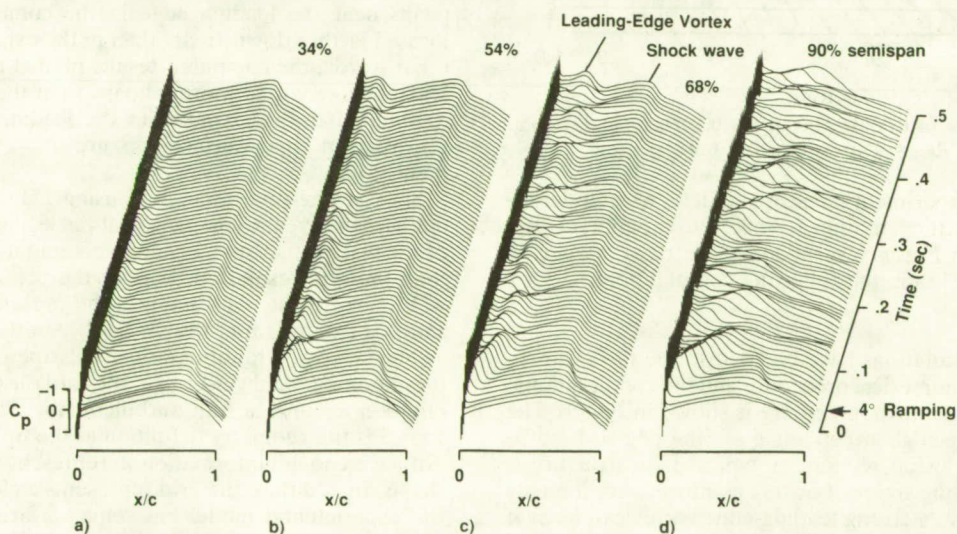


Fig. 8 Unsteady upper surface pressure responses of flexible wing in 4-deg ramp motion, $M_\infty = 0.90$, $Re_c = 15.0 \times 10^6$, $A = 0.04$.

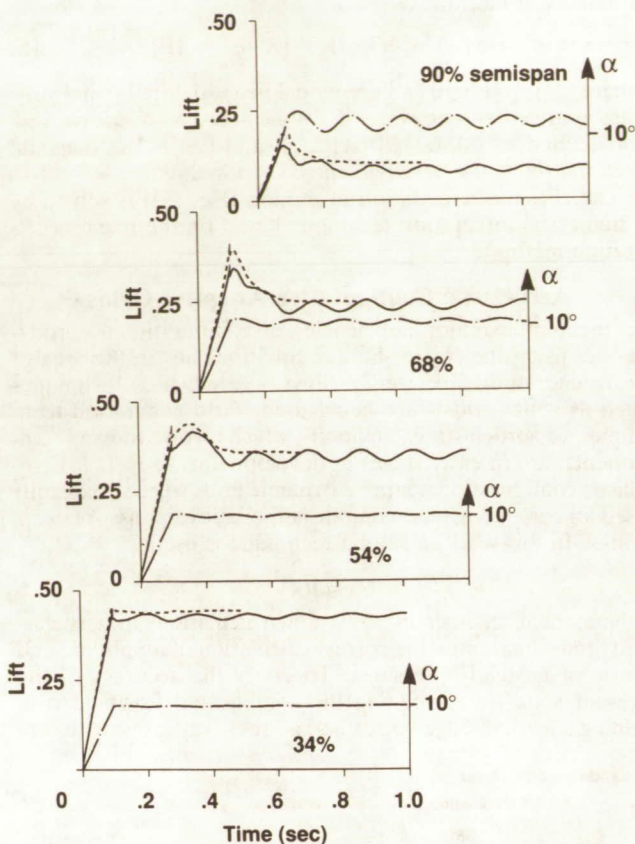


Fig. 9 Comparison of sectional lift responses between rigid and flexible wings in 10-deg ramp motion, $M_\infty = 0.90$, $Re_c = 15.0 \times 10^6$, $A = 0.04$. —, Flexible; ---, rigid; -.-, α (rigid + elastic).

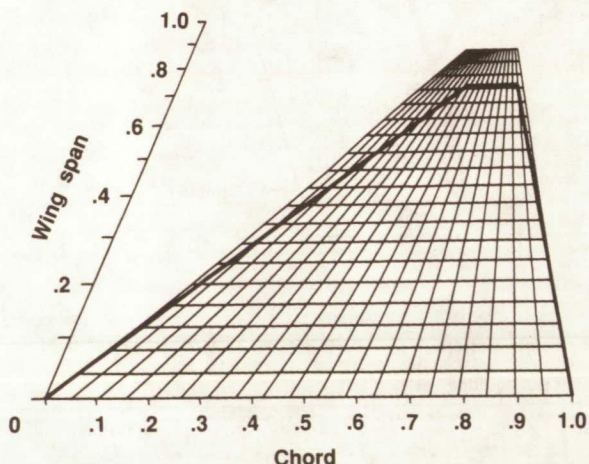


Fig. 10 Deformation of flexible wing at $t = 0.107$ s in 10-deg ramp motion, $M_\infty = 0.90$, $Re_c = 15.0 \times 10^6$, $A = 0.04$.

chosen from the experiment on a clipped delta wing undergoing prescribed pitching motion.⁹ Since the experiment was conducted using a Freon test medium, the ratio of specific heats γ is set to 1.135 in the following computations.

Steady Pressures

Steady-state calculations have been performed to examine the validity of the numerical procedure and the computational grid. The model planform geometry is shown in Fig. 1. The wing has a leading-edge sweep angle of 50.4 deg and a 6%-thick circular-arc airfoil section. A typical flow structure is also illustrated in the figure. For this planform with a highly swept leading edge, a strong leading-edge vortex can form at moderate angles of attack. This vortex can interact with a shock wave at transonic Mach numbers. The lines, A, B, and

C, indicate the spanwise locations of the pressure orifices in the experiment. Figure 2 shows the grid generated algebraically in the C-H topology. The ξ , η , and ζ coordinates represent the chordwise, spanwise, and normal (to the wing surface) directions, respectively. The grid contains $151 \times 25 \times 34$ points.

The present grid has less number of grid points when compared with the grids used in the typical steady-state computations.¹⁻³ The number of grid points was determined to compromise the accuracy and the total computational time. Unsteady computations require an order more computational time than the steady-state computations. With the present grid, a typical unsteady case can be computed within 5 h by using a Cray YMP computer with a single processor. (The code requires about $19 \mu\text{s}$ per grid point per time step for a flexible-wing case.) Then, three different time-step sizes were tried for each case to check the dependency on time-step sizes. Thus, in total, it took about 17 h to complete one unsteady pitching case including the corresponding steady-state computation.

The present grid was chosen from several candidate grids by comparing the pressure distributions computed using each grid with the experiment for a typical flow condition containing both a leading-edge separation and a shock wave at steady state. Among those grids, the H-O grid topology was also considered. However, the results showed that it did not have any advantage over the C-H grid topology either in capturing a leading-edge vortex (because of the moderate sweep angle of the present delta wing) or in capturing a shock wave (because of the relatively coarse grid distribution in the streamwise direction). The present grid is found to give a reasonable agreement with the experiment because the leading-edge vortex is formed at relatively low angles of attack due to the sharp leading edge.

The computed results are shown here for flow conditions at $M_\infty = 0.9$ and $\alpha = 4$ deg. The Reynolds number based on the root chord is about 17 million. Figure 3 shows the comparison of computed steady pressures using the modified and unmodified Baldwin-Lomax turbulence models with the experimental data at 34, 54, and 68% semispan sections. Since the modification accounts for the leading-edge separation, the pressure distribution gives a suction peak due to the leading-edge vortex. In contrast, the unmodified model smears out the vortex so that the suction peak due to the vortex disappears. Thus, the computed results with the modification of the turbulence model successfully capture the flow structures shown by the experimental data.

In the plots, the computed results show good agreement with the experimental data at inboard sections. On the other hand, the comparisons at the outboard section show that the peaks near the leading edge in the computed profiles are located farther downstream than in the experimental data. In other words, the computed results predict the location of the leading-edge vortex more inboard than the experiment. (As a result of the discrepancy in the leading-edge region, the downstream upper-surface pressure shows a minor disagreement, too.)

Since a fine-grid calculation using $151 \times 41 \times 41$ points did not improve the comparison at the leading edge, the source of the discrepancy may be in the computational model rather than the grid resolution. One of the possible sources is the wall effect of the wind tunnel. The present computation assumes a freestream at the far field. Another source is use of a boundary-layer transition strip in the experiment. Even though the modified Baldwin-Lomax model is used here, the computation assumes a fully turbulent flow. The other possible source is the geometry definition at the tip. The report⁹ does not have enough information to represent a detailed wing tip shape. In addition, the grid represents a clean wing, whereas the experimental model has some surface irregularities because of control surfaces both at the leading edge and at the trailing edge.

In Ref. 19, four steady-state cases are computed for flow conditions at $M_\infty = 0.88$ and 0.9 with angles of attack $\alpha = 3$ and 4 deg. The experimental data do not show the presence of a shock wave at $M_\infty = 0.88$. With an increase of the Mach number from 0.88 to 0.9 , a shock wave is formed on the upper surface of the wing. On the other hand, an increase in the angle of attack from 3 to 4 deg at a fixed Mach number primarily affects the strength of the leading-edge vortex. The computed results successfully represent the effects of the different Mach numbers and the different angles of attack.

Rigid Pitching Motion

The unsteady data are given for the case when the rigid wing is oscillating in a pitching mode, $\alpha(t) = \alpha_m - \bar{\alpha} \sin(\omega t)$, about an axis at 65.22% root chord, where ω is the circular frequency in radians per second. The test cases consider four flow conditions at $M_\infty = 0.88$ and 0.9 with mean angles of attack $\alpha_m = 3$ and 4 deg, a pitch amplitude $\bar{\alpha} = 0.5$ deg, and a frequency of 8 Hz that corresponds to a reduced frequency of $k = 0.6$ ($k = \omega c / U_\infty$ where c is the root chord).

Unsteady computations are started from the corresponding steady-state solutions. The number of time steps per cycle of 3600 was chosen from the numerical experiments to assure the time accuracy (the typical time-step size was about 3.3×10^{-3}). The convergence of the unsteady computations to a periodic flow is verified by comparing the results between cycles. The third-cycle results are shown in the following. The numerical transient is confirmed to disappear within two cycles.

Figure 4 shows the comparison of computed unsteady pressures using the modified and unmodified Baldwin-Lomax turbulence models with the experimental data at $M_\infty = 0.9$ and $\alpha_m = 4$ deg, corresponding to Fig. 3. The plots show the comparison of the magnitude and phase angle between the computed and measured unsteady upper surface pressure coefficients of the wing at 34 , 54 , and 68% semispan sections. Both the leading-edge vortex and the shock wave produce a peak in magnitude and a jump in phase angle. Since the unmodified model gave almost two orders of magnitude higher turbulent viscosity at the leading edge, the solution became highly dissipative and thus did not show any large changes in unsteady pressures. (In Fig. 4a, the modified turbulence model predicts a larger phase change than the experiment near $x/c = 0.15$. This is partly due to the conversion of unsteady pressures from real and imaginary to magnitude and phase angle.) The improvements due to the modification of the

turbulence model are seen in both magnitude and phase angle where the leading-edge vortex exists. Consistent to the steady pressures, the peaks near the leading edge in the computed profiles are located more downstream than the experimental data at the outboard sections. Overall, the numerical results show fairly good agreement with the experimental data. The present grid leads to reasonable resolution for the present unsteady flowfields, even though the grid is fairly coarse.

Throughout the four test cases presented in Ref. 19, the modified turbulence model predicted higher peaks in magnitude and larger changes in the phase angle at the leading-edge vortex and thus agreed with the experiment better than the unmodified model. The effect of Mach numbers on the shock wave and the effect of angles of attack on the vortex were consistent to the steady-state results.

Rigid and Flexible Ramp Motions

In maneuvering, aircraft often undergo rapid ramp motions. During such motions, flow unsteadiness and wing flexibility play important roles. In this section, the applicability of the present development to computing such flowfields is demonstrated.

Computations are performed for rigid and flexible wings in ramp motion. Structural properties of the wing were selected to represent a typical fighter wing. Figure 5 shows the mode shapes and the frequencies of the first four normal modes for the clipped delta wing used in the following computations. The dynamic pressure is set to be 1.0 psi. Test cases consider 4 - and 10 -deg ramp motions from 0 -deg angle of attack for both rigid and flexible wings.

4-Deg Ramp Motion

Figure 6 shows the comparisons of the sectional lift responses between the rigid and flexible wings at $M_\infty = 0.9$ and $Re_c = 15 \times 10^6$ for the wing ramping up to 4 deg with a pitch rate of $A = 0.04$. The pitch rate A is defined as $\dot{\alpha}c/U_\infty$. The variation of the effective angle of attack including both the ramp angle and the flexible angle of attack is also shown for the flexible-wing case. The data are plotted at 34 , 54 , 68 , and 90% semispan sections. The unsteady computations are started from the converged steady-state solution at 0 -deg angle of attack.

In the rigid-wing case, the lift responses at the inboard sections settle down quickly after the ramp motion stops, and the flow approaches the steady-state values. (Thus the com-

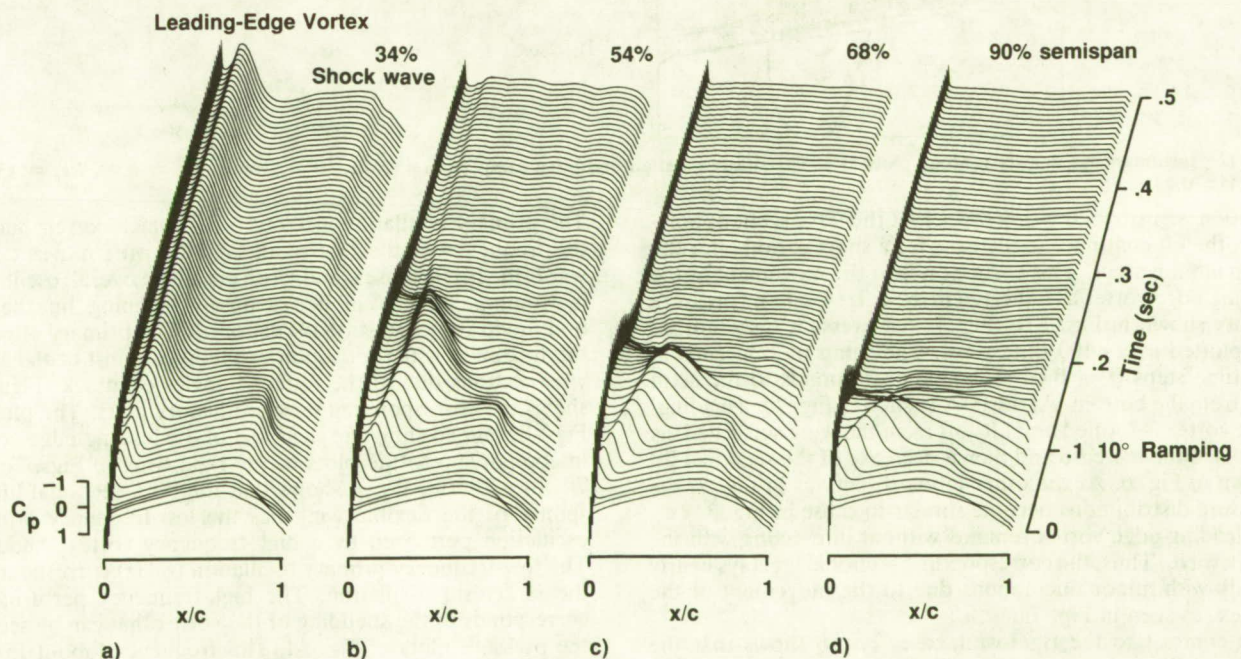


Fig. 11 Unsteady upper surface pressure responses of flexible wing in 10 -deg ramp motion, $M_\infty = 0.90$, $Re_c = 15.0 \times 10^6$, $A = 0.04$.

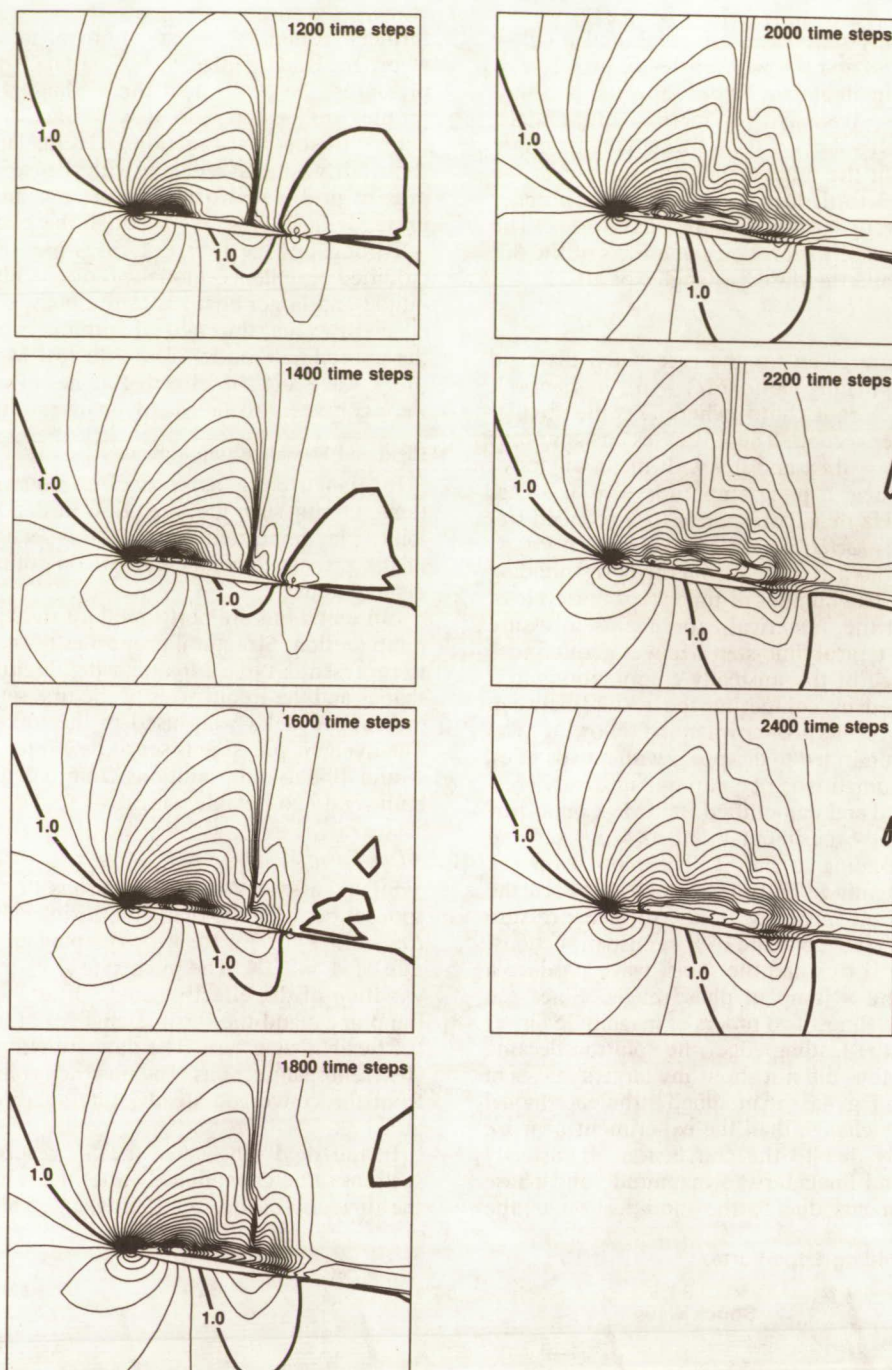


Fig. 12 Instantaneous density contour plots at 68% semispan section in 10-deg ramp motion ($0.08 < t < 0.16$ s), $M_\infty = 0.90$, $Re_c = 15.0 \times 10^6$, $A = 0.04$.

putation was stopped at $t \approx 0.5$ s.) At the 90% section, however, the lift continues to increase for a short period after the ramp motion stops. This corresponds to the movement of the leading-edge vortex as indicated in the corresponding pressure history shown in Fig. 7. In Fig. 7, the pressure distributions are plotted every 100 time steps. The ramp motion ends at 600 time steps ($t = 0.04$ s), which corresponds to the sixth plot from the bottom. At the 90% section in Fig. 7d, a leading-edge vortex is formed and lifts off from the wing surface. This results in the increase and then a decrease of the sectional lift shown in Fig. 6. At the other inboard sections in Fig. 7, the pressure distributions become similar to those in Fig. 3, i.e., the leading-edge vortex remains without interacting with the shock wave. Thus, the corresponding sectional lift stays nearly steady with minor fluctuations due to the movement of the vortex, as seen in Fig. 7a.

In contrast to the rigid-wing case, Fig. 6 shows that the sectional lift responses of the flexible wing are oscillatory.

The primary oscillation is about 6 Hz, which corresponds to the frequency of the first mode. As the wing moves downward, the lift increases, and vice versa. The overall oscillation is damping. The first mode response is damping, but the second mode response stays oscillatory.¹⁹ The primary effect of the flexibility is the reduction of the lift at most of the spanwise sections due to the reduced angles of attack. Figure 8 shows the corresponding pressure history plots. The plots in Figs. 8c and 8d show the shedding of the leading-edge vortex in comparison to the plots of the rigid wing in Figs. 7c and 7d. In addition, Fig. 6 shows that the 90% sectional lift response of the flexible wing has the low-frequency primary oscillation perturbed by a high-frequency vortex shedding. The low-frequency primary oscillation (6 Hz) corresponds to the structural oscillation. The high-frequency perturbation corresponds to the shedding of the vortex that can be seen in the pressure plots of Fig. 8d. This frequency (about 15 Hz) does not excite any structural mode as shown in Fig. 5.

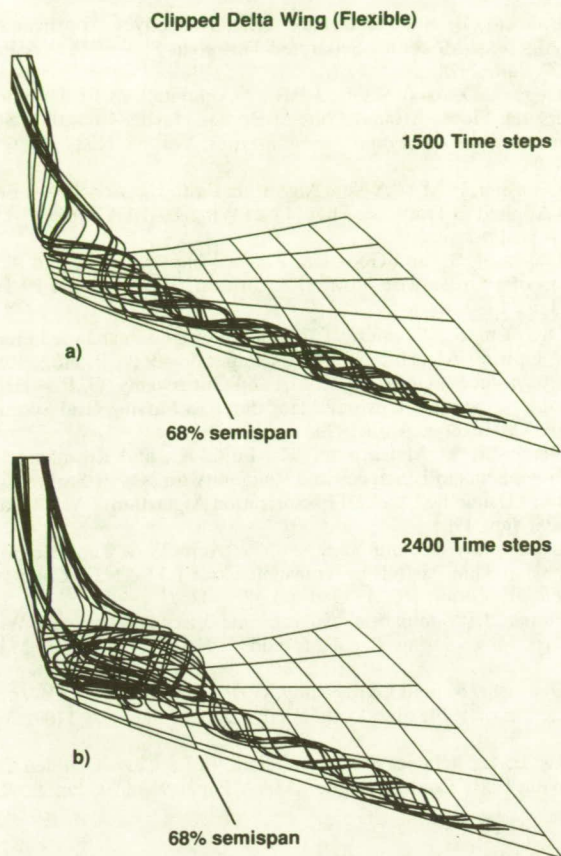


Fig. 13 Streamline pattern over the upper surface of flexible wing in 10-deg ramp motion, $M_\infty = 0.90$, $Re_c = 15.0 \times 10^6$, $A = 0.04$. a) $t = 0.10$ s, and b) $t = 0.16$ s.

Computations (not shown) were also carried out for the flexible-wing ramping from 0 to 3 deg and from 0 to 5 deg at the same pitch rate as the 4-deg case. The 4-deg case shows the largest high-frequency perturbation. In the 3-deg case, the vortex is not strong enough to disturb the lift response. The vortex shedding is found only at the 90% section. In the 5-deg case, the vortex lifts off from the wing surface so that the structural oscillation does not cause the perturbation seen at the lower angles of attack. The 10-deg case discussed in the next section does not show the perturbation either.

A reduction of the local angle of attack due to the flexibility of the wing results in a delay of the lift increase for a short period after the ramp motion stops (about $0.04 < t < 0.11$ in Fig. 6). The wing is deformed upward in bending and leading-edge down in twisting. When the ramp motion stops, the wing is still deforming, which also gives a dynamic effect. Thus the local angle of attack relative to the wing section decreases toward the wing tip and the leading-edge vortex appears weaker in the flexible-wing case. This leads to the delay of the lift increase in the flexible-wing case.

10-Deg Ramp Motion

The sectional lift responses for the 10-deg ramp motion at several spanwise sections are shown in Fig. 9. The computations are again started from the steady-state solution at 0-deg angle of attack. The unsteady increase of the lift is observed more widely in both rigid and flexible cases than the 4-deg case. The sectional lift at the 90% section indicates a stall before reaching 10-deg angle of attack for both rigid and flexible wings. Instead, the plot does not have any significant perturbations. The flexible wing gives lower lift because of the deformation of the wing similar to the 4-deg case. After the initial lift increase, the lift oscillates due to the structural oscillation. Again, the first mode response is damping, but the second mode response stays oscillatory.¹⁹ Figure 10 shows

the magnified deformation of the wing at 1600 time steps (the ramp motion ends at 1500 time steps: $t = 0.10$ s). The actual displacement of the leading edge at the wing tip is 1.7% of the root chord length.

Figure 11 shows the corresponding pressure history plots of every 100 time steps for the flexible-wing case. In contrast to the 4-deg case, the deformation of the wing does not affect the flowfield as strongly because the leading-edge vortex lifts off from the wing surface at the outboard sections. The flexibility does not play an important role at the inboard sections, because the wing root is fixed. Thus there is no significant difference in the responses between the rigid and flexible wings. At the most inboard section in Fig. 11, the pressure distributions show no interaction of the leading-edge vortex with the shock wave. At the 54% section, both vortex and shock wave develop, then both disappear. At the 68% section, a similar but more rapid change occurs. This rapid reduction of the lift indicates a vortex breakdown.

To see the interaction of the leading-edge vortex with the shock wave, the density contours at the 68% section are plotted every 200 time steps from 1200 to 2400 time steps ($0.08 < t < 0.16$) in Fig. 12. First, there is no interaction between the vortex and the shock wave. As the vortex develops, it moves toward the trailing edge, that is, toward the shock wave. When the vortex starts to interact with the shock wave, the shock wave starts to ride on the shear layer and to form a lambda-type shock wave. At this point, the shock wave disappears from the surface pressure plots. As the front shock grows, the flow separation grows and the vortex core bursts quickly. Simultaneously, the rear shock weakens. Finally, the fully separated flow is observed. The corresponding contour plots of the negative u component in Ref. 19 show that a negative u region appears as the vortex is deformed by the strong front shock at 2000 time steps ($t \approx 0.13$ s). As the vortex core diffuses, the reverse flow region grows. The shock wave plays an essential role in the process of this breakdown.

Figure 13 shows plots of the streamline pattern at 1500 and 2400 time steps ($t = 0.10, 0.16$ s, respectively). At 1500 time steps, when the ramp motion has just ended, a leading-edge separation is formed over the entire span. Although it is not clear from the plots, the vortex starts bursting near the tip as indicated in Fig. 11d. In contrast, at 2400 time steps, a bubble-type breakdown is clearly observed in the middle of the span. The breakdown grows toward the upstream slowly. Then the flow reaches the nearly steady state.

Although no corresponding experiment was performed for the present wing at this angle of attack, Ref. 20 reported a vortex breakdown about a similar wing at similar flow conditions, including a comparison with the experiment.

Concluding Remarks

In this paper, a computational procedure for computing the unsteady transonic flows associated with the leading-edge vortex on a clipped delta wing, including flexibility, has been presented. The procedure is based on a time-accurate computational method combined with the use of aeroelastically adaptive dynamic grids. The flow is modeled using the Navier-Stokes equations. The flow equations are coupled with the structural equations to account for the flexibility. The numerical procedure has been verified through the comparisons with the experiment for the unsteady pitching cases on the rigid clipped delta wing. The main flow structures are successfully captured.

The ramp motion cases have demonstrated the effects of unsteadiness of the flow field and flexibility of the wing. The primary effect of the flexibility is the reduction of the lift due to the deformation of the wing. Interaction of the leading-edge vortex with the shock wave has significant effects on the wing responses. For the 4-deg ramp motion, the vortex shedding occurs at the wing tip due to the flexibility. For the 10-deg ramp motion, a possible vortex breakdown is observed. The inviscid interaction with the shock wave plays an essential

role in the process of the breakdown observed in the present calculation.

References

- ¹Fujii, K., and Schiff, L. B., "Numerical Simulation of Vortical Flows over a Strake-Delta Wing," *AIAA Journal*, Vol. 27, No. 9, 1990, pp. 1153-1162.
- ²Taylor, S. L., Kjelgaard, S. O., Weston, R. P., Thomas, J. L., and Sellers, W. L., III, "Experimental and Computational Study of the Subsonic Flow About a 75° Swept Delta Wing," AIAA Paper 87-2425, Aug. 1987.
- ³Ekaterinaris, J. A., and Schiff, L. B., "Numerical Simulation of the Effects of Variation of Angle of Attack and Sweep Angle on Vortex Breakdown over Delta Wings," AIAA Paper 90-3000-CP, Aug. 1990.
- ⁴Kandil, O. A., and Chuang, H. A., "Computation of Vortex-Dominated Flow for a Delta Wing Undergoing Pitching Oscillation," *AIAA Journal*, Vol. 28, No. 9, 1990, pp. 1589-1595.
- ⁵Guruswamy, G. P., "Vortical Flow Computations on Swept Flexible Wings Using Navier-Stokes Equations," AIAA Paper 89-1183, April 1989.
- ⁶Guruswamy, G. P., "Unsteady Aerodynamic and Aeroelastic Calculations of Wings Using Euler Equations," *AIAA Journal*, Vol. 28, No. 3, 1990, pp. 461-469.
- ⁷Guruswamy, G. P., "Navier-Stokes Computations on Swept-Tapered Wings, Including Flexibility," AIAA Paper 90-1152, April 1990.
- ⁸Obayashi, S., Guruswamy, G. P., and Goorjian, P. M., "Application of a Streamwise Upwind Algorithm for Unsteady Transonic Computations over Oscillating Wings," AIAA Paper 90-3103, Aug. 1990.
- ⁹Hess, R. W., Cazier, F. W., Jr., and Wynne, E. C., "Steady and Unsteady Transonic Pressure Measurements on a Clipped Delta Wing for Pitching and Control-Surface Oscillations," NASA TP-2594, Oct. 1986.
- ¹⁰Baldwin, B. S., and Lomax, H., "Thin-Layer Approximation and Algebraic Model for Separated Turbulent Flows," AIAA Paper 78-257, Jan. 1978.
- ¹¹Degani, D., and Schiff, L. B., "Computations of Turbulence Supersonic Flows Around Pointed Bodies Having Crossflow Separation," *Journal of Computational Physics*, Vol. 66, No. 1, 1986, pp. 173-196.
- ¹²Goorjian, P. M., "A New Algorithm for the Navier-Stokes Equations Applied to Transonic Flows Over Wing," AIAA Paper 87-1121-CP, June 1987.
- ¹³Obayashi, S., and Goorjian, P. M., "Improvements and Applications of a Streamwise Upwind Algorithm," AIAA Paper 89-1957-CP, June 1989.
- ¹⁴Obayashi, S., "Numerical Simulation of Underexpanded Plumes Using Upwind Algorithms," AIAA Paper 88-4360-CP, Aug. 1988.
- ¹⁵Obayashi, S., Goorjian, P. M., and Guruswamy, G. P., "Extension of a Streamwise Upwind Algorithm to a Moving Grid System," NASA TM-102800, April 1990.
- ¹⁶Obayashi, S., Matsushima, K., Fujii, K., and Kuwahara, K., "Improvements in Efficiency and Reliability for Navier-Stokes Computations Using the LU-ADI Factorization Algorithm," AIAA Paper 86-0338, Jan. 1986.
- ¹⁷Guruswamy, P., and Yang, T. Y., "Aeroelastic Time Response Analysis of Thin Airfoils by Transonic Code LTRAN2," *Computers and Fluids*, Vol. 9, No. 4, 1980, pp. 409-425.
- ¹⁸Flores, J., "Simulation of Transonic Viscous Wing and Wing-Fuselage Flows Using Zonal Methods," NASA TM-89421, March 1987.
- ¹⁹Obayashi, S., and Guruswamy, G. P., "Unsteady Shock-Vortex Interaction on a Flexible Delta Wing," AIAA Paper 91-1109, April 1991.
- ²⁰Tu, E. L., "Navier-Stokes Simulation of a Close-Coupled Canard-Wing-Body Configuration," AIAA Paper 91-0070, Jan. 1991.

APPENDIX C



AIAA-92-4431

**Navier-Stokes Computations for
Oscillating Control Surfaces**

S. Obayashi and G. Guruswamy
NASA Ames Research Center
Moffett Field, CA

**AIAA Atmospheric Flight
Mechanics Conference**

August 10-12, 1992 / Hilton Head Island, SC

Navier-Stokes Computations for Oscillating Control Surfaces

Shigeru Obayashi* and Guru P. Guruswamy**

NASA Ames Research Center, Moffett Field, California, 94035-1000

Abstract

Unsteady Navier-Stokes computations have been performed for simulating transonic flows over wings with oscillating control surfaces using a locally moving grid and a stationary-mismatched zoning scheme. An F-5 wing and a clipped delta wing are chosen for the present study. The computed unsteady pressures and the response characteristics to the control surface motions are compared with experimental data. The results successfully predict main features of the unsteady pressure profiles, such as the double peaks at the shock wave and at the hinge line.

Introduction

Aircraft are often subject to aerodynamic oscillation, especially in the transonic regime, because of flow nonlinearities and the presence of the moving shock waves. In this unsteady aerodynamics environment, aircraft rely heavily on active controls for safe and steady flight operation. Active control is also needed for the suppression of structural flutter and the reduction of structural weight to achieve stable flight conditions.

The influence of control surfaces on both aerodynamics and aeroelastic performance of a wing is more pronounced in the transonic regime. These influences can be constructively used to improve the wing performance through proper maneuvering of the active control surfaces. Active control technology relies on accurate predictions of unsteady aerodynamics and aeroelastic performance of a wing. Since the experimental evaluation of the effect of a control surface on the wing performance would involve considerable cost and the risk of structural damage in a wind tunnel, it is necessary to initiate the investigation through theoretical analyses.

The theoretical analysis of transonic flows is complicated by the presence of mixed subsonic and supersonic regions within the flow field. For an unsteady

flow field, such as that surrounding a control surface, additional considerations are needed to treat moving shock waves of varying strength and subsequent flow separation induced by the shock-wave/boundary-layer interactions. For the case of the control surface in which viscous effects dominate, computation based on the unsteady Navier-Stokes equations is needed.

The physics of unsteady transonic flow around a control surface has been simulated at various levels of inviscid and viscous approximations using small disturbance theory^{1,2} and, for limited two-dimensional cases, the unsteady Navier-Stokes equations.^{3,4} The purpose of this study is to explore the capability of three-dimensional Navier-Stokes simulation for the unsteady flow field surrounding a wing with an oscillating control surface.

The present investigation is initiated in conjunction with a recently developed code, ENSAERO, which is capable of computing aeroelastic responses by simultaneously integrating the Euler/Navier-Stokes equations and the modal structural equations of motion using aeroelastically adaptive dynamic grids.⁵⁻⁸ The code has been applied to transonic flows from small to moderately large angles of attack for fighter wings undergoing unsteady motions. In this paper, the geometric capability of the code is extended to simulate unsteady flows over a rigid wing with an oscillating trailing-edge flap.

To model an oscillating control surface efficiently, an algebraic grid generation technique is incorporated into the code. The grid moves every time step to follow the deflection of the control surface. Small deflections are handled using a sheared single grid, and large deflections are handled using a zonal technique.⁹

In this paper, the first test case considers transonic flows over an F-5 wing with an oscillating inboard control surface. The same case was simulated using small disturbance theory in Ref. 2. The second case considers transonic vortical flows over a clipped delta wing. Unsteady Navier-Stokes computations for the clean wing were reported in Ref. 8. The mismatched zonal cases are demonstrated for this case.

* Senior Research Scientist, MCAT Institute, San Jose, California. Senior Member AIAA.

** Research Scientist, Associate Fellow AIAA.

Copyright © 1992 by the American Institute of Aeronautics and Astronautics, Inc. No copyright is asserted in the United States under Title 17, U.S. Code. The U.S. Government has a royalty-free license to exercise all rights under the copyright claimed herein for Governmental purposes. All other rights are reserved by the copyright owner.

Numerical Method

Governing Equations and Discretization

The nondimensionalized Reynolds-averaged thin-layer Navier-Stokes equations used in this study can be written in conservation-law form in a generalized body-conforming curvilinear coordinate system for three dimensions as follows:

$$\partial_\tau \hat{Q} + \partial_\xi \hat{E} + \partial_\eta \hat{F} + \partial_\zeta \hat{G} = \frac{1}{Re} \partial_\zeta \hat{G}^v \quad (1)$$

where $\tau = t$, $\xi = \xi(x, y, z, t)$, $\eta = \eta(x, y, z, t)$, and $\zeta = \zeta(x, y, z, t)$. In the present paper, the ξ and η directions are along the streamwise and spanwise directions, respectively, of a wing. The viscous derivatives associated with these directions are dropped. The ζ direction is normal to the wing surface, and thus the viscous derivatives are retained.

In Eq. (1), \hat{Q} is the vector of conserved quantities, \hat{E} , \hat{F} and \hat{G} are the inviscid flux vectors, and \hat{G}^v is the thin-layer viscous flux vector. The viscosity coefficient in \hat{G}^v is computed as the sum of the laminar and turbulent viscosity coefficients where the laminar viscosity is taken from the freestream laminar viscosity, assumed to be constant for transonic flows. As an option, Sutherland's law can be used to calculate the laminar viscosity. The turbulent viscosity is evaluated by the Baldwin-Lomax algebraic eddy-viscosity model.¹⁰ Since the flow field to be considered in this paper contains leading-edge separation, it is important to apply a modification to the turbulence model originally developed for crossflow-type separation.¹¹

In this study, a conventional finite-difference (FD) grid system is used. However, for the moving grid case, it is important to treat the time metrics correctly. The FD formulation does not give freestream-capturing time metrics.^{12,13} The FD time metrics are related to the grid velocity, for example,

$$\xi_t = -\xi_x x_t - \xi_y y_t - \xi_z z_t \quad (2)$$

For rigid motion of the grid, the freestream can be preserved by applying a freestream subtraction technique to the time metric terms.

In the FV formulation, the right-hand side of Eq. (2) is expressed as a product of a surface vector and a grid velocity. The time integration of the product from time level n to $n+1$ represents a volume swept by the surface during one time step. By computing this volume, $V_{\xi n}^{n+1}$, the freestream-capturing time metrics can be obtained as

$$\frac{\xi_t}{J} = -\frac{V_{\xi n}^{n+1}}{\Delta t} \quad (3)$$

See Ref. 13 for more details. Because control surfaces oscillating at a small amplitude were considered in this paper, the FD and FV formulas did not produce any significant difference in the results.

Upwind Algorithm

Several numerical schemes have been developed to solve Eq. (1). The present code has two different schemes: the central-difference and streamwise upwind schemes. In this work, a streamwise upwind algorithm is applied to compute the inviscid cell-interface fluxes. The streamwise upwind algorithm has recently been developed and applied to steady and unsteady problems of transonic flows over wings, including flexibility of the wing.^{7,8} A third-order evaluation is used for the inviscid term. A second-order central-difference evaluation is applied to the viscous term. The complete algorithm can be found in Ref. 7.

An implicit method is used for the time integration because it is more suitable for expensive unsteady viscous calculations. The method chosen for the upwind scheme is the LU-ADI (lower-upper factored, alternating direction implicit) method.¹⁴ The method is first-order accurate in time and requires only scalar bidiagonal matrix inversions. See Refs. 14 and 15 for additional details.

Specific code performance information for the current study is given as follows. All results were computed on either a CRAY-YMP or CRAY-2 computer at NASA Ames Research Center. The performance of the upwind version of ENSAERO is 170 MFLOPS and 19 μ sec per iteration per grid point on a single CRAY-YMP processor.

Control Surface Grid

In this paper, a single C-H topology grid for a wing with a control surface is used. In each C grid section, a two-dimensional algebraic grid generation technique is applied to each airfoil section.¹⁶ At both ends of the control surface, a small gap is introduced (Fig. 1). This region is used to shear the grid when the control surface oscillates. Although the gap is introduced to simplify the calculations, its effect can be minimized by clustering the grid in this region.

The C grid around a deflected control surface can be obtained in two ways. One is to shear every grid line normal to the control surface with the local deflection, Δx and Δz . The other is to regenerate the entire C grid with the control surface deflected at every time step. The computational overhead of the latter approach is only 7% because of the efficient algebraic grid generation scheme. However, the computed surface pressures did not show any differences between the two methods. Thus, the results

presented in this paper were computed using the shearing technique.

Zonal Grid Capability

The present code inherits the zonal grid capability developed for the Transonic Navier-Stokes (TNS) code to handle complicated geometries, such as complete aircraft configurations.⁹ Although a problem with the extension of the zonal method to unsteady flows was reported in a previous paper,¹⁷ a code error was found and has been corrected. In the present study, the corrected code is used.

In this paper, a mismatched zoning scheme is introduced to accommodate large mean flap deflections, while a shearing-grid technique is used to model an oscillating flap about the mean deflection. Zonal interfaces are located at both ends of a control surface including the gap (Fig. 2). As the control surface deflects, the grids become mismatched. However, if the zonal interfaces move, it requires expensive computation to find interpolation coefficients on the mismatched zones at every time step. To maintain the efficiency of the single-grid computation, the zonal interfaces should remain stationary when the control surface oscillates with a small amplitude. Instead, the control surface grid shears at the gap region similar to the single-grid case. To transfer the flow information from one grid to another, bilinear interpolation is used here (see the nonconservative interpolation in Ref. 18), because the present zonal interfaces are coplanar. Although the present interpolation is explicit and nonconservative, the error can be ignored when practical time-step sizes for Navier-Stokes computations are used.

A different zonal approach is reported in Ref. 19 to treat a stationary, deflected flap. Its extension to oscillating control surfaces will be investigated in the near future.

Results

F-5 Wing

The first test considers unsteady viscous flows over an F-5 wing with an oscillating inboard control surface. This wing has an aspect ratio of 2.98, a taper ratio of 0.31 and a leading edge sweep angle of 31.92 deg. Computations were made using coarse and fine grids containing $151 \times 41 \times 34$ points and $201 \times 61 \times 34$ points, respectively. The wing planform is given in Fig. 3. It should be noted that the present C-H grid does not have enough resolution for the faired wing tip of the experimental model. The control surface is oscillating about an axis located at the 82% root chord, and the hinge axis is normal to the wing root. The test cases are at a Mach number of $M_\infty = 0.9$, where the experimental steady and unsteady data are given in Ref. 20. All F-5 wing cases are computed at a Reynolds number based on the root

chord of $Re_c = 12 \times 10^6$. Reference 2 discusses the small disturbance results applied to the same test case.

The response of surface pressure to the control surface motion can be represented in terms of real and imaginary parts of the first Fourier component of the unsteady pressures. In Fig. 4, the coarse- and fine-grid results are compared with experimental data at an angle of attack of $\alpha = 0$ deg with the control surface oscillating at a frequency of 20 Hz and an amplitude of $\beta = 0.5$ deg. This frequency corresponds to a reduced frequency of $k \approx 0.28$. Results are shown for the upper surface pressures at three spanwise locations. It is noted that for $M_\infty = 0.9$, the steady-state solution is shock-free except near the wing tip. The spikes in the unsteady pressure distributions around the 50% chord indicate the motion of the shock wave due to the control surface oscillation. The spikes are also seen at the hinge line. In the real part of the unsteady pressures, at the inboard sections, the computations predict higher spikes for the motion of the shock wave than observed in the experiment. This is because the computation assumes a plane of symmetry at the root section, while the experiment has a solid wall. In contrast, the computations predict lower spikes at the hinge line. This is because the present grid has constant chordwise distributions and thus does not align to the hinge line. In the imaginary part, there is a greater discrepancy between the computation and the experiment, which is possibly due to the resolution of the experimental data as shown later. The coarse- and fine-grid results show reasonably good agreement in Fig. 4.

The unsteady pressure profiles using time-step sizes yielding 1800 and 2400 steps/cycle were compared with each other to check the time-step dependency of the coarse-grid results. The unsteady results converged at 1800 steps/cycle and thus this time step was used for the F-5 wing results shown in this paper. The finite-difference time metrics, Eq. (2), and the freestream-capturing time metrics, Eq. (3), were checked on the coarse grid as well. No difference was found for this small amplitude of control surface oscillation.

Figure 5 shows the unsteady results on the coarse grid at 1.5 deg angle of attack with the flap oscillating at a frequency of 20 Hz and an amplitude of 0.5 deg at three spanwise locations. The real part of the unsteady pressures follows the previous observation for Fig. 4. The imaginary part shows better agreement at the outboard section than Fig. 4. Since the computed results show more consistent trends, the disagreement in the imaginary part is likely due to the resolution of the experimental data.

Clipped Delta Wing

The next test case considers a clipped delta wing with an oscillating trailing-edge control surface.²¹ The wing planform is shown in Fig. 6. The wing has a leading-edge sweep angle of 50.4 deg and a 6%-thick circular-arc airfoil section. At $M_\infty = 0.9$ and $\alpha = 3$ deg, both a leading-edge vortex and a shock wave are present on the upper surface

of the wing. The present C-H grid contains $151 \times 44 \times 34$ points (see Fig. 1). Since the experiment was conducted using a Freon test medium, the ratio of specific heats, γ , is set to 1.135 in the following computations. In addition, the modified Baldwin-Lomax model is used to account for the leading-edge vortex. Steady-state and rigid pitching calculations of this wing were reported in Ref. 8. Although three cases were computed for this oscillating control surface with an amplitude of 2.20, 4.38 and 6.65 deg, the 6.65-deg case is discussed in the following because the other two cases show similar trends.

Figure 7 shows the unsteady pressures with the control surface oscillating at a frequency of 8 Hz and an amplitude of 6.65 deg at $M_\infty = 0.9$, $\alpha = 3$ deg and $Re_c = 17 \times 10^6$ based on the root chord. Results are shown as magnitude and phase angle of the upper surface pressure responses at three spanwise sections. The magnitude part of the unsteady pressures shows significant influence of the control surface oscillation. At the 68% spanwise section, the plot shows double peaks, similar to the F-5 wing case. These correspond to the shock wave location and the control-surface hinge line. Although the computed result shows a much smaller peak due to the shock wave at the 68% section, it is consistent with the steady-state result where the shock wave appears weaker.⁸ This discrepancy originates in both the experimental and computational modeling. For example, there was a misalignment of the control surface on the order of 2 deg in the experiment.²¹ In contrast, the computed peak at the hinge line is much higher than the experiment. This is because the grid aligns to the hinge line in this case and the experimental data does not have enough resolution near the hinge line. The phase angle plots show a discrepancy near the leading edge. It should be noted that the computation assumes a fully turbulent flow while the experiment has a fixed transition at the 8 % chord. Overall, the computed results show reasonably good agreement with the experiment.

The test case presented in Fig. 7 was more sensitive to time-step sizes. Most of the unsteady pressures on the wing surface converged at 3600 steps/cycle (the same number as the rigid pitching case in Ref. 8). However, the oscillation of the control surface caused a minor fluctuation to the leading-edge vortex, and thus, the unsteady pressures under the leading-edge vortex required 5000 steps/cycle to converge.

Zonal Grid

The zonal test case is taken from the previous clipped delta wing. The control surface is deflected 6 deg and undergoes an oscillatory motion with an amplitude of 1 deg and a frequency of 8 Hz at $M_\infty = 0.9$, $\alpha = 0$ deg and $Re_c = 17 \times 10^6$. Since no experimental data is available for this particular case, zonal-grid results are compared with single-grid results.

First, the single grid of $151 \times 44 \times 34$ points is divided into three zones at the gaps at both ends of the

control surface. Each zone contains $151 \times 13 \times 34$, $151 \times 15 \times 34$, and $151 \times 20 \times 34$ points from inboard to outboard (see Fig. 2). Special attention is given to the generation of smooth zonal interfaces because the gap region often causes skewed grid distributions.

Figure 8 shows the comparison of steady-state results between the single- and zonal-grid solutions. The control surface is deflected down 6 deg and held stationary. Asymmetric pressure distributions indicate the effects of the deflected control surface. These effects can even be seen at the inboard sections. A comparison of unsteady pressures between the single- and zonal-grid results is also given in Fig. 9. The control surface oscillates with an amplitude of $\bar{\beta} = 1$ deg about a mean deflection of $\beta_m = 6$ deg. The unsteady pressure profiles show double peaks at the shock wave and the hinge line, although the shock wave is not seen in Fig. 8. In both figures, single- and zonal-grid computations agree well, in spite of the mismatched zoning. It takes about 9 sec on a CRAY-YMP single processor to set up the interpolation coefficients for all of the zonal interfaces. This corresponds to approximately 2 time steps of the Navier-Stokes calculation. After the coefficients are computed, the unsteady computations simply use the stored coefficients because the zonal interfaces remain stationary. This is one way to take an advantage of the flexibility of the zonal-grid technique along with the efficiency of the single-grid computation.

Conclusions

Unsteady Navier-Stokes computations have been performed for transonic flows over wings with oscillating control surfaces. To use the existing framework of the finite-difference method, the time metric terms are calculated by using the finite-volume concept. The use of locally moving grids has made it possible to efficiently simulate an oscillating control surface. The introduction of the stationary-mismatched zoning scheme has enhanced the flexibility of the code.

Comparisons of unsteady pressures with experimental data show reasonably good agreement, although the grids used in this study are relatively coarse. The computed results successfully predict main features of the unsteady pressure profiles, such as the double peaks at the shock wave and at the hinge line. In the future, an unsteady mismatched zoning scheme will be investigated. A control law will also be implemented into the code to compute aeroelastic performance of a wing.

Acknowledgements

The authors would like to thank Dr. G. H. Klopfer of MCAT Institute for his helpful suggestions and discussions on the mismatched zoning scheme. The first author's work was supported by NASA Grant NCC 2-605.

References

- ¹Ballhaus, W., Goorjian, P. M., and Yoshihara, H., "Unsteady Force and Moment Alleviation in Transonic Flow," AGARD Conference Proceeding No. 227, May 1981.
- ²Guruswamy, G. P. and Tu E. L., "Transonic Aeroelasticity of Fighter Wings with Active Control Surface," *Journal of Aircraft*, Vol. 26, No. 7, July 1989, pp. 682-684.
- ³Steger, J. L. and Bailey, H. E., "Calculation of Transonic Aileron Buzz," *AIAA Journal*, Vol. 18, March 1980, pp. 249-255.
- ⁴Horiuti, K., Chyu, W. J., and Buell, D. A., "Unsteady, Transonic Flow Computations for an Airfoil with an Oscillating Flap," *AIAA Paper 84-1562*, June 1984.
- ⁵Guruswamy, G. P., "Unsteady Aerodynamic and Aeroelastic Calculations of Wings Using Euler Equations," *AIAA Journal*, Vol. 28, No. 3, March 1990, pp. 461-469.
- ⁶Guruswamy, G. P., "Navier-Stokes Computations on Swept-Tapered Wings, Including Flexibility," *AIAA Paper 90-1152*, April 1990.
- ⁷Obayashi, S., Guruswamy, G. P., and Goorjian, P. M., "Streamwise Upwind Algorithm for Computing Unsteady Transonic Flows Past Oscillating Wings," *AIAA Journal*, Vol. 29, No. 10, Oct. 1991, pp. 1668-1677. Errata: *AIAA Journal*, Vol. 30, No. 2, Feb. 1992, pp. 569.
- ⁸Obayashi, S. and Guruswamy, G. P., "Unsteady Shock-Vortex Interaction on a Flexible Delta Wing," *AIAA Paper 91-1109-CP*, April 1991.
- ⁹Flores, J. and Chaderjian, N., "Zonal Navier-Stokes Methodology for Flow Simulation about a Complete Aircraft," *Journal of Aircraft*, Vol. 27, No. 7, July 1990, pp. 583-590.
- ¹⁰Baldwin, B. S. and Lomax, H., "Thin-Layer Approximation and Algebraic Model for Separated Turbulent Flows," *AIAA Paper 78-257*, Jan. 1978.
- ¹¹Degani, D. and Schiff, L. B., "Computations of Turbulent Supersonic Flows Around Pointed Bodies Having Crossflow Separation," *Journal of Computational Physics*, Vol. 66, No. 1, Sept. 1986, pp. 173-196.
- ¹²Vinokur, M., "An Analysis of Finite-Difference and Finite-Volume Formulations of Conservation Laws," *Journal of Computational Physics*, Vol. 81, No. 1, Mar. 1989, pp. 1-52.
- ¹³Obayashi, S., "Freestream Capturing for Moving Coordinates in Three Dimensions," *AIAA Journal*, Vol. 30, No. 4, April 1992, pp. 1125-1128.
- ¹⁴Obayashi, S., "Numerical Simulation of Underexpanded Plumes Using Upwind Algorithms," *AIAA Paper 88-4360-CP*, Aug. 1988.
- ¹⁵Obayashi, S., Goorjian, P. M., and Guruswamy, G. P., "Extension of a Streamwise Upwind Algorithm to a Moving Grid System," *NASA TM-102800*, April 1990.
- ¹⁶Obayashi, S., Matsushima, K., Fujii, K., and Kuwahara, K., "Improvements in Efficiency and Reliability for Navier-Stokes Computations Using the LU-ADI Factorization Algorithm," *AIAA Paper 86-0338*, Jan. 1986.
- ¹⁷Obayashi, S., Guruswamy, G. P. and Tu, E. L., "Unsteady Navier-Stokes Computations on a Wing-Body Configuration in Ramp Motions," *AIAA Paper 91-2865*, Aug. 1991.
- ¹⁸Klopfer, G. H. and Molvik, G. A., "Conservative Multizone Interface Algorithm for the 3-D Navier-Stokes Equations," *AIAA Paper 91-1601*, June 1991.
- ¹⁹Chaussee, D. and Klopfer, G., "The Numerical Study of Three-Dimensional Flow Past Control Surfaces," *AIAA Paper 92-4650*, Aug. 1992.
- ²⁰Persoon, A. J., Roos, R., and Schippers, P., "Transonic and Low Supersonic Wind Tunnel Tests on a Wing with Inboard Control Surface," *Air Force Flight Dynamics Lab., TR-80-3146*, Dec. 1980.
- ²¹Hess, R. W., Cazier, F. W., Jr., and Wynne, E. C., "Steady and Unsteady Transonic Pressure Measurements on a Clipped Delta Wing for Pitching and Control-Surface Oscillations," *NASA TP-2594*, Oct. 1986.

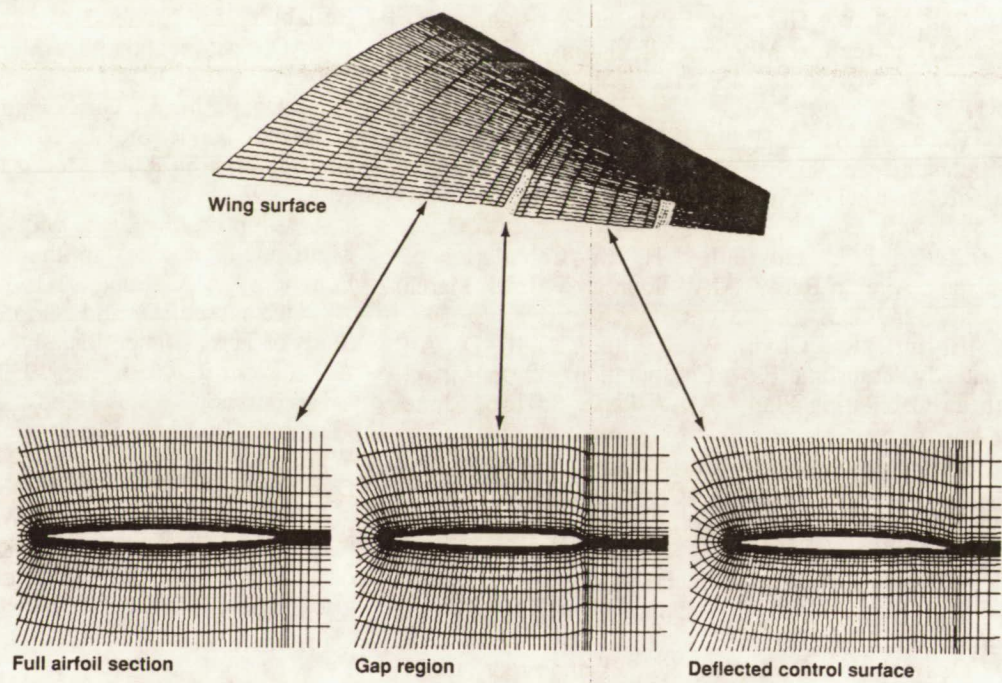


Fig. 1 A single grid for a wing with a control surface.

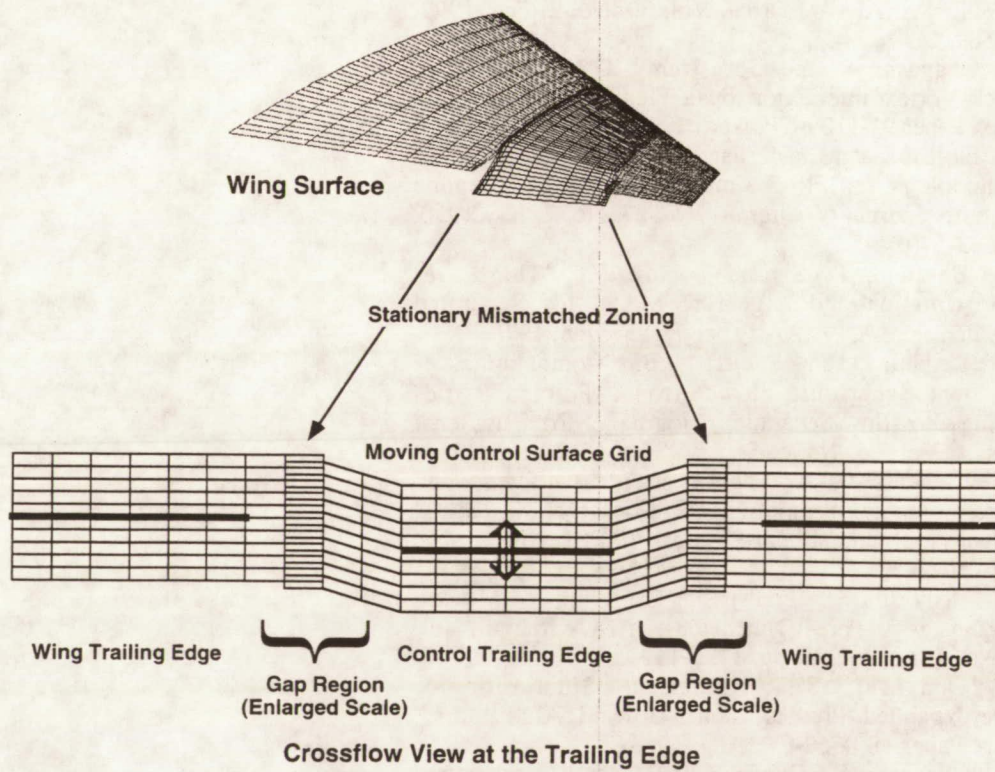


Fig. 2 Zonal grids for a wing with a control surface.

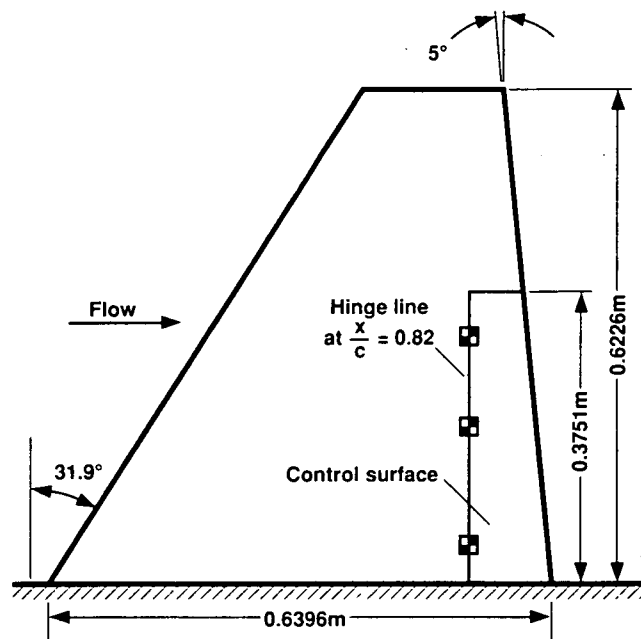


Fig. 3 Planform of F-5 wing with inboard trailing-edge flap.

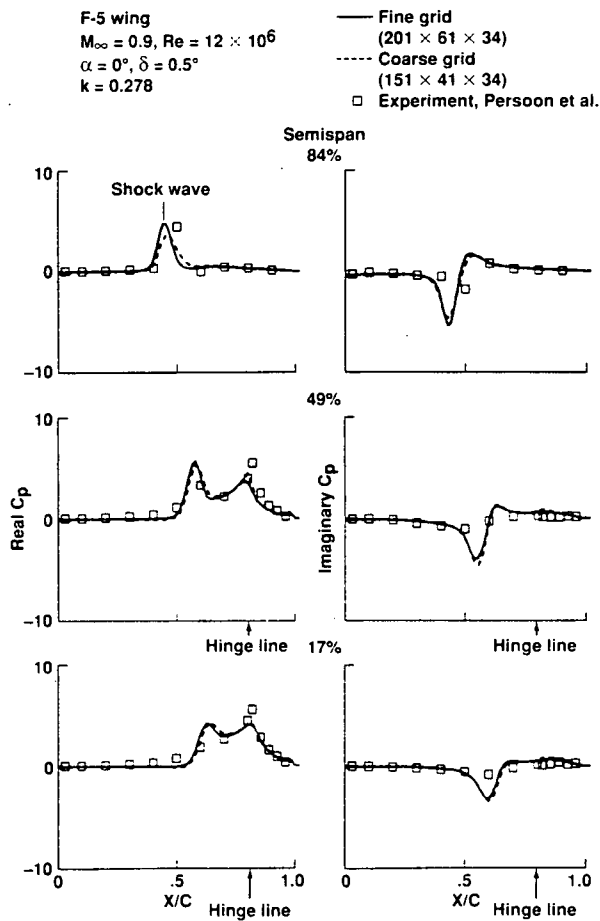


Fig. 4 Comparison of computed unsteady pressures between the coarse- and fine-grid solutions on the upper surface of the F-5 wing.

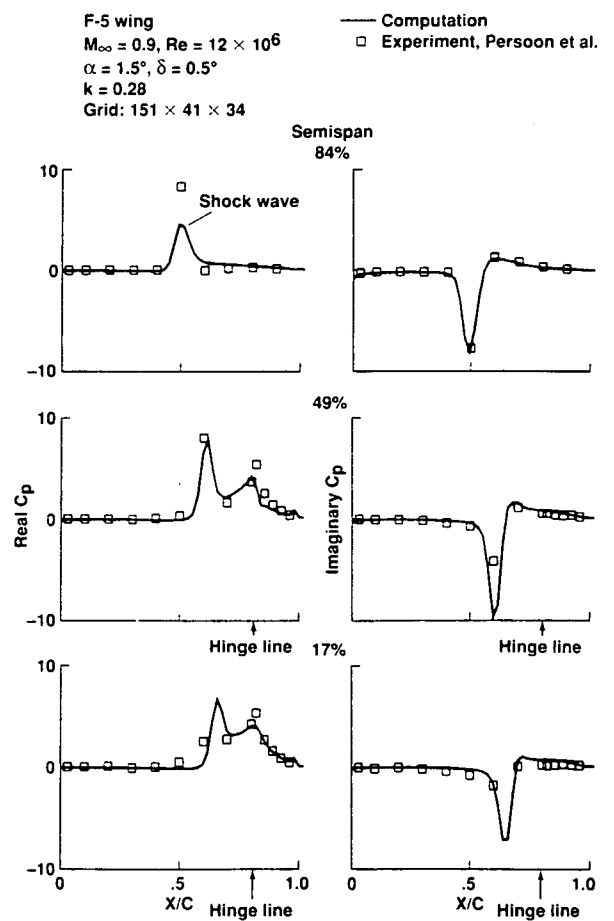


Fig. 5 Comparison of computed unsteady pressures with experimental data on the upper surface of the F-5 wing.

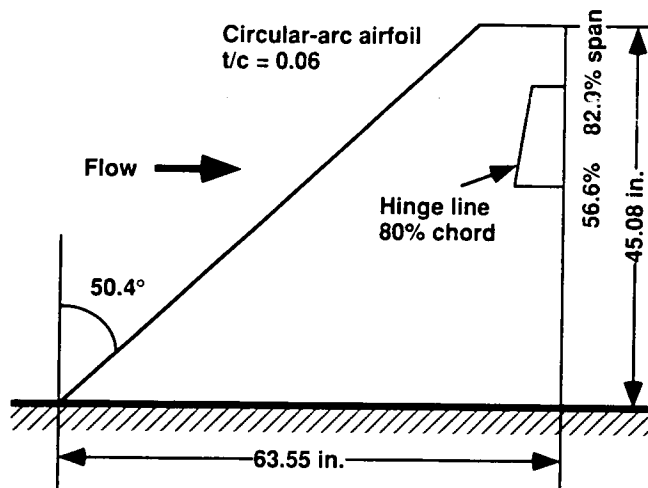


Fig. 6 Planform of clipped delta wing with trailing-edge flap.

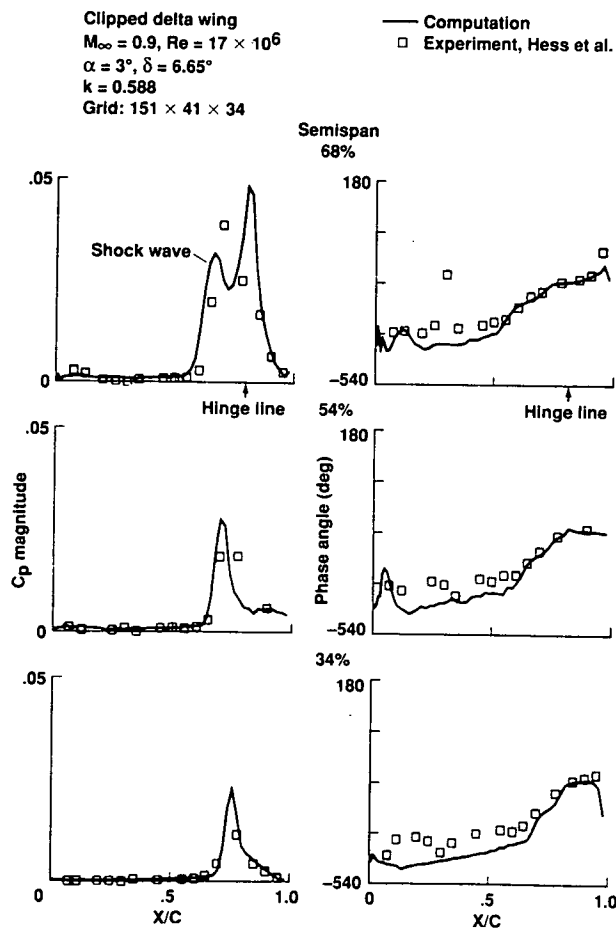


Fig. 7 Comparison of computed unsteady pressures between the use of freestream-capturing and finite-difference time metrics on the upper surface of the clipped delta wing.

Clipped delta wing
 $M_\infty = 0.9$, $Re = 17 \times 10^6$
 $\alpha = 0^\circ$, $\delta_{fix} = 6^\circ$

— Single-grid computation
 (151 × 44 × 34)
 - - - Zonal-grid computation
 (151 × 13 × 34,
 151 × 15 × 34,
 151 × 20 × 34)

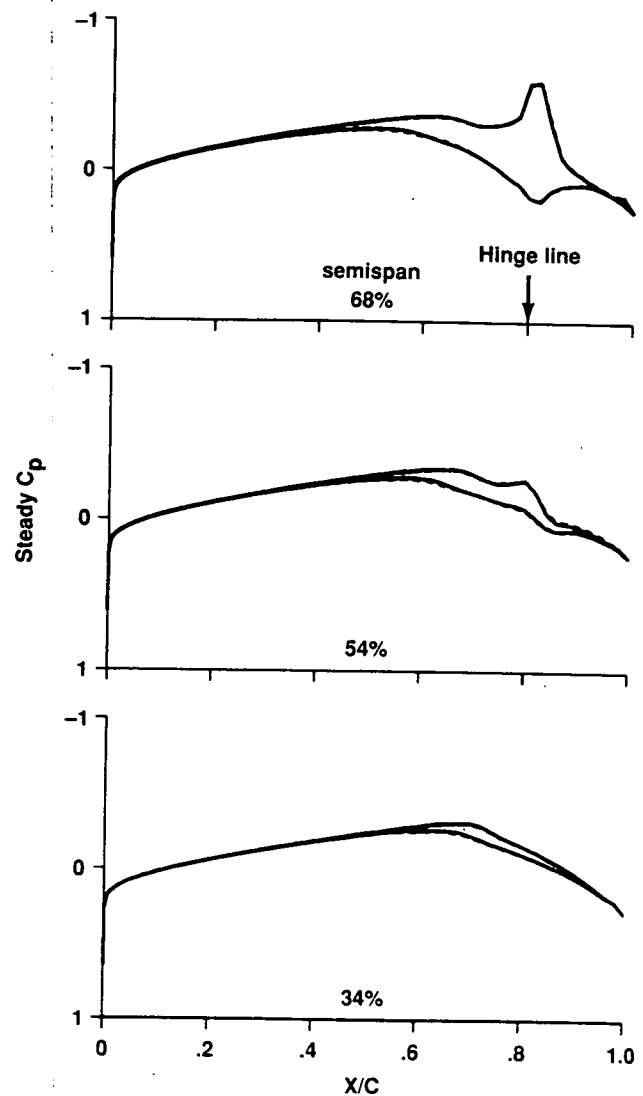


Fig. 8 Comparison of computed steady pressures between the single and zonal grids over the clipped delta wing.

APPENDIX D

Extended abstract of proposed paper for the AIAA 11th Computational Fluid Dynamics Conference, 6-9 July 1993, Orlando, Florida.

VIRTUAL ZONE NAVIER-STOKES COMPUTATIONS for OSCILLATING CONTROL SURFACES

G.H. Klopfer and S. Obayashi
Senior Research Scientists
MCAT Institute

NASA Ames Research Center, Moffett Field, CA 94035-1000

Abstract

A new unsteady zoning method called 'virtual zones' has been developed for application to an unsteady finite difference Navier-Stokes code. An existing interpolation method has been extensively modified to bring the run times for the interpolation procedure down to the same level as for the flow solver. Unsteady Navier-Stokes computations have been performed for transonic flow over a clipped delta wing with an oscillating control surface. The computed unsteady pressure and response characteristics of the control surface motion compare well with experimental data.

Introduction

Present civilian transport aircraft as well as highly maneuverable fighter aircraft are often subject to unsteady aerodynamics. In this unsteady environment aircraft designers utilize active controls to achieve controllability and safety of the aircraft. Active control can also be used to suppress transonic flutter characteristic of high aspect ratio transport wings and thus reduce the structural weight to achieve more efficient flight conditions.

In the transonic flow regime active controls have a pronounced effect on the aerodynamic and aeroelastic performance of a wing. This effect can be used to improve the airplane performance by the proper design of the active control surfaces. To do this successfully requires the accurate prediction of the aerodynamic and aeroelastic performance of a wing. Experimental prediction of unsteady aerodynamic and aeroelastic performance is costly and time consuming; numerical simulation of the unsteady Navier-Stokes equations is a much more cost effective alternative for predicting the performance of an active control surface.

The physics of unsteady transonic flow around a control surface has been simulated with small disturbance theory [1,2]. Unsteady Navier-Stokes simulations have been done in two dimensions [3,4]. A recent study [5] explored a three dimensional simulation of the unsteady thin-layer Navier-Stokes of the flow field surrounding a wing with an forced oscillating control

surface. In that study an unsteady Navier-Stokes code, ENSAERO, was extended to simulate unsteady flows over a rigid wing with an oscillating trailing-edge flap.

In the previous study an algebraic grid generation technique was incorporated into the code. The grid moved at every time step to follow the deflection of the flap. The small unsteady deflections were handled using a sheared single mesh. The large stationary deflection were handled using a zonal method [6]. The use of the single sheared grid did not permit the exact simulation of the unsteady flap-wing geometry. A gap had to be introduced between the ends of the flap and wing to allow sufficient space for the moving sheared mesh. The gap compromised the numerical simulation of the oscillating control surface flow field. The purpose of the present study is to rectify that compromise through the use of a new zoning technique called "virtual" zones.

The numerical simulation of the unsteady Navier-Stokes equations about complex and realistic aerodynamic configurations requires the use of zonal methods. In this method the overall flow field domain is subdivided into smaller blocks or zones. In each of these zones the flow field is solved independently of the other zones. The boundary data for each zone is provided by the neighboring zones. A major difficulty of the zonal methods applied to oscillating control surfaces has been how to account for the variable exposure of the ends of the control surfaces to the flow field.

The virtual zoning method, first implemented in a multizone finite volume code, CNSFV, [7], has been modified for application to the unsteady finite difference code, ENSAERO. For a finite difference application, virtual zones are essentially two-dimensional zones one cell thick. The main purpose of these zones is to convert, for example, a solid wall boundary condition into an interface condition. The interface conditions are required for the interzonal communication. In a multi-zonal code the virtual zones act like real zones as far as boundary and interface conditions are concerned, however, no flow field computations are done within these zones. Hence the name 'virtual' zone is appropriate.

In addition to the introduction of the virtual zones, it is necessary to speed up the process of determining the interpolation coefficients required for the interzonal communication if the unsteady Navier-Stokes simulation is to be practical.

The present study considers the transonic vortical flow over a clipped delta wing. A view of the wing and the control surface is shown in Fig. 1. Unsteady Navier-Stokes computations for the clean wing were reported in Ref. 8. The forced oscillating control surface computation with the single zone sheared mesh were presented in Ref. 5.

Numerical Method

Governing Equations and Discretization

The governing equations are the Reynolds-averaged thin-layer Navier-Stokes equations. The laminar viscosity is taken from the freestream laminar viscosity and is assumed to be constant for the transonic flow considered in this study. The turbulent viscosity is obtained with the Baldwin-Lomax algebraic eddy viscosity model [9] with the Degani-Schiff modification [10] to properly handle the leading edge separation as well as the control flap vortical flow.

The numerical algorithm, the time dependent metrics of the curvilinear coordinate system, and the performance characteristics of the ENSAERO code have been described previ-

ously and will not be repeated here. The interested reader is referred to Ref. 5.

Control Surface Grid and Zones

The primary focus of the present study is to demonstrate the feasibility of using dynamic zones for the oscillating control surface case and not so much as minimizing the cpu run times for the case to be presented. Hence the flow domain was split into only three real zones. Each of the zones consists of a C-H topology. The two zonal boundaries were placed at the span stations located at the ends of the control surface. Four additional zones (called virtual zones and described below) were placed in the two cuts separating the flap and the wing. One pair of the virtual zones remains fixed with the wing and the other pair is fixed with the flap and moves with the flap during the control surface motion. Figure 2 shows the seven zones involved.

The C grid around a deflected control surface can be obtained in two ways. One is to shear every grid line normal to the control surface with the local deflection. The other is to regenerate the entire C grid with the control surface deflected at every time step with an algebraic method. A previous study [5], showed that the computed surface pressures did not show any differences between the two methods. Therefore, for this study, the grids around the control flap were regenerated with the simpler shearing method.

Virtual Zone

The zoning capability of the CNSFV code [6], allowed the possibility of a single face of a zone to interact with several other zones. The procedure of determining the interpolation coefficients is automatic in that no additional information is required other than identifying the faces that are in contact with each other. To further extend the flexibility of the zoning method for the case of control surface aerodynamics, the idea of "virtual" zones was introduced in Ref. 7.

Virtual zones are zones of zero thickness (for a finite volume formulation) which serve to transfer solid wall (or other) boundary conditions to an interface condition. Thus multiple boundary conditions can be imposed on a block face with the same flexibility as an interface condition. Virtual zones also decouple the process of volume grid zoning from the surface grid patches which define the aerodynamic configuration under study. Surface grid patches are required in order to impose the proper boundary conditions. The volume grid zones should be set up to obtain the proper mesh qualities required for numerical accuracy. Another advantage of the decoupling is that much fewer zones are now needed, thus easing the effort and time required to generate the grids about complex and realistic configurations.

Finally the virtual zones also allow the zonal boundaries to cut through the configuration surfaces, which is an important property for control surfaces. The region of the configuration that intersects the zonal face is covered with a virtual zone to convert that region into another interface condition. Once a zone has been defined along with its associated virtual zones, its definition is complete and is not influenced by any of its neighboring zones. In other words the zone communicates with the outside world only through the interface conditions. Thus a particular zone can be altered or substituted with another zone without any need to redefine the interface conditions of the other zones. For example, a zonal grid can be set up for a wing with control flaps with one zone for each (say, undeflected) flap. For the deflected flap case, only the flap zone needs to be replaced with a zone containing a deflected flap. The

boundary and interface conditions of all other zones remain unchanged, even though they may now have a solid surface exposed to the flow field, e.g. the edge of the exposed end of the wing and flap.

The original zoning capability of the ENSAERO code was extended by including the above capability of multiple interface conditions on a single block face. Since the code is a finite difference code the zones required an overlap at the boundaries of the zones to allow for the proper interblock communication (ie. interfacing). In this study a one cell overlap was chosen. For this kind of zoning the virtual zones of zero thickness used for the finite volume formulation is not appropriate. Instead the thickness of the virtual zones had to be expanded to include the extent of the overlap of the zones. In other words the virtual zones for the present formulation are now one cell thick. There is a slight mismatch of a half cell thickness between the location of the actual solid wall and the location where the virtual zones apply the solid wall boundary condition. This mismatch does not occur with the finite volume formulation. However in the present case the slight mismatch had no discernable influence on the overall flow field, especially in the case where the ends of the flaps and wings are treated viscously, rather than with the inviscid tangency condition.

An example of the virtual zones required for the present case is shown in Figs. 3-5 for the inboard end of the control surface. The two virtual zones slide through each other with the control surface motion. As can be seen in the figures different amounts of the virtual zones are then exposed to, or in contact with, the real zones surrounding the wing and the flap. The virtual zones transfer the solid wall boundary condition to an interface condition and thus allows for the automatic inclusion of the variable exposure of the ends of the flap and wing to the flow field. The area where the wing and flap virtual zones overlap represents the unexposed portions of the flap and wing. Since the flow field is not updated in the virtual zones by the flow solver, nothing happens in the virtual zone overlap region nor does it influence the rest of the flow field.

Zonal Interface Interpolation

The original interpolation procedure used in CNSFV and ENSAERO was based on global area search. Even though it was vectorized, it was still much too slow for a dynamic interpolation procedure where the interpolation coefficients have to be updated at every time step. By replacing the area search with a procedure based on a polygon clipping algorithm, the search time to find the interpolants was reduced by two orders of magnitude. This improvement brought the cpu run times for determining the interpolation coefficients down to the same level as required for the flow solver (about 4 cpu seconds per iteration on the Cray YMP for the case discussed in the next section). More complete details will be presented in the full paper. There were some other techniques used that also helped speed up the process and these will also be discussed in the full paper.

Results

The test case considered in the present study is a clipped delta wing with an oscillating trailing edge control surface [11]. The wing planform is shown in Fig. 1. The wing has a leading edge sweep angle of 50.4 deg and a 6% thick circular arc airfoil section. At $M_\infty = 0.9$ and $\alpha = 3$ deg, both a leading edge vortex and a shock wave are present on the upper surface of the wing. The C-H grids of the three zones consist of $151 \times 13 \times 34$, $151 \times 15 \times 34$, and

151 × 20 × 34 points from the inboard to the outboard zones as shown in Fig. 2. Since the experiment was conducted using a Freon test medium, the ratio of specific heats, γ , is set to 1.135 in the present computations. As stated before, the modified Baldwin-Lomax model is used to account for the leading edge and control surface vortices. Steady state and rigid pitching calculations of this wing were reported in Ref. 8.

Figure 6 shows the unsteady pressures with the control surface oscillating at a frequency of 8 Hz and an amplitude of 6.65 deg at $M_\infty = 0.9$, $\alpha = 3$ deg and $Re_c = 17 \times 10^6$ based on the root chord. The results are shown as the amplitude and phase angle of the upper surface at the three span stations as indicated on the figure. In general the agreement with the experimental results is good. Because the accuracy of experiment had its own limitations, the virtual zone results are also compared with the single grid results of Ref. 5. As shown there is quite a discrepancy between the virtual zone results and the single grid results (the 151 × 44 × 34 grid), especially in the amplitudes at the center of the control surface. The discrepancy is however most likely due to the gap that was introduced between the flap and wing in the single grid case to accomodate the shearing grid. If the gap is reduced by increasing the spanwise resolution of the wing and control surface, the computational results of the refined single grid case (151 × 87 × 34) approach those of the virtual zone. This particular example demonstrates the importance of simulating the geometry of the control surface/wing configuration accurately.

The final figure shows the upper surface pressures as well as the instantaneous particle traces emanating from the leading edge of the wing (yellow traces), the lower edges of the wing at the control surface cut (blue traces), and the upper edges of the control flaps (red traces). The full paper will cover the flow physics near the wing/flap junctures in more detail.

Conclusions

An unsteady interface algorithm based on the idea of virtual zones has been developed for a finite difference code, ENSAERO. The new 'virtual' zoning technique simplifies zoning complex geometries such as control flaps and makes possible the use of standard multizonal codes for configurations difficult to do before. A fast search routine based on a window clipping algorithm has also been developed and is sufficiently fast so that new interpolation coefficients can be recomputed at every time step.

Both of the above developments have made practical a complete unsteady Navier-Stokes simulation of a forced oscillating control surface on a clipped delta wing in the transonic flow regime. The method has been validated against experimental data as well as numerical simulation based on a shearing single zone grid. The numerical result confirms that the accurate representation of geometry by 'virtual zones' is superior to the single zone computations at the same grid size.

Acknowledgements

The first author's work was supported by NASA Grant NCC 2-616 and the second author's by NCC 2-605.

References

1. Ballhaus, W., Goorjian, P. M., and Yoshihara, H.; "Unsteady Force and Moment Alleviation in Transonic Flow," AGARD Conference Proceeding No. 227, May 1981.

2. Guruswamy, G. P. and Tu, E. L.; "Transonic Aeroelasticity of Fighter Wings with Active Control Surface," *Journal of Aircraft*, Vol. 26, No. 7, July 1989, pp. 682-684.
3. Steger, J. L. and Bailey, H. E.; "Calculation of Transonic Aeleron Buzz," *AIAA Journal*, Vol. 18, March 1980, pp. 249-255.
4. Horiuti, K., Chyu, W. J., and Buell, D. A.; "Unsteady Transonic Flow Computation for an Airfoil with an Oscillating Flap," *AIAA Paper* 84-1562, June 1984.
5. Obayashi, S. and Guruswamy, G.; "Navier-Stokes Computations for Oscillating Control Surfaces," *AIAA Paper* No. 92-4431, August 1992.
6. Klopfer, G. H. and Molvik, G. A.; "Conservative Multizonal Interface Algorithm for the 3-D Navier-Stokes Equations," *AIAA Paper* No. 91-1601CP, June 1991.
7. Chaussee, D. S. and Klopfer, G. H.; "The Numerical Study of 3-D Flow Past Control Surfaces," *AIAA Paper* No. 92-4650, August 1992.
8. Obayashi, S. and Guruswamy, G.; "Unsteady Shock-Vortex Interaction on a Flexible Delta Wing," *Journal of Aircraft*, Vol. 29, No. 5, Sept-Oct 1992, pp. 790-798.
9. Baldwin, B. S. and Lomax, H.; "Thin-Layer Approximation and Algebraic Model for Separated Turbulent Flows," *AIAA Paper* 78-257, January 1978.
10. Degani, D. and Schiff, L. B.; "Computations of Turbulent Supersonic Flows Around Pointed Bodies Having Crossflow Separation," *Journal of Computational Physics*, Vol. 66, No. 1, September 1986, pp. 173-196.
11. Hess, R. W., Cazier, F. W., Jr., and Wynne, E. C.; "Steady and Unsteady Transonic Pressure Measurements on a Clipped Delta Wing for Pitching and Control-Surface Oscillations," *NASA TP-2594*, Oct. 1986.

List of Figure Captions

Fig. 1. Planform of clipped delta wing with trailing edge flap.

Fig. 2. Surface grids and zonal boundaries of wing/flap configuration.

Fig. 3. Perspective view of trailing edge flap and wing.

Fig. 4. Perspective view of trailing edge flap and wing with the inboard wing and flap virtual zones.

Fig. 5. Perspective phantom view of trailing edge flap and wing with the inboard wing and flap virtual zones.

Fig. 6. Comparison of unsteady pressures between virtual zones and single grids computations with the experimental data of Ref. 11.

Fig. 7. Upper surface pressures and instantaneous particle traces emanating from the leading edge and the edges of the control surface.

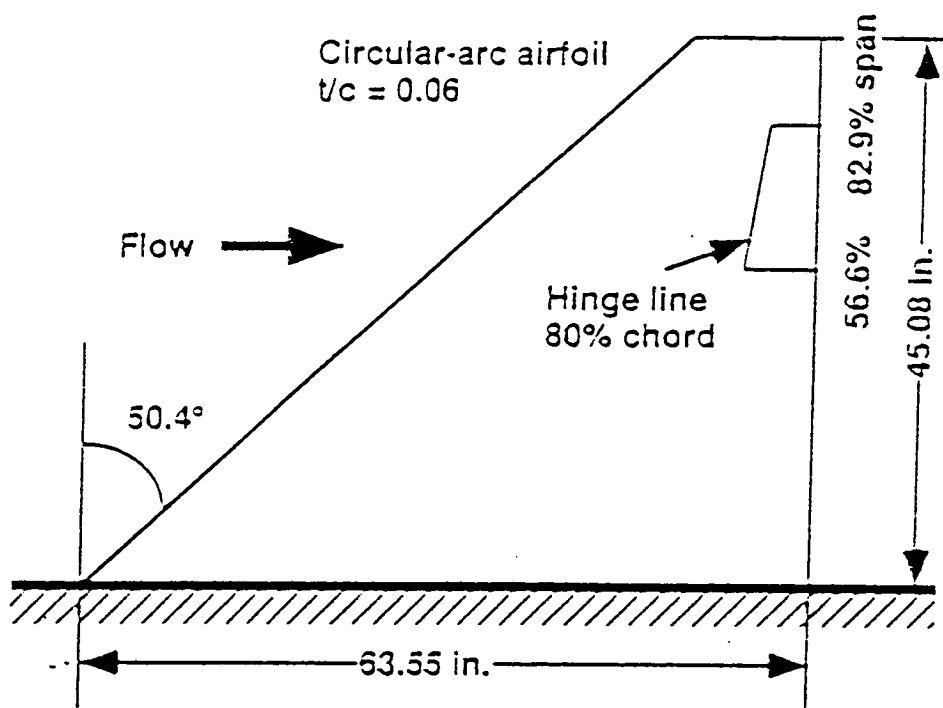


Fig. 1

Flow

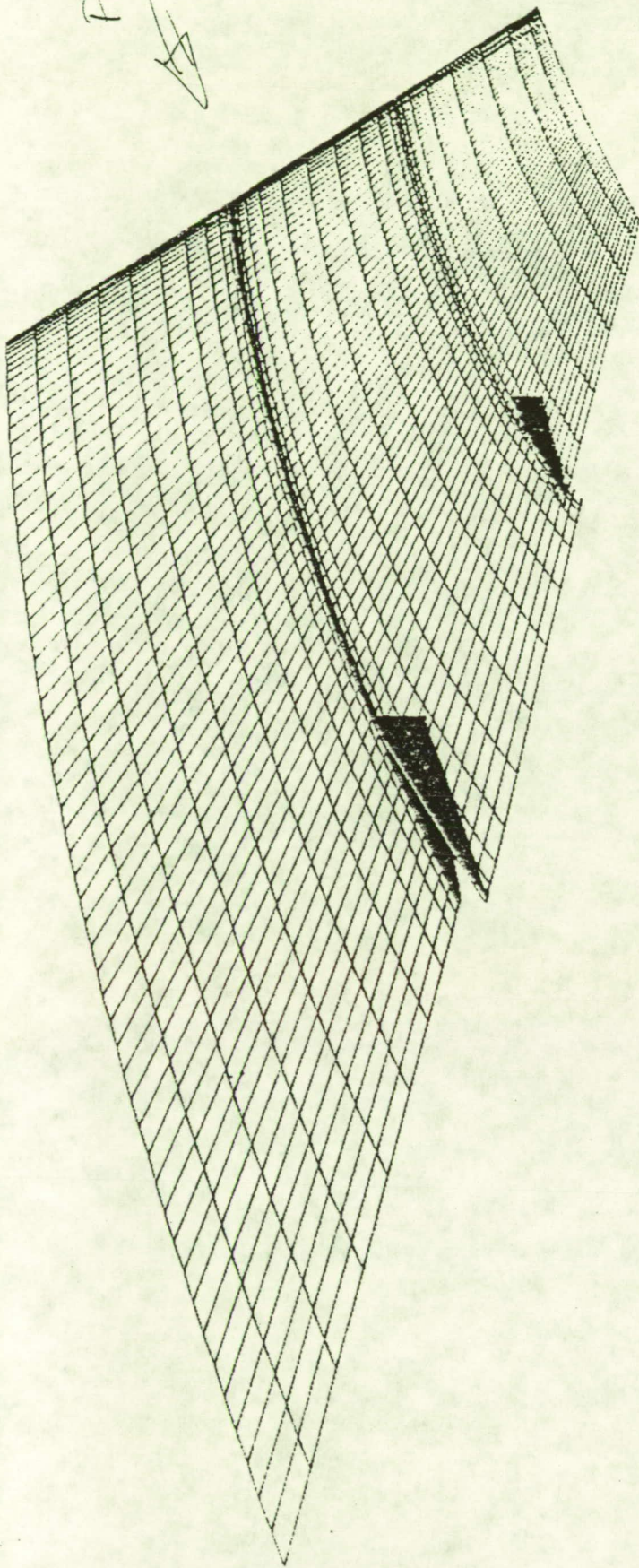
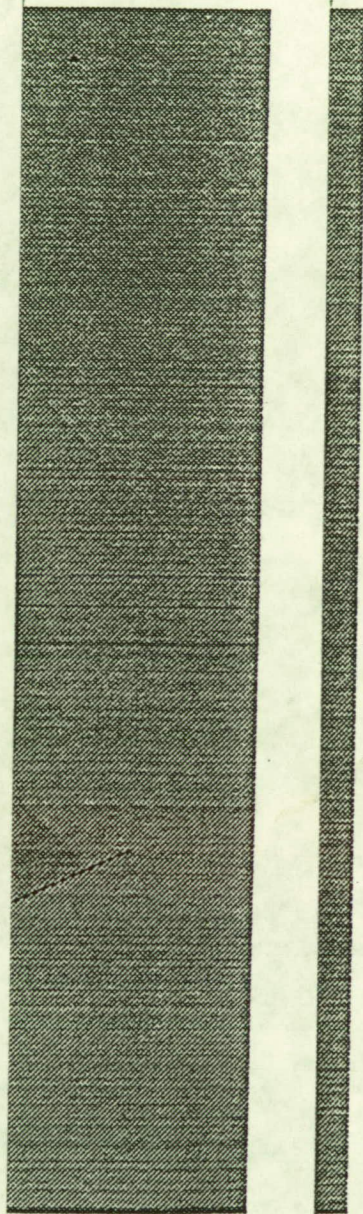


Fig. 2



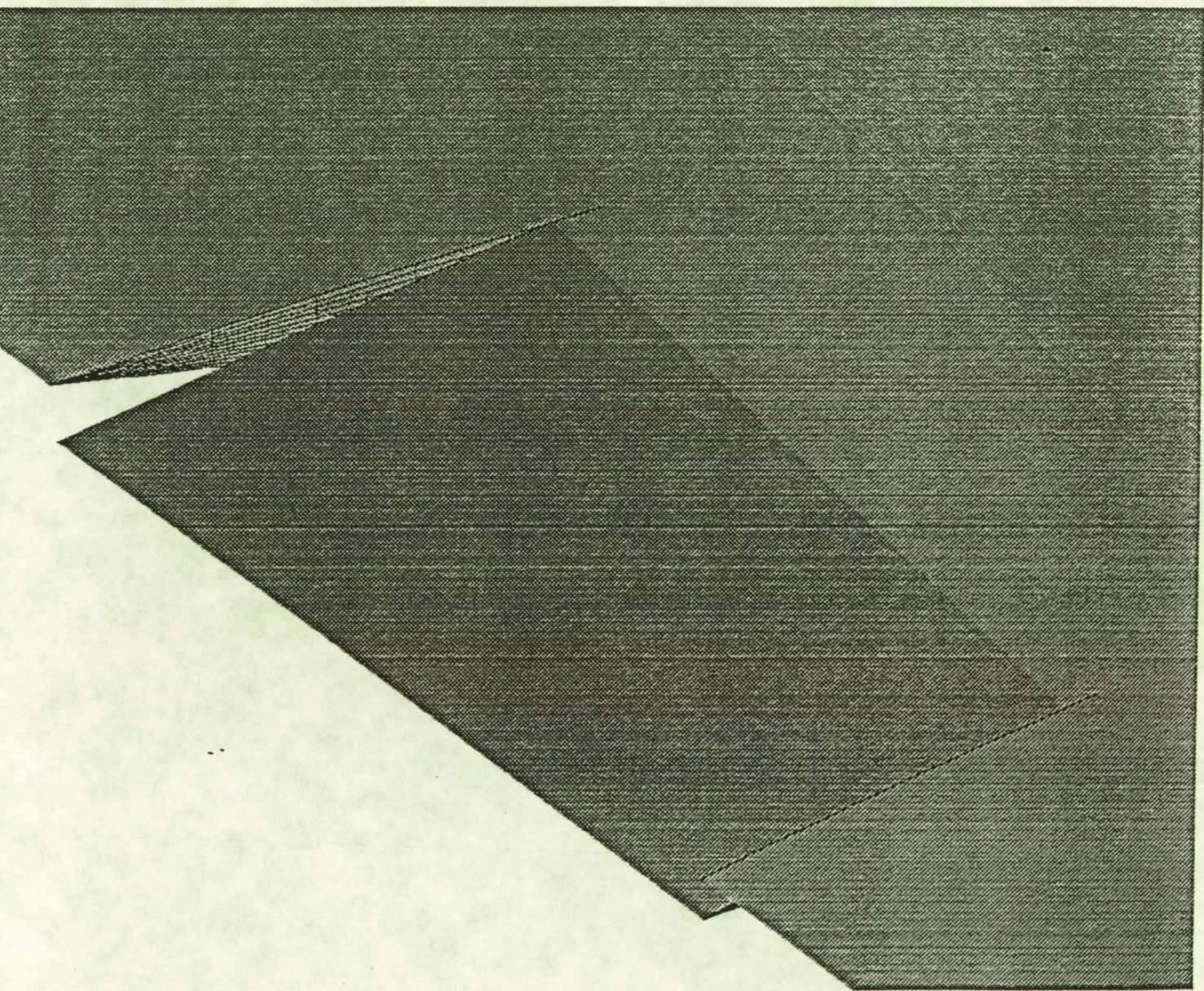


Fig. 3

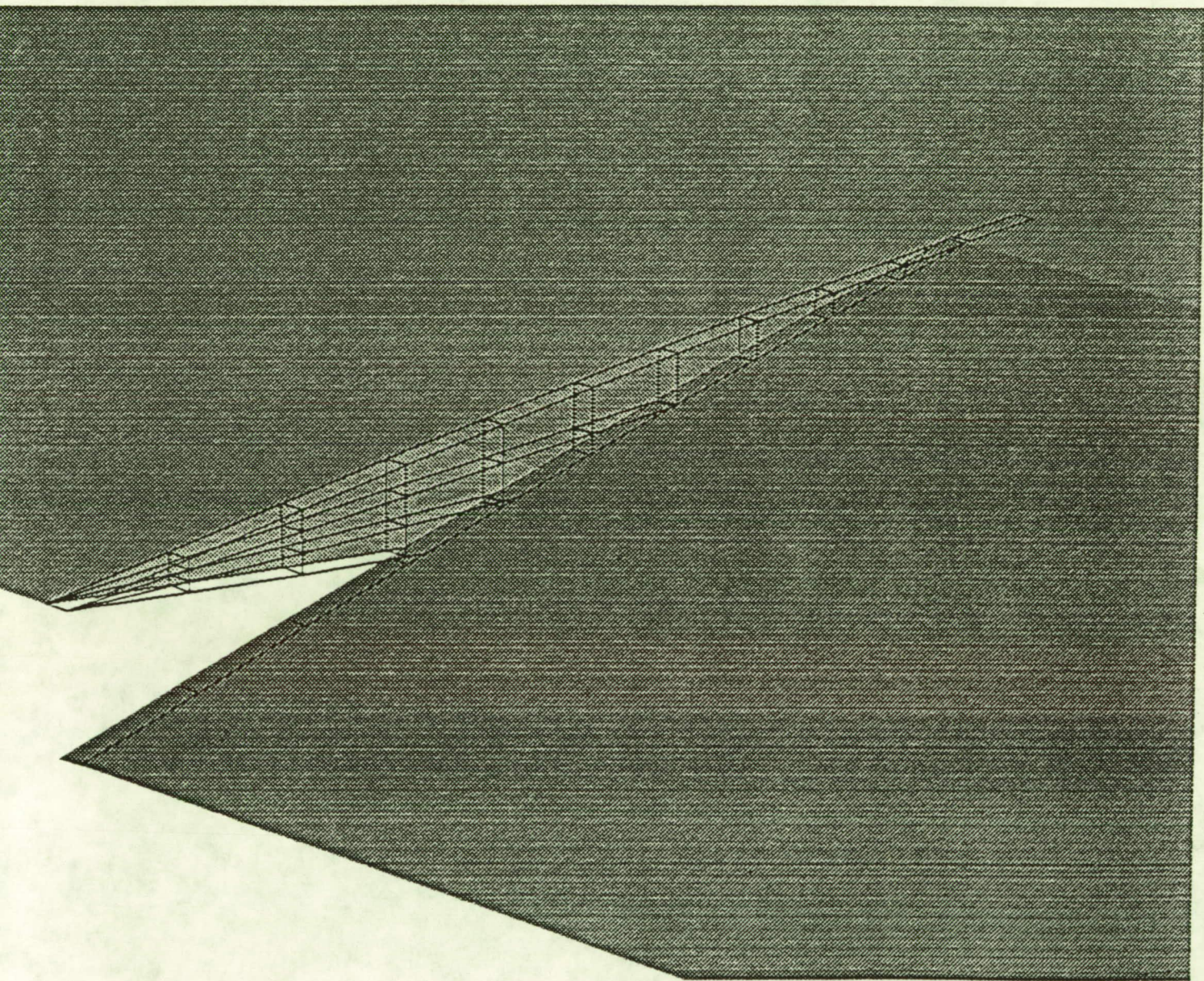


Fig. 4

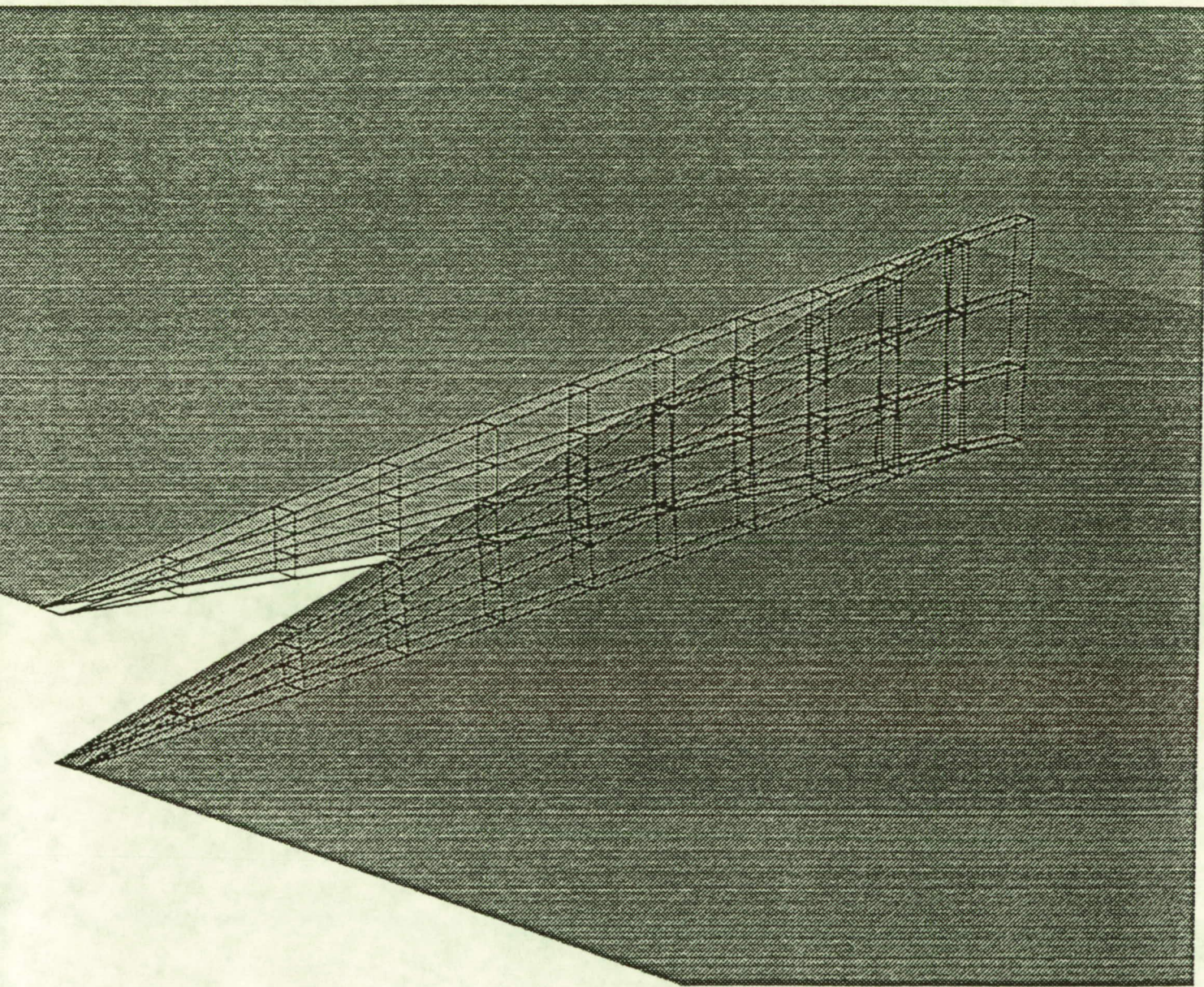


Fig 5

- 151x44x34 Virtual Zones
--- 151x87x34 Single grid
.... 151x44x34 Single grid
□ EXP'L HESS et al

Semispan

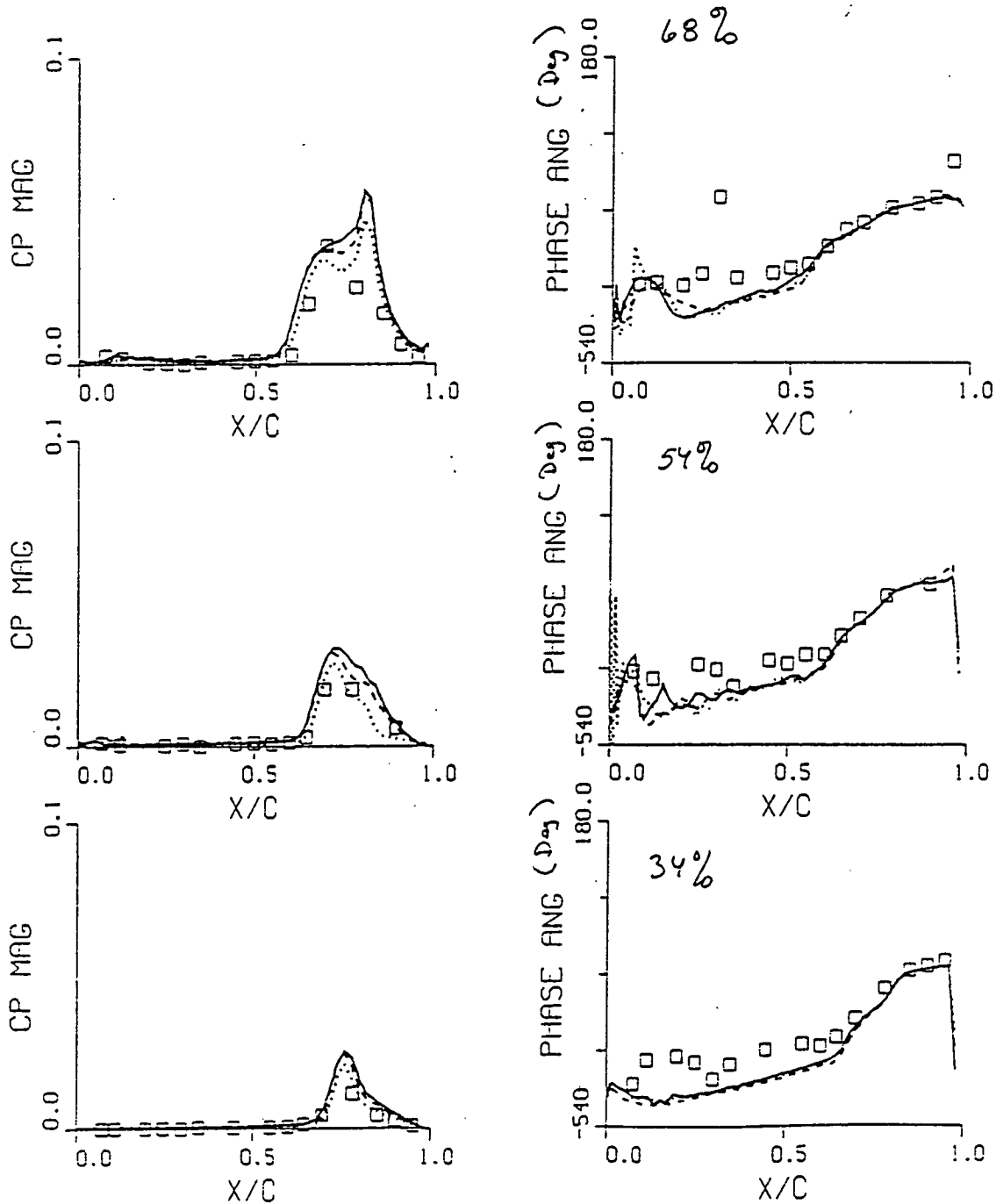


Fig. 6

Flow

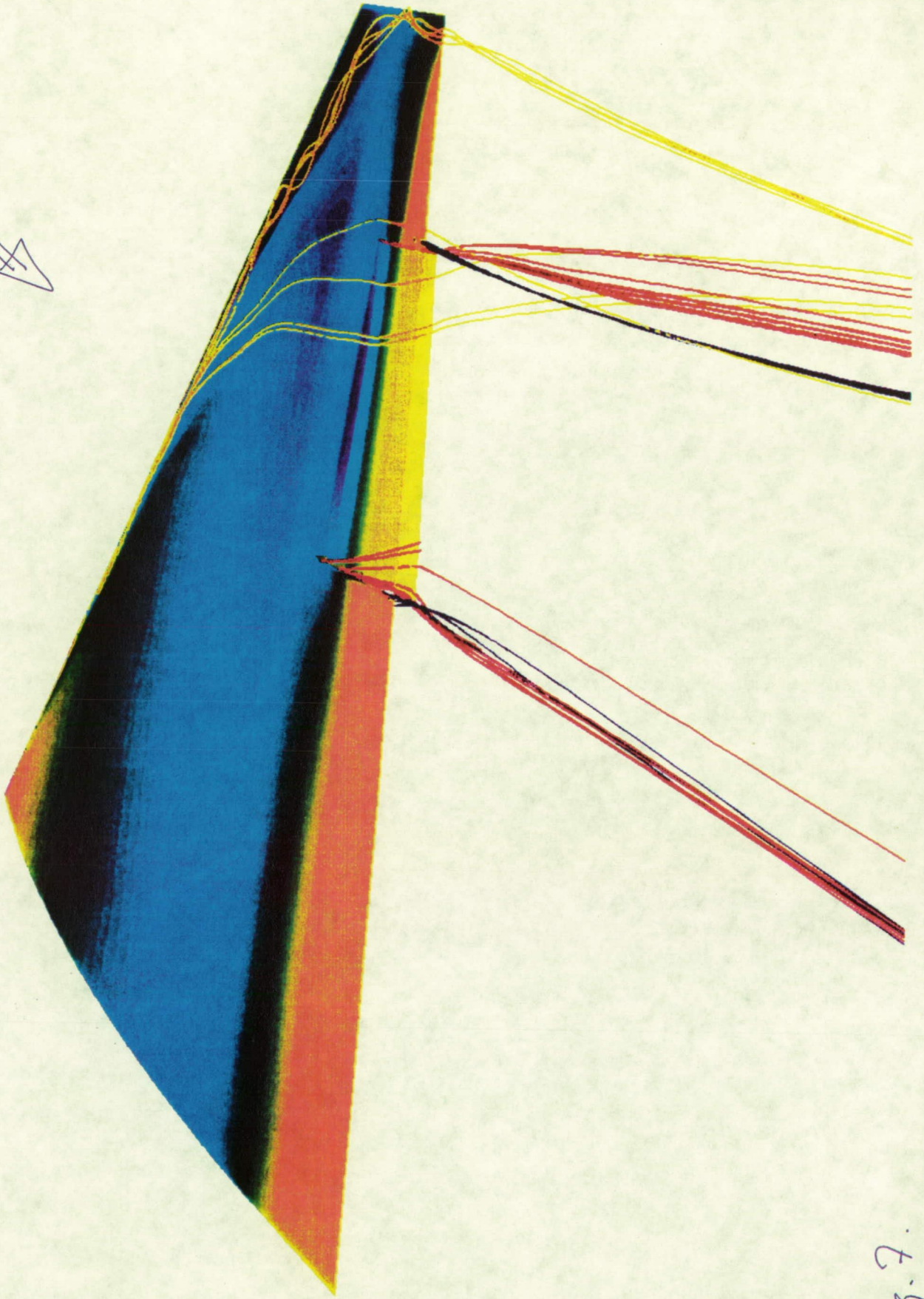


Fig. 7.

APPENDIX E

Extended Abstract of a proposed paper for presentation at the
24th AIAA Fluid Dynamics Conference, July 6-9, 1993, Orlando, FL

Unsteady Navier-Stokes Simulation of the Canard-Wing-Body Ramp Motion

Eugene L. Tu,* Shigeru Obayashi† and Guru P. Guruswamy‡
NASA Ames Research Center, Moffett Field, California 94035-1000

Introduction

The use of canards in many advanced aircraft for control and improved aerodynamic performance has been the topic of continued research. In addition to providing rapid pitch control, the influence of canards on wing aerodynamics can often result in increased maximum lift and decreased trim drag. There are also unique dynamic performance characteristics for canard-configured aircraft coupled with the capability of present-day automatic control systems. The reduced or even negative static stability of canard configurations can lead to improved aircraft agility and maneuverability.

Several examples of the use of canards for stability and control are currently available. The X-31 aircraft uses a long-coupled canard for pitch control¹ while the SAAB JAS 39 Gripen uses a short- (or close-) coupled canard in maneuvering, cruise and even landing roll-out conditions.² The close-coupled canard of the X-29 forward-swept aircraft is integrated into the active control system and is used to maintain control of this inherently unstable aircraft.³

In the three examples given above and, indeed, in most canard-configured aircraft, the main benefits of canards are realized during maneuver or other dynamic conditions. Therefore, the detailed study of canards as primary control surfaces requires the accurate prediction of the unsteady aerodynamics of such configurations. For close-coupled canards,

* Research Scientist, Member AIAA

† Senior Research Scientist, MCAT Institute, Senior Member AIAA

‡ Research Scientist, AIAA Associate Fellow

the unsteady aerodynamic performance associated with the canard-wing interaction is of particular interest.

At moderate angles of attack, canards or wings with sharp leading edges exhibit flow separation at the leading edge due to the adverse pressure gradient on the leeward side. In general, the flow structure of highly-swept or delta canard-wing configurations is characterized by a canard downwash, which modifies the wing flowfield, and an interaction between the canard and wing vortex systems. The inboard wing flowfield is often dominated by the canard downwash and the outboard is affected by the subsequent change in wing leading-edge vortex formation and the canard-wing vortex interaction. Further details of the flow features of steady canard-wing-body aerodynamics are given in Ref. 4.

In general, the characteristics of static canard configurations are adequately represented by steady-state aerodynamics. At higher angles of attack, some of the conditions which may result in unsteady aerodynamics include large regions of separated flow and vortex breakdown. However, for a configuration undergoing unsteady motion, the dynamic effects can be quite significant. In particular, the downwash of the canard and the interaction between the canard and wing vortices can exhibit highly non-linear unsteady aerodynamic characteristics.

The use of canards for improved cruise performance has been supported by both experimental (e.g. Refs. 5-9) and computational studies (e.g. Refs. 10-12) which investigated the steady-state aerodynamics of typical canard configurations. Many of these studies investigated the effects of canard size, position and deflection angle on the canard-wing aerodynamic interaction. A study by Boyden¹³ investigated the dynamic stability and response characteristics of typical canard configurations and showed potential benefits in maneuverability and agility with the use of canards.

Computational fluid dynamics (CFD) has become a valuable tool for understanding the complex three-dimensional flow physics of canard configurations. A number of studies based on conformal mapping, linear and nonlinear vortex lattice methods, the transonic

small perturbation (TSP) equation, and Euler equations have been performed for steady canard-wing aerodynamics and are listed in Ref. 4. However, very limited computational work has been performed to study the details of the unsteady canard-wing-body flowfield using the Navier-Stokes equations, which are required to accurately model viscous effects.

Previous studies^{4,14,15} by the first author have successfully solved the Navier-Stokes equations to investigate steady-state canard-wing-body aerodynamics, including effects of canard deflection and vertical position. Accuracy was demonstrated by favorable comparisons with experimental surface pressure, force and moment data. A grid refinement study was also performed to resolve any significant discrepancies in the baseline computational comparisons with experiment.

A more recent Navier-Stokes simulation¹⁶ has been performed to investigate the unsteady aerodynamics of a wing-body (no canard) configuration undergoing ramp motions. Reference 16 demonstrated significant dynamic effects on wing-body aerodynamic loads. In the present study, the thin-layer Navier-Stokes equations are solved for the unsteady flow about a highly-swept canard-wing-body configuration undergoing ramp (pitch-up) motions. Emphasis is placed on understanding the complex unsteady flowfield at various pitch rates and flow conditions. In addition to surface pressures, forces and moments, a detailed analysis of the unsteady canard-wing vortex structure, including vortex breakdown, is performed. Both grid and time-step refinement studies are conducted to verify adequate spatial and time accuracy of the current method.

Computational Modeling

Numerical Procedure

The NASA Ames ENSAERO code is used to solve the unsteady thin-layer Navier-Stokes equations. ENSAERO has the capability to simultaneously integrate the Navier-Stokes equations coupled with the modal structural equations of motion and has been recently

demonstrated for steady, unsteady and aeroelastic applications.^{16–19} Since the current study is restricted to rigid-body motions, the modal structural equations are not being solved.

The current version of ENSAERO includes both a central-difference scheme,²⁰ which is identical to that used in the Transonic Navier-Stokes (TNS) code,^{4,21} and a streamwise upwind numerical scheme.¹⁸ Both schemes have been found to be accurate for the current geometry and flow conditions. In order to compare current results directly with earlier canard-wing-body steady-state computations,⁴ the central-difference scheme is utilized for this study. It is noted that the central-difference scheme in ENSAERO is first-order accurate in time and second-order accurate in space.

To provide turbulence closure, the Baldwin-Lomax algebraic eddy-viscosity model²² is used. Due to the vortex-dominated flow structures of the highly-swept sharp-leading-edge canard and wing, a modification to the original Baldwin-Lomax formulation is required. For this study, the Degani-Schiff modification,²³ as originally developed for crossflow-type separations, is employed. It is noted that with present-day CFD technology, higher-order eddy-viscosity models could easily be utilized and are readily available within the ENSAERO code. However, with the lack of significant non-equilibrium or streamwise separation effects anticipated at the moderate angles of attack being investigated, the benefits for the current study of such higher-order models do not justify the increased computational costs. Further details about the ENSAERO code, algorithm, zonal approach, and general performance will be given in the full paper.

Geometry Modeling and Grid Generation

The geometry in this study is based on the wind-tunnel model used by Gloss and Washburn⁵ and is illustrated in Fig. 1. The same geometry was used in the previous steady-state numerical study⁴ and in the unsteady wing-body (canard-off) study.¹⁶ In the original wind-tunnel model, fairings were used to facilitate a vertical-offset canard. These fairings, which account for slight asymmetries in the experimental results, are omitted in the current

computational modeling. The sting used for wind-tunnel mounting is modeled by extending the body, with its appropriate no-slip boundary condition, to the downstream boundary.

Using the S3D surface geometry and grid generation code,²⁴ the canard, wing and body component surface geometries are modeled from their original analytical definitions. The 3DGRAPE²⁵ program is then used to generate the single-zone canard-wing-body flowfield grid. The overall H-O topology grid, with the mismatched interface, for a typical high-canard case is given in Fig. 2. An expanded view of the flowfield grid near the geometry is also shown.

The resulting grid for the canard-wing-body configuration contains 4,625 points (half-body) on the surface, and approximately 470,000 points in the flowfield. This same grid was used extensively in previous steady-state computations⁴ and was found to provide accurate results at moderate angles-of-attack. A grid refinement study which increases the total number of flowfield points to almost 2 million will also be presented in the full paper.

Since the current computations are performed in the transonic regime, the flowfield grid is extended upstream and downstream by approximately eight wing root-chord lengths, and in the radial direction by six wing-span lengths.

Results and Discussion

Preliminary results are presented to validate the current methodology and provide initial analyses of the unsteady canard-wing-body flowfield. All steady and unsteady results are computed at $M_\infty = 0.90$ and Reynolds number based on the mean aerodynamic chord of the wing (Re_c) of 1.52 million. Comparisons between computed results and experimental data^{5,26} are made to validate the accurate prediction of the steady flowfield. Convergence of the unsteady flowfield is verified using time-step refinement. Previous studies^{16,17,27} have demonstrated accurate unsteady flowfield predictions using ENSAERO on various wing, wing-body and wing with control surface geometries.

Experimental Comparisons

Figure 3 shows the effect of the canard on the wing flowfield at $\alpha \approx 4^\circ$. The stations inboard of the canard-tip span line (25% and 45% span) are most significantly influenced by the presence of the canard. For the canard-off case, the suction peak on the upper surface identifying the presence of a leading-edge vortex is clearly evident. At this static angle of attack, the canard-on results show that the formation of the wing leading-edge vortex is inhibited at the inner stations. This effect of the canard on the leading-edge vortex is directly attributed to the canard downwash. The results presented in Ref. 4 indicate that discrepancies between the computational and experimental results in Fig. 3 are resolved with grid refinement.

Effect of Canard on Unsteady Aerodynamic Loads

The effect of the canard on the unsteady aerodynamic loads associated with pitch-up ramp motion are presented in this section. All unsteady canard-wing-body results are computed for α from 0° to 15° and various non-dimensional pitch rates as defined by $A = \dot{\alpha} \bar{c} / U_\infty$. Ramp motions are started from converged steady-state solutions at an initial angle of attack (α_i) and held at the final angle (α_f) for a specified length of time. The pitch axis of the ramp motion and the pitching moment results are taken from the model c.g. location shown in Fig. 1.

A typical ramp motion from $\alpha_i = 0^\circ$ to $\alpha_f = 15^\circ$ is illustrated in Fig. 4. In order to directly compare unsteady and steady-state results, time (t) is given in degrees. Therefore, during the ramp motion ($0^\circ \leq t \leq 15^\circ$) α and t are equal ($\alpha = t$). However, for $t > 15^\circ$, α is held constant at 15° ($\alpha = 15^\circ$ or α_f). In this manner, the ramp motion has an impulsive start and finish which significantly influence the unsteady results.

Computed time histories of lift, drag and pitching moments for the configuration, with and without canard, undergoing a ramp motion (pitch rate, $A = 0.10$) are illustrated in Fig. 5.

Computational and experimental steady-state results are also given at the corresponding instantaneous angles of attack.

The lift curves of Fig. 5 show a significant dynamic lift increase for the unsteady canard-on case. Early in the motion ($t < 4^\circ$), the unsteady canard-on lift is slightly lower than the canard-off lift due to the effects of the virtual (or apparent) mass of the fluid. Since the entire canard is forward of the pitch axis, there is an initial loss of lift on the canard at the start of the ramp motion ($t = 0^\circ$). As the ramp motion continues, the canard-on case exhibits increased dynamic lift over both the canard-off and steady-state canard-on cases.

As expected, the time histories of drag coefficients follow a similar trend. However, by replotting the drag results of Fig. 5 in traditional drag polar form, Fig. 6 shows that the unsteady canard-on case exhibits improved dynamic lift-to-drag performance.

The pitching moments given in Fig. 5 also illustrate the significant influence of the fluid virtual mass at the start ($t = 0^\circ$) and finish ($t = 15^\circ$) of the ramp motion. The virtual mass acts to counter the acceleration of the body and, therefore, causes a rapid nose-down pitching moment at $t = 0^\circ$ and a nose-up moment at $t = 15^\circ$. Beyond $t = 15^\circ$, the lift, drag and pitching moment values converge toward the steady-state $\alpha = 15^\circ$ result.

The effect of pitch rate on dynamic lift for the canard-on case is given in Fig. 7 for $A = 0.10$ and 0.05 . Note that since comparisons are made at instantaneous angles of attack during the ramp motion (t in deg.), the physical time (t in sec.) between the two pitch rates differ by a factor of two. Figure 7 shows that the dynamic lift of the canard configuration is increased at the higher pitch rate throughout the ramp motion. Far enough into the ramp motion ($t > 10^\circ$), there appears to be an approximately linear relation between pitch rate and dynamic lift for the current configuration. This observation will be explored further in the full paper with a more extensive parameter study.

Analysis of Unsteady Aerodynamic Loads

Better insight into the dynamic loads produced by the ramp motion (Fig. 5) can be

attained by examining the separate component regions of the geometry. The canard region consists of the canard and the body forward of the wing leading-edge root location (fore-body). The wing region consists of the wing and the remaining aft-body (not including the sting).

The time history of the canard and wing region lift contributions for the $A = 0.05$ ramp motion are illustrated in Fig. 8. Computed steady-state lift coefficients are also given for reference. By definition, the total configuration lift is the sum of the canard and wing region lift. The effects of the fluid virtual mass is evident at both $\alpha_i = 0^\circ$ and $\alpha_f = 15^\circ$. Due to the relative locations of the canard and wing to the pitch axis, there is an initial increase in wing region lift and a decrease in canard region lift at α_i . These trends are then reversed at α_f .

Figure 8 shows that there is a net loss of dynamic lift for the canard throughout the ramp motion. The increased dynamic lift for the total configuration is due to the large increase in dynamic lift of the wing. In linear stability theory, the lift of the wing or canard can be written as

$$C_L = C_{L_\alpha} \alpha + C_{L_{\dot{\alpha}}} \dot{\alpha} + C_{L_q} q \quad (1)$$

where C_{L_α} , $C_{L_{\dot{\alpha}}}$ and C_{L_q} are the stability derivatives $(\partial C_L / \partial \alpha)_0$, $(\partial C_L / \partial \dot{\alpha})_0$ and $(\partial C_L / \partial q)_0$, respectively; q is the angular velocity of the configuration about the pitch axis. The notation $()_0$ indicates that partial derivatives are evaluated assuming no disturbance from the other terms. Note that for the ramp motion, $q = \dot{\alpha}$.

The loss of canard lift is primarily due to the location of the canard forward of the pitch axis which, if described by linear stability theory, causes a negative contribution to $C_{L_{canard}}$ from the $C_{L_q} q$ term in Eq. 1. After the ramp motion stops ($t > 15^\circ$), the lift contribution from the wing converges to the steady-state result much more slowly than the canard region lift. Previous studies¹⁶ indicate that vortex interaction and breakdown may be a significant factor in this phenomenon.

In order to confirm the convergence of the unsteady computations, Fig. 9 shows the effect of time-step size (Δt in deg.) on the unsteady lift curves for the component regions of the geometry. From Fig. 9, it is clear that with decreasing time-step size, the time-accurate solutions converge quickly. In fact, even when using a larger step size, the lift curves compare favorably for $t > 0.1^\circ$. In all previous computations presented in this study, $\Delta t = 0.0025^\circ$ was used.

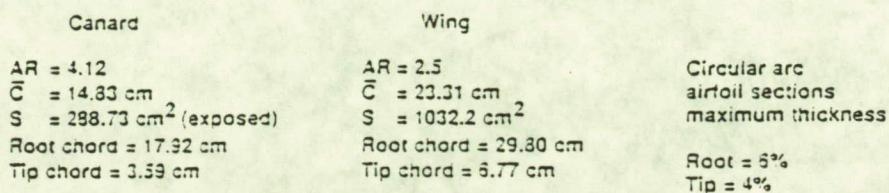
A complete analysis of the unsteady canard-wing-body flowfield for the configuration undergoing ramp motions will be presented in the full paper. This analysis will include a detailed study of the canard-wing vortex interaction and the dynamic effects associated with vortex breakdown. For example, a side-by-side comparison of upper surface pressures (Fig. 10) shows a dramatic increase in canard and wing vortex strengths for the unsteady case. In Fig. 10, the unsteady result is for $A = 0.10$ and gives an instantaneous map of surface pressures at $\alpha = 8.55^\circ$ during a pitch-up ramp motion from 0° to 15° . Numerical issues including the effects of dissipation, turbulence modeling and grid fineness will also be addressed in the full paper.

References

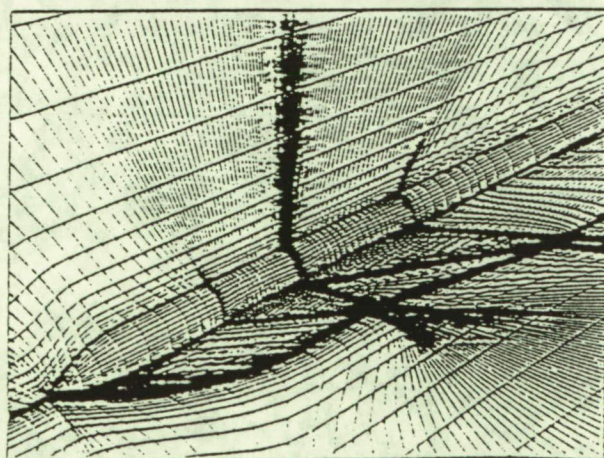
- ¹ Yeh, D.T., George, M.W., Clever, W.C., Tam, C.K. and Woan, C.J., "Numerical Study of the X-31 High Angle-of-Attack Flow Characteristics," AIAA Paper 91-1630, June 1991.
- ² Modin, K.E. and Clareus, U., "Aerodynamic Design Evolution of the SAAB JAS 39 Gripen Aircraft," AIAA Paper 91-3195, September 1991.
- ³ Kehoe, M.W., Bjarke, L.J. and Laurie, E.J., "An In-Flight Interaction of the X-29A Canard and Flight Control System," NASA TM 101718, April 1990.
- ⁴ Tu, E.L., "Navier-Stokes Simulation of a Close-Coupled Canard-Wing-Body Configuration," *Journal of Aircraft*, Vol. 29, No. 5, September-October 1992, pp. 830-838.
- ⁵ Gloss, B.B. and Washburn, K.E., "Load Distribution on a Close-Coupled Wing Canard

- at Transonic Speeds," *Journal of Aircraft*, Vol. 15, No. 4, April 1978, pp. 234-239.
- ⁶ Er-El, J. and Seginer, A., "Vortex Trajectories and Breakdown on Wing-Canard Configurations," *Journal of Aircraft*, Vol. 22, No. 8, August 1985, pp. 641-648.
- ⁷ Calarese, W., "Vortex Interaction on a Canard-Wing Configuration," Air Force Wright Aeronautical Laboratories AFWAL-TR-86-3100, October 1986.
- ⁸ Oelker, H. and Hummel, D., "Investigations on the Vorticity Sheets of a Close-Coupled Delta-Canard Configuration," *Journal of Aircraft*, Vol. 26, No. 7, July 1989, pp. 657-666.
- ⁹ Erickson, G.E., Schreiner, J.A. and Rogers, L.W., "Canard-Wing Vortex Interaction at Subsonic Through Supersonic Speeds," AIAA Paper 90-2814, August 20-22, 1990.
- ¹⁰ Agrell, N., "Transonic Aerodynamic Computations for a Canard Configuration," AIAA Paper 84-2158, August 1984.
- ¹¹ Bandyopadhyay, G., "Low Speed Aerodynamics of Canard Configurations," *The Aeronautical Journal*, Vol. 93, No. 921, January 1989.
- ¹² Longo, J.M.A. and Das, A., "Numerical Simulation of Vortical Flows Over Close-Coupled Canard-Wing Configuration," AIAA Paper 90-3003-CP, August 1990.
- ¹³ Boyden, R.P., "Subsonic Dynamic Stability Characteristics of Two Close-Coupled Canard-Wing Configurations," NASA TP 1291, October 1978.
- ¹⁴ Tu, E.L., "Effect of Canard Deflection on Close-Coupled Canard-Wing-Body Aerodynamics," AIAA Paper 92-2602, June 1992.
- ¹⁵ Tu, E.L., "Effect of Canard Position on the Longitudinal Aerodynamic Characteristics of a Close-Coupled Canard-Wing-Body Configuration," AIAA Paper 92-4632, August 1992.
- ¹⁶ Obayashi, S., Guruswamy, G.P. and Tu, E.L., "Unsteady Navier-Stokes Computations on a Wing-Body Configuration in Ramp Motions," AIAA Paper 91-2865, August 1991.
- ¹⁷ Guruswamy, G.P., "Navier-Stokes Computations on Swept-Tapered Wings, Including Flexibility," AIAA Paper 90-1152, April 1990.

- ¹⁸ Obayashi, S., Guruswamy, G.P., and Goorjian, P.M., "Streamwise Upwind Algorithm for Computing Unsteady Transonic Flows Past Oscillating Wings," *AIAA Journal*, Vol. 29, No. 10, October 1991, pp. 1668-1677.
- ¹⁹ Obayashi, S. and Guruswamy, G.P., "Unsteady Shock-Vortex Interaction on a Flexible Delta Wing," *Journal of Aircraft*, Vol. 29, No. 5, September-October 1992, pp. 790-798.
- ²⁰ Beam, R. and Warming, R.F., "An Implicit Finite-Difference Algorithm for Hyperbolic Systems in Conservative-Law Form," *Journal of Comp. Physics*, Vol. 22, September 1976, pp. 87-110.
- ²¹ Holst, T.L., Kaynak, U., Gundy, K.L., Thomas, S.D. and Flores, J., "Numerical Solution of Transonic Wing Flows Using an Euler/Navier-Stokes Zonal Approach," *Journal of Aircraft*, Vol. 24, No. 1, January 1987, pp. 17-24.
- ²² Baldwin, B.S. and Lomax, H., "Thin Layer Approximation and Algebraic Model for Separated Turbulent Flows," AIAA Paper 78-257, January 1978.
- ²³ Degani, D. and Schiff, L.B., "Computation of Turbulent Supersonic Flows Around Pointed Bodies Having Crossflow Separation," *Journal of Computational Physics*, 66, 1986, pp. 173-196.
- ²⁴ Luh, R.C., Pierce, L. and Yip, D., "Interactive Surface Grid Generation," AIAA Paper 91-0796, January 1991.
- ²⁵ Sorenson, R.L., "The 3DGRAPE Book: Theory, Users' Manual, Examples," NASA TM 102224, July 1989.
- ²⁶ Gloss, B.B., "Effect of Canard Location and Size on Canard-Wing Interference and Aerodynamic-Center Shift Related to Maneuvering Aircraft at Transonic Speeds," NASA TN D-7505, June 1974.
- ²⁷ Obayashi, S. and Guruswamy, G.P., "Navier-Stokes Computations for Oscillating Control Surfaces," AIAA Paper 92-4431, August 1992.



A diagram showing a wing in a flow field. A coordinate system is established with the x -axis pointing along the flow direction, the y -axis pointing vertically upwards, and the z -axis pointing horizontally to the right. The wing is represented by a curved line with a dashed line indicating its extension. The flow field is bounded by a curved surface on the right.



ORIGINAL PAGE IS
OF POOR QUALITY

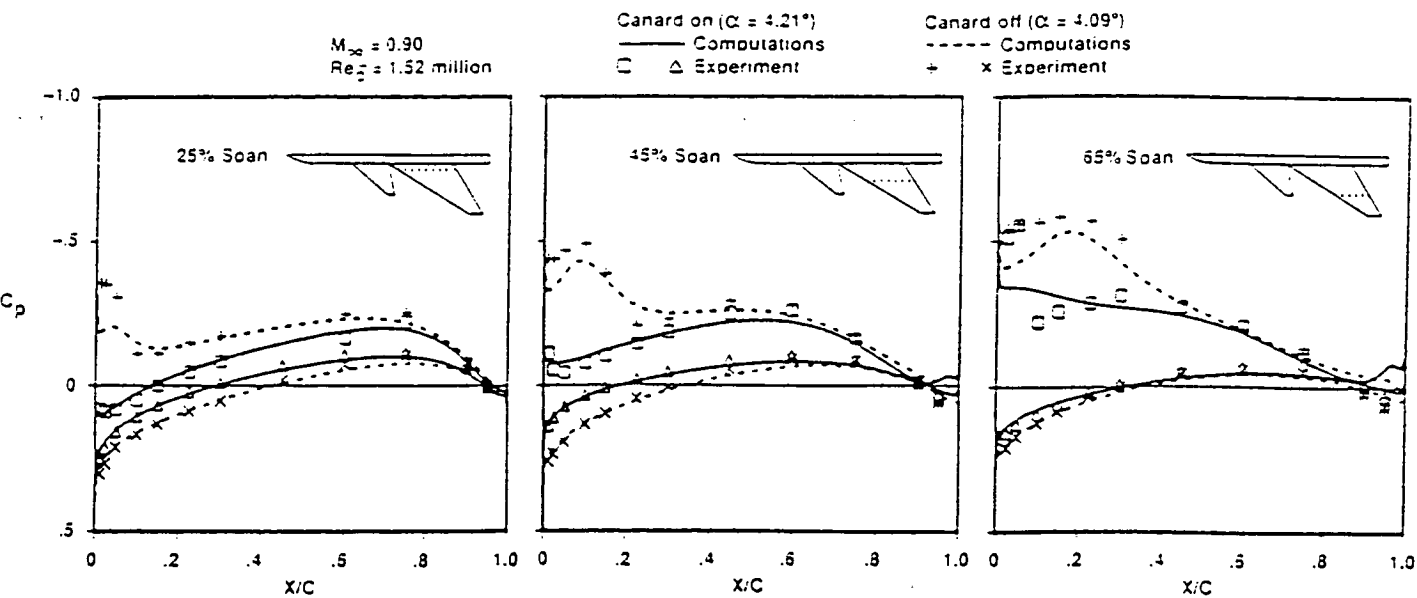


FIG. 3 Effect of canard on wing surface pressures.

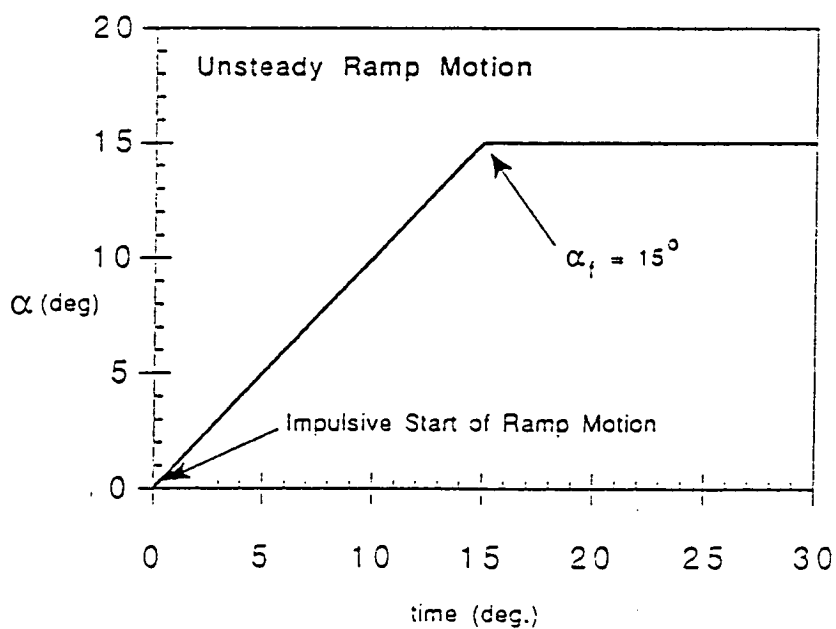


FIG. 4 Pitch-Up Ramp Motion

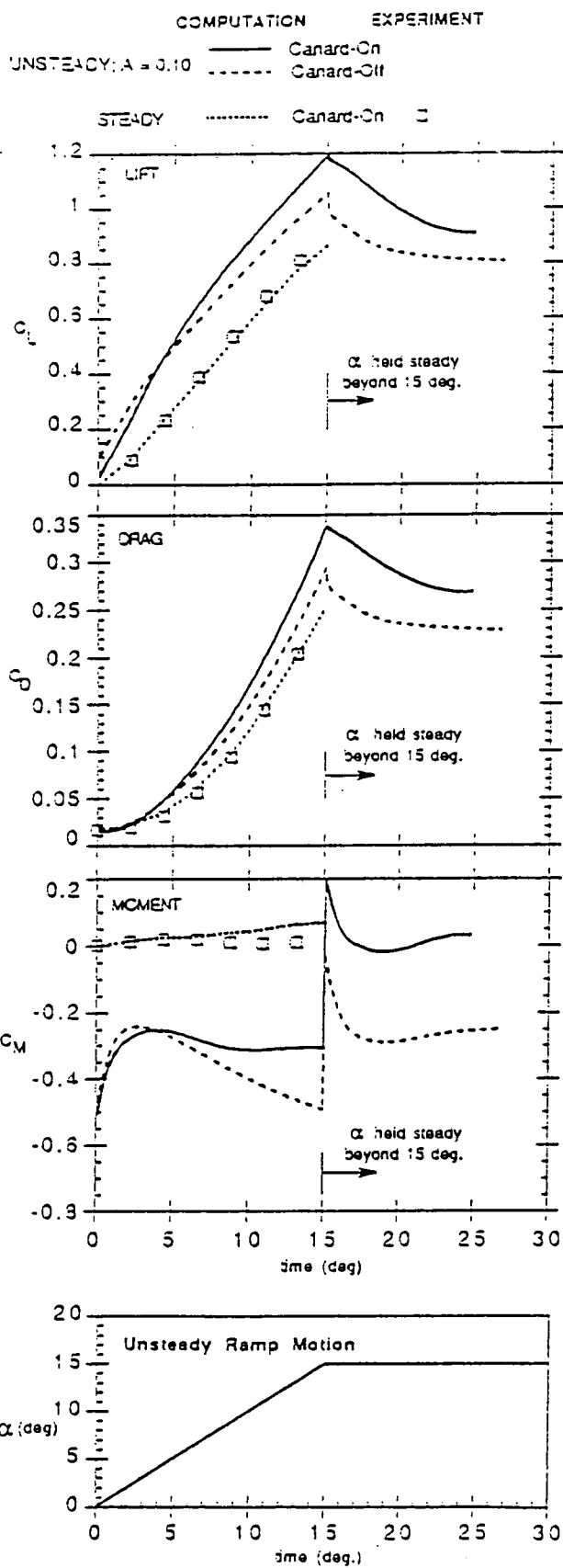


FIG. 5 Effect of canard on unsteady aerodynamic loads during ramp motion.

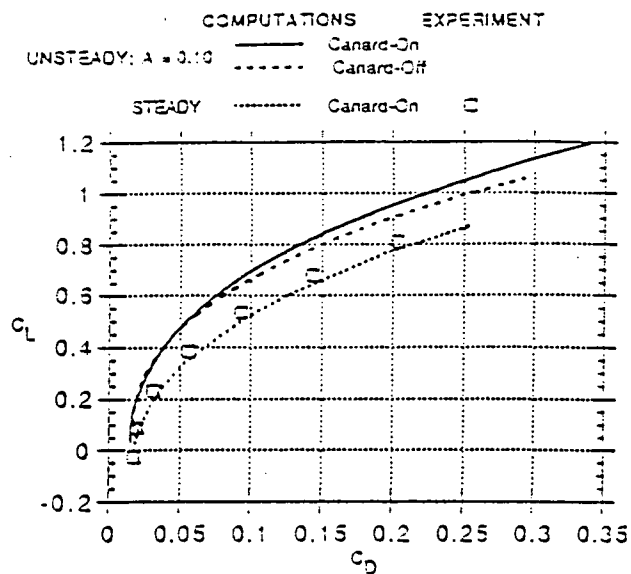


FIG. 6 Drag polar of canard-wing-body configuration undergoing ramp motion.

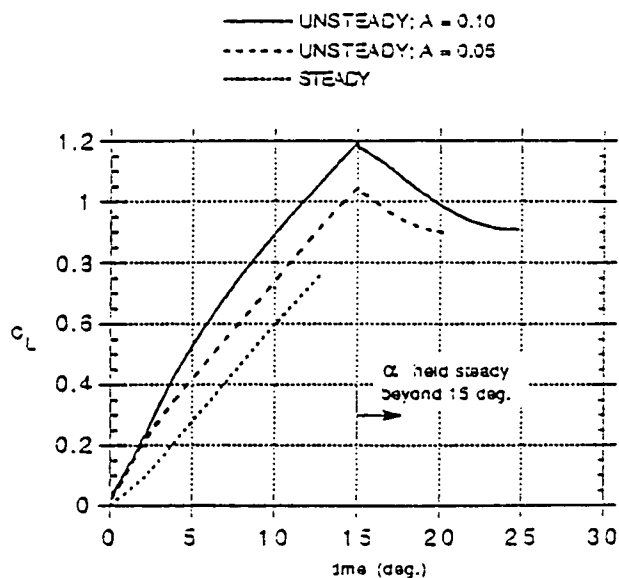


FIG. 7 Effect of pitch rate (A) on dynamic lift.

Unsteady Component Lift Curve
 $M=0.90$, $Re=1.52$ million, $A=0.05$

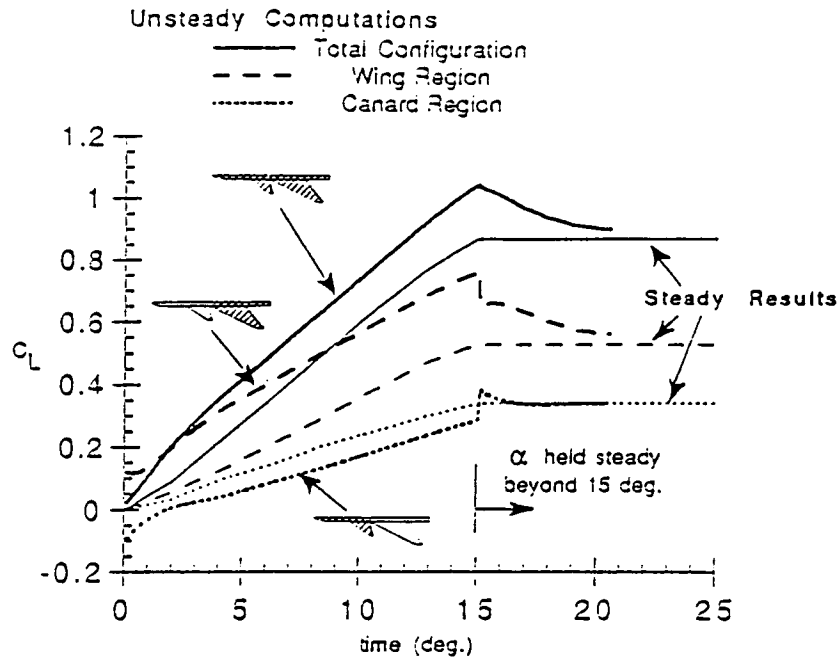


FIG. 8 Component breakdown of dynamic lift due to ramp motion.

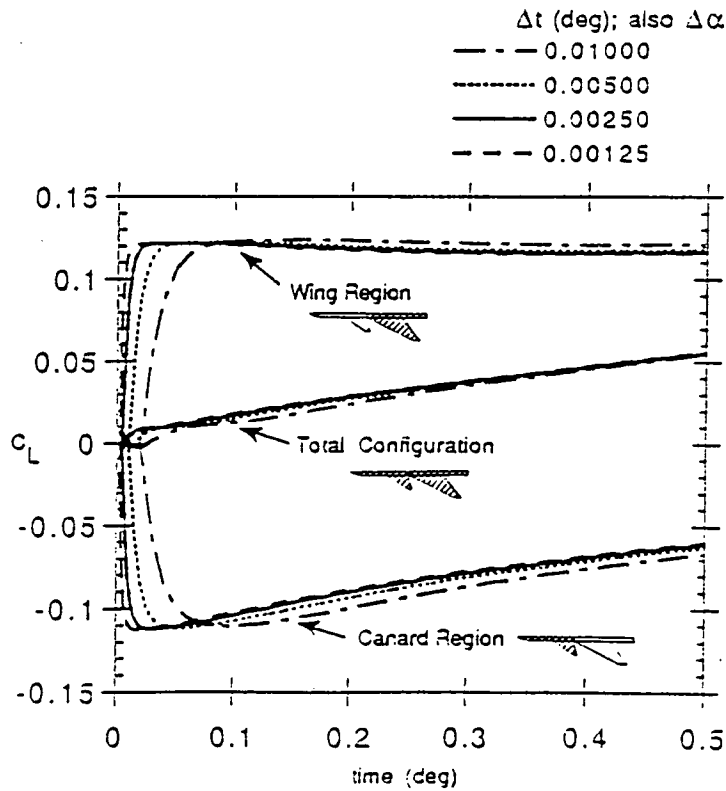


FIG. 9 Effect of time-step size on initial response of ramp motion.

$M = 0.90, \alpha = 8.55^\circ, Re_{\bar{c}} = 1.52 \text{ million}$

UNSTEADY, $A=0.10$

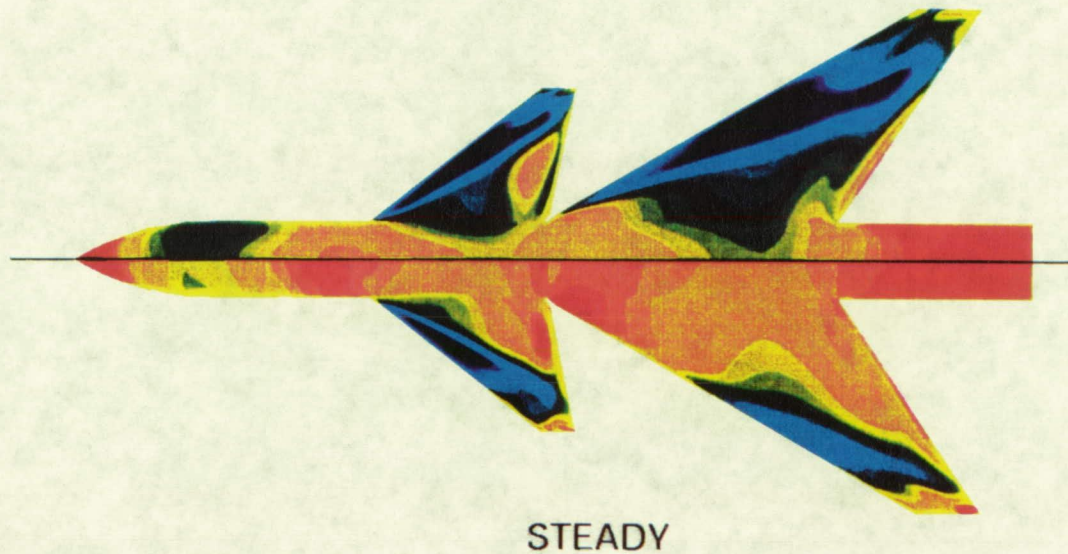


Fig. 10 Effect of ramp motion on unsteady canard-wing-body aerodynamics

APPENDIX F

Extended abstract of a proposed paper for presentation at the AIAA Atmospheric Flight Mechanics Conference, August 9-11, 1993, Monterey, California.

Navier-Stokes Computations on Full-Span Wing-Body Configuration with Oscillating Control Surfaces

Shigeru Obayashi,* Ing-Tsau Chiu† and Guru P. Guruswamy‡

NASA Ames Research Center, Moffett Field, California

Introduction

Aircraft are often subject to aeroelastic oscillation, especially in the transonic regime, because of flow unsteadiness in the presence of the moving shock waves. In this unsteady aerodynamics environment, aircraft rely heavily on active controls for safe and steady flight operation. Active control is also needed for the suppression of flutter without adding structural weight to achieve stable flight conditions.

The influence of control surfaces on both aerodynamics and aeroelastic performance of a wing is more pronounced in the transonic regime. These influences can be constructively used to improve the wing performance through proper actuation of the active control surfaces. Active control technology relies on accurate predictions of unsteady aerodynamics and aeroelastic performance of a wing. Since the experimental evaluation of the effect of a control surface on the wing performance would involve considerable cost and the risk of structural damage in a wind tunnel, it is necessary to initiate the investigation through theoretical analyses.

The present investigation is initiated in conjunction with a recently developed code, ENSAERO, which is capable of computing aeroelastic responses by simultaneously

* Senior Research Scientist, MCAT Institute, San Jose, California. Senior Member AIAA.

† Research Scientist, MCAT Institute, San Jose, California. Member AIAA.

‡ Research Scientist. Associate Fellow AIAA.

integrating the Euler/Navier-Stokes equations and the modal structural equations of motion using aeroelastically adaptive dynamic grids.¹⁻⁴ The code has been applied to transonic flows from small to moderately large angles of attack for fighter wings undergoing unsteady motions. Furthermore, the geometric capability of the code was extended to simulate unsteady flows over a rigid wing with an oscillating trailing-edge flap.

This paper reports unsteady Navier-Stokes simulations of transonic flows over a rigid arrow-wing body configuration of supersonic transport-type aircraft with oscillating control surfaces. The base grid was generated by using the hyperbolic grid generator.⁵ For unsteady computations, the grid moves every time step following the deflection of the control surface. Computations have been made at moderate angles of attack with and without control surface deflections. The flow condition selected is in the transonic regime with a moving shock wave, including leading-edge separation. Computed pressures have been compared with the wind-tunnel experiment.⁶ In the full paper, dynamic stability of the model will be discussed in detail by using computed results. Comparison of response characteristics between symmetric and antisymmetric control surface motions on the right and left wings will also be studied.

Numerical Method

The nondimensionalized Reynolds-averaged thin-layer Navier-Stokes equations are used in this study. The viscosity coefficient is computed as the sum of the laminar and turbulent viscosity coefficients where the laminar viscosity is taken from the freestream laminar viscosity, assumed to be constant for transonic flows. As an option, Sutherland's law can be used to calculate the laminar viscosity. The turbulent viscosity is evaluated by the Baldwin-Lomax algebraic eddy-viscosity model.⁷ Since the flow field to be considered in this paper contains leading-edge separation, it is important to apply a modification to the turbulence model originally developed for crossflow-type separation.⁸

Several numerical schemes have been developed to solve the Navier-Stokes equations. The present code has two different schemes for the inviscid term: the central-difference and streamwise upwind schemes. A second-order central-difference evaluation is applied to the viscous term. An implicit method is used for the time integration because it is more suitable for expensive unsteady viscous calculations. The complete algorithm can be found in Ref. 2. Specific code performance information for the current study is given as follows. All results were computed on either a CRAY-YMP or CRAY-2 computer at NASA Ames Research Center. The performance of the central difference version of ENSAERO is 160 MFLOPS and 15 μ sec per iteration per grid point on a single CRAY-YMP processor.

Sample Results

The first sample result is to show the code capability for computing an oscillating control surface. Figure 1 shows the planform of the clipped delta wing with the trailing-edge control surface. The wing has a leading-edge sweep angle of 50.4 deg and a 6%-thick circular-arc airfoil section. At $M_\infty = 0.9$ and $\alpha = 3$ deg, both a leading-edge vortex and a shock wave are present on the upper surface of the wing. The present C-H grid contains 151 x 44 x 34 points. The gap regions are introduced at the both ends of the control surface (see Fig. 2). This region is used to shear the grid when the control surface oscillates. Although the gap is introduced to simplify the calculations, its effect can be minimized by clustering the grid in this region. The dynamic grid around a deflected control surface was obtained by shearing every grid line normal to the control surface with the local deflection, Δx and Δz . Figure 3 shows the unsteady pressures with the control surface oscillating at a frequency of 8 Hz and an amplitude of 6.65 deg at $M_\infty = 0.9$, $\alpha = 3$ deg and $Re_c = 17 \times 10^6$ based on the root chord. Results are shown as magnitude and phase angle of the upper surface pressure responses at three spanwise sections. The magnitude part of the unsteady pressures shows significant influence of the control surface oscillation. Overall, the computed results show reasonably good agreement with the experiment.

The H-H topology grid is used for a wing-body configuration with a control surface. The ICEM DDN CAD software system by CDC was used to generate the surface grid. Then the volume grid was generated by using HYPGEN code.⁵ To treat the control surface movement, a small gap is introduced at the end of the control surface. Figure 4 shows the geometry of the wind tunnel model.⁶ The configuration is a thin, low aspect ratio, highly swept wing mounted below the centerline of a slender body. The wing is flat with a rounded leading edge. Figure 5 shows the surface grid for the half-span configuration. The body is extended to downstream. This half-span grid consists of 110 points in the streamwise direction, 116 points in the spanwise direction, and 40 points normal to the body surface, in total of 510,400 points. In the following computations, the grid is further divided into the upper and lower grids at the wing and the H-topology cut condition is provided through a zonal interface. For the full-span configuration, the grid is mirrored to the other side and thus the number of the grid points is doubled. It should be noted that the exact wing tip definition was not available so the tip thickness was decreased to zero across three grid points.

Figure 6 shows the steady pressures compared with experiment at three spanwise sections for the half-span configuration. The flow conditions consists of $M_\infty = 0.85$, $\alpha = 8$ deg, $\delta = 0$ deg and $Re_\tau = 9.5 \times 10^6$ based on the mean aerodynamic chord. No data correction was applied to either the computed or measured data. The leading-edge vortex is captured by the computed results well. The grid refinement study for the half-span configuration will be included in the final paper. Figure 7 illustrates the instantaneous antisymmetric position of oscillating control surfaces under computation. Since no unsteady measurement is available, computed mean pressures are validated against the steady data. Comparison of response characteristics between symmetric and antisymmetric control surface motions on the right and left wings will be studied. In the full paper, dynamic stability of the model will be discussed in detail by using computed results.

References

- ¹Guruswamy, G. P., "Navier-Stokes Computations on Swept-Tapered Wings, Including Flexibility," AIAA Paper 90-1152, April 1990.
- ²Obayashi, S., Guruswamy, G. P., and Goorjian, P. M., "Streamwise Upwind Algorithm for Computing Unsteady Transonic Flows Past Oscillating Wings," AIAA Journal, Vol. 29, No. 10, Oct. 1991, pp. 1668-1677. Errata: AIAA Journal, Vol. 30, No. 2, Feb. 1992, pp. 569.
- ³Obayashi, S. and Guruswamy, G. P., "Unsteady Shock-Vortex Interaction on a Flexible Delta Wing," Journal of Aircraft, Vol. 29, No. 5, Sept.-Oct. 1992, pp. 790-798.
- ⁴Obayashi, S. and Guruswamy, G. P., "Navier-Stokes Computations for Oscillating Control Surfaces," AIAA Paper 92-4431, August 1992.
- ⁵Chan, W. M. and Steger, J. L., "Enhancement of a Three Dimensional Hyperbolic Grid Generation Scheme," Applied Mathematics and Computation, Vol. 51, Oct. 1992, pp. 181-205.
- ⁶Manro, M. E., Manning, K. J. R., Hallstaff, T. H. and Rogers, J. T., "Transonic Pressure Measurements and Comparison of Theory to Experiment for an Arrow-Wing Configuration," NASA CR-2610, August 1976.
- ⁷Baldwin, B. S. and Lomax, H., "Thin-Layer Approximation and Algebraic Model for Separated Turbulent Flows," AIAA Paper 78-257, Jan. 1978.
- ⁸Degani, D. and Schiff, L. B., "Computations of Turbulent Supersonic Flows Around Pointed Bodies Having Crossflow Separation," Journal of Computational Physics, Vol. 66, No. 1, Sept. 1986, pp. 173-196.

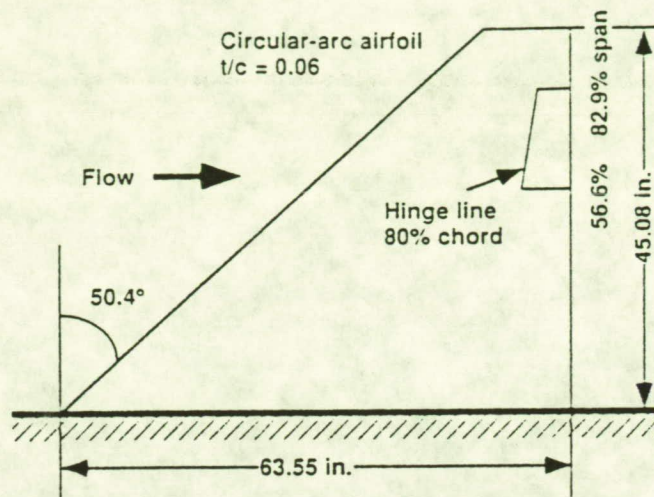


Fig. 1 Planform of a clipped delta wing.

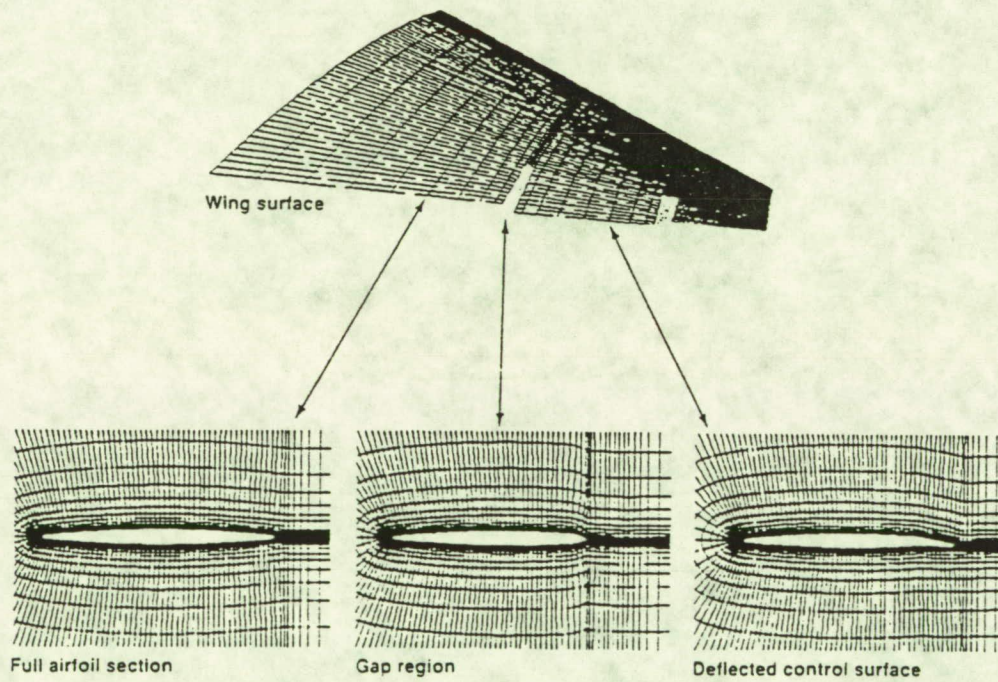


Fig. 2 Grid for a wing with a control surface.

$M_\infty = 0.9$, $Re = 17 \times 10^6$
 $\alpha = 3^\circ$, $\delta = 6.65^\circ$
 $k = 0.588$
 Grid: $151 \times 41 \times 34$

— Computation
 □ Experiment, Hess et al.

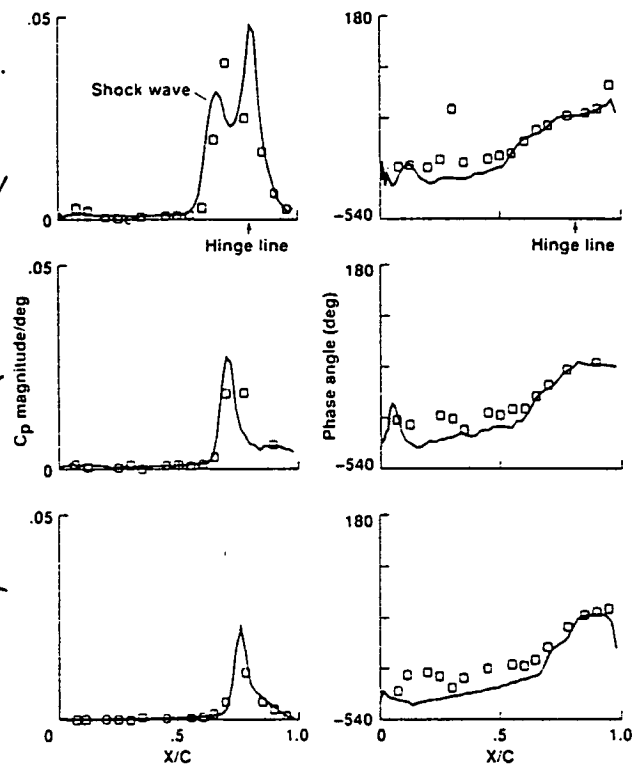
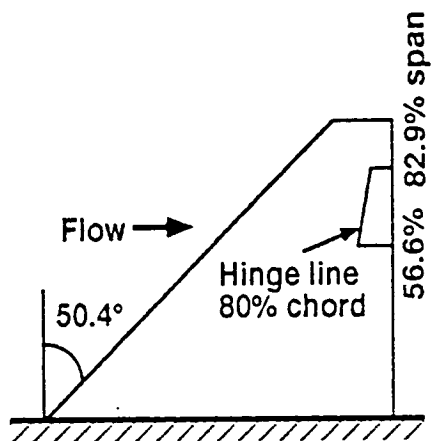


Fig. 3 Comparison of computed unsteady pressures with experiment on the upper surface of the clipped delta wing.

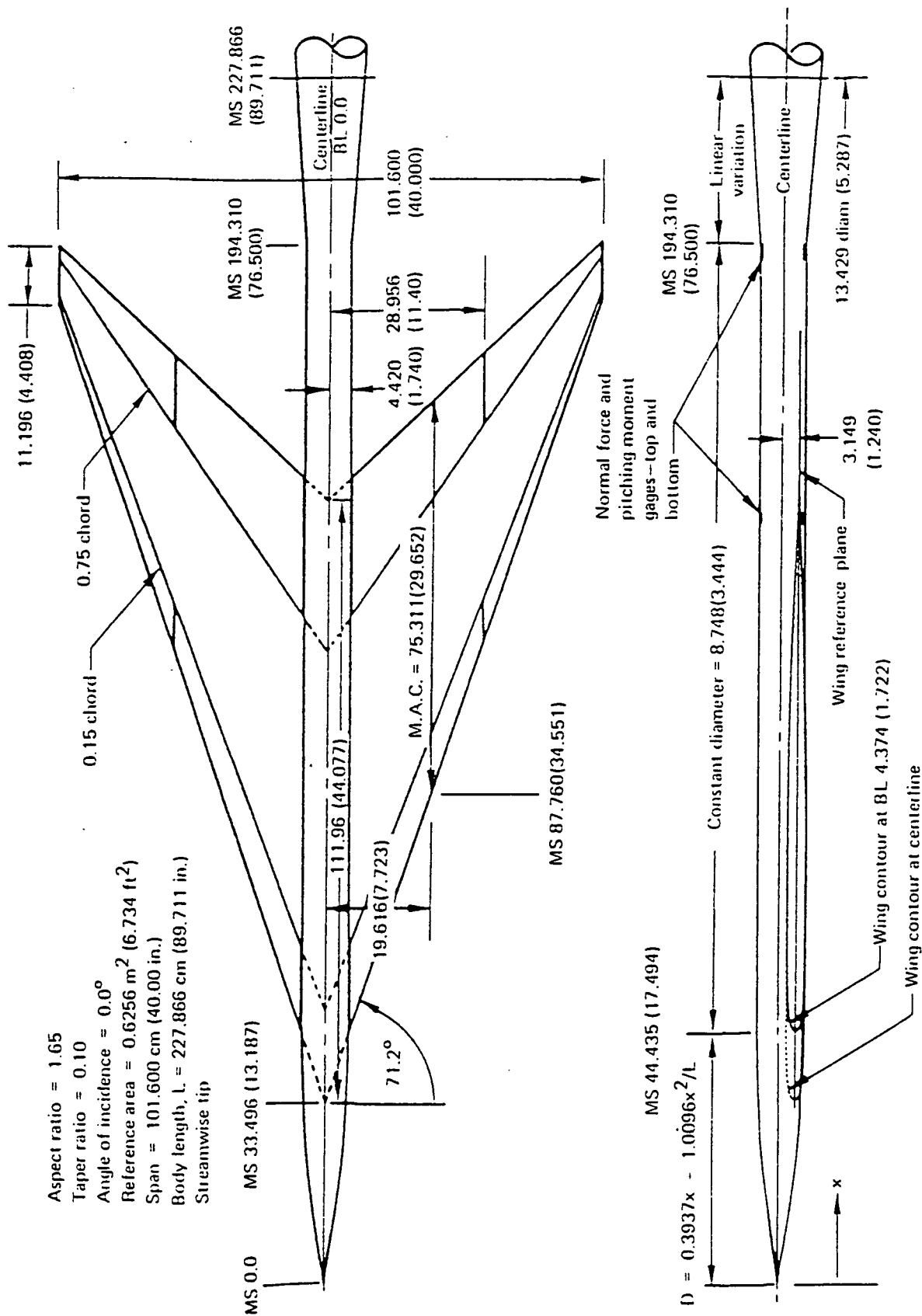


Fig. 4 Wind-tunnel model geometry of an arrow-wing body configuration.

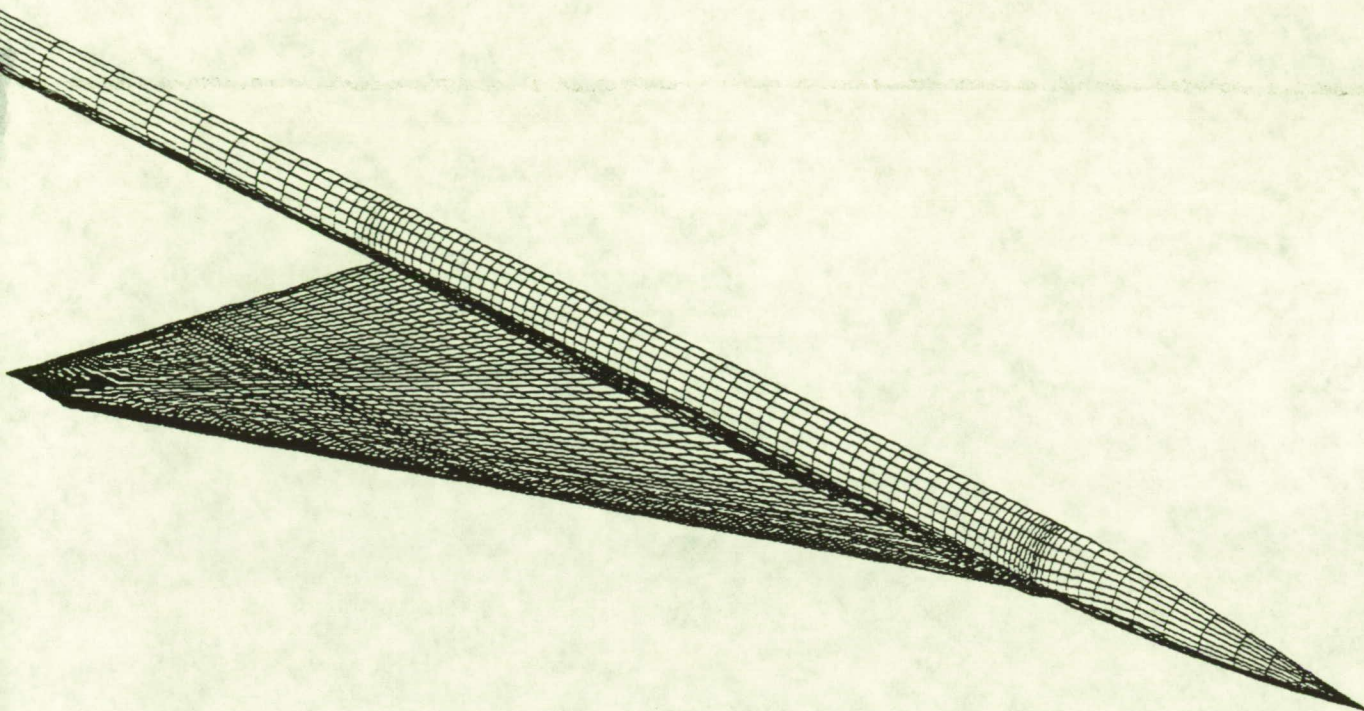


Fig. 5 Surface grid for the half-span configuration.

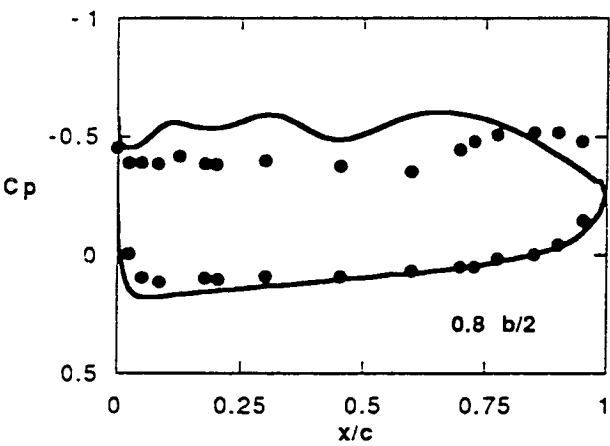
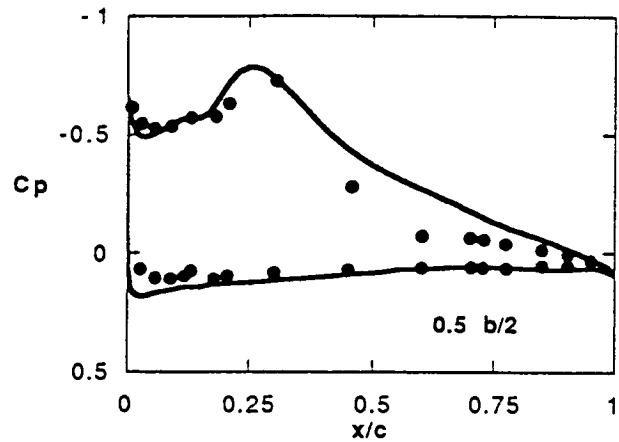
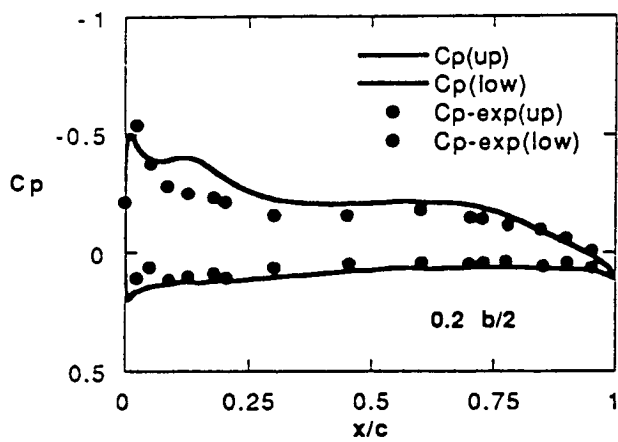


Fig. 6 Comparison of computed steady pressures with experiment on the wing surface of the half-span configuration.

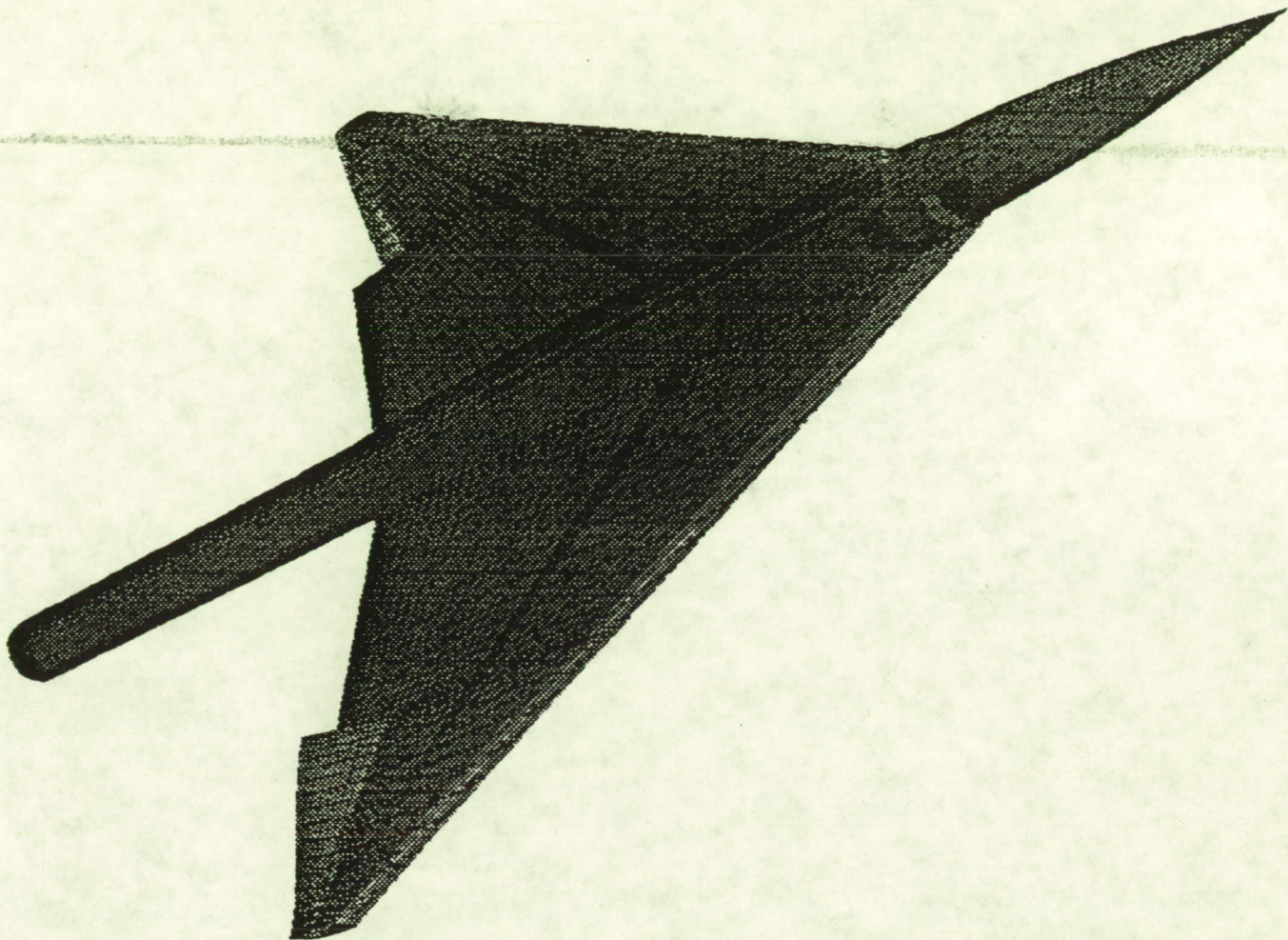


Fig. 7 Instantaneous view of antisymmetric oscillations of control surfaces.